

3-10-2010

Particle Size Control for PIV Seeding Using Dry Ice

Brian T. Love

Follow this and additional works at: <https://scholar.afit.edu/etd>

 Part of the [Aerodynamics and Fluid Mechanics Commons](#)

Recommended Citation

Love, Brian T., "Particle Size Control for PIV Seeding Using Dry Ice" (2010). *Theses and Dissertations*. 2046.
<https://scholar.afit.edu/etd/2046>

This Thesis is brought to you for free and open access by the Student Graduate Works at AFIT Scholar. It has been accepted for inclusion in Theses and Dissertations by an authorized administrator of AFIT Scholar. For more information, please contact richard.mansfield@afit.edu.



PARTICLE SIZE CONTROL FOR PIV SEEDING USING DRY ICE

THESIS

Brian T. Love, Captain, USAF

AFIT/GAE/ENY/10-M15

DEPARTMENT OF THE AIR FORCE
AIR UNIVERSITY

AIR FORCE INSTITUTE OF TECHNOLOGY

Wright-Patterson Air Force Base, Ohio

APPROVED FOR PUBLIC RELEASE; DISTRIBUTION UNLIMITED.

The views expressed in this thesis are those of the author and do not reflect the official policy or position of the United States Air Force, Department of Defense, or the United States Government. This material is declared a work of the U.S. Government and is not subject to copyright protection in the United States.

AFIT/GAE/ENY/10-M15

PARTICLE SIZE CONTROL FOR PIV SEEDING USING DRY ICE

THESIS

Presented to the Faculty

Department of Aeronautics and Astronautics

Graduate School of Engineering and Management

Air Force Institute of Technology

Air University

Air Education and Training Command

In Partial Fulfillment of the Requirements for the
Degree of Master of Science in Aeronautical Engineering

Brian T. Love, BS

Captain, USAF

March 2010

APPROVED FOR PUBLIC RELEASE; DISTRIBUTION UNLIMITED.

PARTICLE SIZE CONTROL FOR PIV SEEDING USING DRY ICE

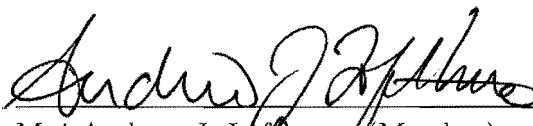
Brian T. Love, BS
Captain, USAF

Approved:




Dr. Mark F. Reeder (Chairman)

19 Mar 10
Date



Maj Andrew J. Lofthouse (Member)

19 Mar 10
Date



LtCol Richard E. Huffman (Member)

19 MAR 10
Date

Abstract

Particle image velocimetry (PIV) has been carried out using solid carbon dioxide (CO_2) particles as the seed material to continue the development of clean seeding for use in large-scale, closed-circuit tunnels. Testing occurred in two wind tunnels at subsonic and supersonic speeds using dry ice particles generated by allowing liquefied CO_2 to expand from a small diameter injector tube through a larger diameter shroud tube. The particles were injected into the plenum and discrete solid particles, suitable for PIV measurements, were present in the test section. Data on particle size were first collected using a Malvern particle size analyzer for three sizes of injector tubes, two sizes of shroud tubes, and two different types of shroud tubes: a simple tube and a static mixing tube. The injectors using the static mixing shroud tube and the simple shroud tube were each used in the adjustable throat supersonic blowdown wind tunnel at the Air Force Institute of Technology with a 6 inch by 6.5 inch cross section. Particle size results for these two configurations suggested that the static mixing shroud tube decreased the Sauter mean particle diameter by a factor of three. In the tunnel, Mach 1.92 flow over a 10° ramp was produced and PIV images captured particles above the ramp both upstream and downstream of the oblique shock while schlieren imaging provided insight into the flow conditions. Both the velocities far upstream and far downstream of the shock closely matched expectations, based on the wind tunnel instrumentation. Particle lag for the flow across the shock was quantified for the two cases, and despite the substantial, quantified differences in particle size measured at the shroud tube exit, the results for both shroud tubes were generally consistent with a theoretical response of a $2\ \mu\text{m}$ particle. Finally, for the first time particles were injected into the stilling chamber of the Air Force Research Laboratory's closed-circuit Trisonic Gas-dynamics Facility, which has a 24 inch by 24 inch cross-section at three subsonic speeds and four stagnation pressures. PIV was successfully carried out in each case. Measured streamwise velocities matched expected velocities within a few percent based on tunnel instrumentation, and

freestream turbulence was found to be less than 2% in most cases. These results suggest that PIV using CO₂ particles may be robustly implemented in this closed-circuit wind tunnel without risk of contaminating the tunnel.

Acknowledgements

First and foremost, I would like to thank my advisor Dr. Mark Reeder for his unwavering support and endless patience. Thank you for giving me the freedom to explore while providing clear guidance throughout this endeavor. I'd also like to thank Mr. John Hixenbaugh, Mr. Chris Zickefoose, and Mr. Jay Anderson for their professionalism and for providing me with the facilities and equipment necessary to accomplish this test. John, thank you for never accepting "no" for an answer. Many road blocks were easily surpassed with your help. Chris, thank you for your help with the rapid prototyping machines, tools, media equipment and for a good laugh at every turn. Jay, thank you for keeping me out of too much trouble with the hardware in your labs!

Mr. Brian Crabtree at the AFIT model shop was instrumental in the design and fabrication of the new wind tunnel test section. Thank you for being a pro at what you do and for always being willing to help me with every job, no matter how small. The work you did was exceptional!

I'd like to thank my sponsors at AFRL. Thank you to Mr. Tom Presdorf for your support throughout this project, and thank you to Dr. Ryan Schmit, Dr. Aaron Altman, Lt. Mike Belliss, Mr. Shawn Raisch, and Mr. Paul Olekas for all your help in bringing this system into the TGF. How many PhDs does it take to complete a Master's thesis? I look forward to working with all of you!

Finally, I'd like to thank the Faculty and Staff at AFIT for making this such an outstanding academic experience for me.

Brian T. Love

Table of Contents

	Page
Abstract	iv
Acknowledgements	vi
List of Figures	ix
List of Tables	xii
I. Introduction	1
1.1 Motivation	2
1.2 Research Focus	3
II. Background	5
2.1 PIV Overview	5
2.1.1 Light Source	5
2.1.2 Flow Seeding	6
2.1.3 Image Acquisition and Correlation	9
2.2 Discrete CO ₂ Particle Formation and Characterization	10
2.3 Particle Size Analysis	12
2.4 High Speed Wind Tunnel Testing	13
2.4.1 Tunnel Design	13
2.4.2 Mass Flow	14
2.4.3 Isentropic Relations	14
2.5 Schlieren Imaging	15
III. Methodology	17
3.1 Particle Generation	17
3.2 Particle Size Analysis	19
3.3 AFIT Wind Tunnel Tests	21
3.3.1 Wind Tunnel	21
3.3.2 Schlieren	22
3.3.3 PIV System	23
3.4 AFRL Wind Tunnel Tests	28
3.4.1 Trisomic Gas-dynamics Facility	28
3.4.2 PIV System	29

	Page
IV. Results and Discussion	34
4.1 Particle Size Analysis	34
4.1.1 Particle Dispersion	35
4.1.2 Effect due to Feed Tube Size	35
4.1.3 Effect due to Shroud Size	37
4.1.4 Effect due to Shroud Type	37
4.1.5 Effect due to Thermal Bath Temperature	39
4.1.6 Sources of Error in Particle Size Analysis	40
4.2 AFIT Wind Tunnel Results	41
4.2.1 Simple Shroud Tubes	41
4.2.2 Static Mixing Shroud Tubes	49
4.2.3 Sources of Error in AFIT Wind Tunnel Testing	55
4.3 AFRL Wind Tunnel Results	56
4.3.1 Cross Plane	56
4.3.2 Streamwise Plane	59
4.3.3 Sources of Error in AFRL Wind Tunnel Testing	75
V. Conclusions	80
5.1 Overview of Research Effort	80
5.2 Conclusions	81
5.3 Impact of Research	83
5.4 Future Work	83
Appendix A. Theoretical Response Curves Using Melling's Approach	85
Bibliography	88

List of Figures

Figure		Page
2.1	Principle components of PIV.	6
2.2	Rayleigh and Mie scattering characteristics	7
2.3	Diagram of the cross-correlation process.	10
2.4	Diagram of a simple schlieren system with a point light source	16
2.5	Diagram of a Herschellian schlieren system	16
3.1	Feed and shroud tubes used during experimentation.	18
3.2	Kenics [®] static mixer	18
3.3	Malvern Spraytec particle size analyzer setup.	20
3.4	Refrigerated bath filled with deionized, distilled water for heat exchange.	21
3.5	AFIT 6 inch by 6.5 inch supersonic blowdown wind tunnel.	22
3.6	Approximate location of the field of view for the schlieren and PIV camera	23
3.7	Laser and camera setup for PIV measurements in the AFIT 6 inch by 6.5 inch wind tunnel.	25
3.8	Calibration grid imaged to scale the field of view.	26
3.9	Injection from above the test section used for system checkout.	27
3.10	Side view of the TGF	30
3.11	TGF subsonic test section performance chart	31
3.12	Exterior view of CO ₂ injectors in the stagnation chamber wall of the TGF with an interior view inset looking up from the access door.	32
3.13	View of test section injector, looking upstream towards stagnation chamber.	33
4.1	Percent of total number of particles measured at each particle diameter.	35
4.2	Percent of total volume particles of a given size make up.	36
4.3	Characteristic profile of particles exiting a simple shroud tube.	36
4.4	Characteristic profile of particles exiting a mixing shroud tube.	37
4.5	D ₃₂ for varying feed tube ID and a constant 0.33 inch ID shroud tube.	38
4.6	D ₃₂ for varying shroud tube size and constant 0.068 inch feed tube ID.	38
4.7	D ₃₂ for a simple versus mixing shroud tube type.	39
4.8	D ₃₂ for the mixing shroud, 0.068 inch ID feed tube and varying shroud bath temperature.	40
4.9	Typical transient conditions of AFIT blowdown wind tunnel operation.	42
4.10	Horizontal velocity component using simple tubes and a 32 x 32 pixel IR.	43
4.11	Horizontal velocity component using simple tubes and a 64 x 64 pixel IR.	44

	Page
4.12	Vertical velocity component using simple tubes and a 32 x 32 pixel IR. . . 45
4.13	Vertical velocity component using simple tubes and a 64 x 64 pixel IR. . . 45
4.14	Schlieren image of flow upstream of PIV FOV showing a weak shock caused by tunnel roughness and a strong shock caused by the 10° ramp. . 46
4.15	Velocity normal to the shock using simple tubes and a 32 x 32 pixel IR. . 47
4.16	Velocity normal to the shock using simple tubes and a 64 x 64 pixel IR. . 48
4.17	Particle response using two IR sizes compared to theoretical response for varying particle sizes. 48
4.18	Horizontal velocity component using mixing tubes and a 32 x 32 pixel IR. 50
4.19	Horizontal velocity component using mixing tubes and a 64 x 64 pixel IR. 51
4.20	Vertical velocity component using mixing tubes and a 32 x 32 pixel IR. . . 51
4.21	Vertical velocity component using mixing tubes and a 64 x 64 pixel IR. . . 52
4.22	Velocity normal to the shock using mixing tubes and a 32 x 32 pixel IR. . 52
4.23	Velocity normal to the shock using mixing tubes and a 64 x 64 pixel IR. . 53
4.24	Particle response using two IR sizes compared to theoretical response for varying particle sizes 53
4.25	128 by 128 pixel regions for simple injectors at f5.6 (left) and mixing injectors at f4.0 (right). 54
4.26	Nine sequential frames using a red reference line to indicate shock displacement over time. 54
4.27	Cross-plane PIV setup at the TGF with approximate fields of view for each camera. 57
4.28	Image of seeding from curved 0.4 inch ID shroud at M=0.8, P=250 psf. . 58
4.29	Image of seeding from simple 0.33 inch ID shroud at M=0.8, P=250 psf showing lack of particles. 59
4.30	Image of seeding from simple 0.17 inch ID shroud at M=0.8, P=250 psf showing typical jet in a crossflow profile. 60
4.31	Approximate PIV image location within the test section. 60
4.32	Setup for PIV data collection in the TGF. 61
4.33	Sample PIV image collected in the TGF 62
4.34	Sample PIV vector map overlaid on the approximate field of view for the PIV arrangement at the TGF. 62
4.35	Streamwise velocity maps at $P_0 = 500$ psf and varying speeds. 64
4.36	Vertical velocity maps at $P_0 = 500$ psf and varying speeds. 65
4.37	Streamwise velocity profile at $M = 0.89$, $P_0 = 255$ psf, and $T_0 = 294$ K. . 66
4.38	Streamwise velocity profile at $M = 0.79$, $P_0 = 501$ psf, and $T_0 = 296$ K. . 66

4.39	Streamwise turbulence profile at $M = 0.89$, $P_0 = 255$ psf, and $T_0 = 294$ K normalized by the calculated freestream velocity, 286 m/s.	67
4.40	Vertical velocity turbulence profile at $M = 0.89$, $P_0 = 255$ psf, and $T_0 = 294$ K normalized by the calculated freestream velocity, 286 m/s.	67
4.41	Streamwise velocity turbulence profile at $M = 0.79$, $P_0 = 501$ psf, and $T_0 = 296$ K normalized by the calculated freestream velocity, 257 m/s. . .	68
4.42	Vertical velocity turbulence profile at $M = 0.79$, $P_0 = 501$ psf, and $T_0 = 296$ K normalized by the calculated freestream velocity, 257 m/s.	68
4.43	Streamwise velocity profile at $M = 0.5$, $P_0 = 500$ psf, and $T_0 = 294$ K. . .	70
4.44	Streamwise velocity profile at $M = 0.5$, $P_0 = 1000$ psf, and $T_0 = 294$ K. .	70
4.45	Streamwise velocity profile at $M = 0.5$, $P_0 = 1500$ psf, and $T_0 = 294$ K. .	71
4.46	Streamwise turbulence profile at $M = 0.5$, $P_0 = 500$ psf, and $T_0 = 294$ K normalized by the calculated freestream velocity, 170 m/s.	71
4.47	Vertical velocity turbulence profile at $M = 0.5$, $P_0 = 500$ psf, and $T_0 = 294$ K normalized by the calculated freestream velocity, 170 m/s.	72
4.48	Streamwise turbulence profile at $M = 0.5$, $P_0 = 1000$ psf, and $T_0 = 294$ K normalized by the calculated freestream velocity, 170 m/s.	72
4.49	Vertical velocity turbulence profile at $M = 0.5$, $P_0 = 1000$ psf, and $T_0 = 294$ K normalized by the calculated freestream velocity, 170 m/s.	73
4.50	Streamwise turbulence profile at $M = 0.5$, $P_0 = 1500$ psf, and $T_0 = 294$ K normalized by the calculated freestream velocity, 170 m/s.	73
4.51	Vertical velocity turbulence profile at $M = 0.5$, $P_0 = 1500$ psf, and $T_0 = 294$ K normalized by the calculated freestream velocity, 170 m/s.	74
4.52	Streamwise velocity profile at $M = 0.30$, $P_0 = 517$ psf, and $T_0 = 298$ K. .	75
4.53	Streamwise velocity profile at $M = 0.30$, $P_0 = 1007$ psf, and $T_0 = 298$ K. .	76
4.54	Streamwise velocity profile at $M = 0.30$, $P_0 = 1506$ psf, and $T_0 = 300$ K. .	76
4.55	Streamwise turbulence profile at $M = 0.30$, $P_0 = 517$ psf, and $T_0 = 298$ K normalized by the calculated freestream velocity, 103 m/s.	76
4.56	Vertical velocity turbulence profile at $M = 0.30$, $P_0 = 517$ psf, and $T_0 = 298$ K normalized by the calculated freestream velocity, 103 m/s.	77
4.57	Streamwise turbulence profile at $M = 0.30$, $P_0 = 1007$ psf, and $T_0 = 298$ K normalized by the calculated freestream velocity, 104 m/s.	77
4.58	Vertical velocity turbulence profile at $M = 0.30$, $P_0 = 1007$ psf, and $T_0 = 298$ K normalized by the calculated freestream velocity, 104 m/s. . .	78
4.59	Streamwise turbulence profile at $M = 0.30$, $P_0 = 1506$ psf, and $T_0 = 300$ K normalized by the calculated freestream velocity, 104 m/s.	78
4.60	Vertical velocity turbulence profile at $M = 0.30$, $P_0 = 1506$ psf, and $T_0 = 300$ K normalized by the calculated freestream velocity, 104 m/s. . .	79

List of Tables

Table		Page
2.1	Common seeding materials for gas flows	7
3.1	Feed and shroud tube sizes	19
3.2	Test conditions for TGF.	29
3.3	Range validation for TGF data.	31
4.1	Injector configurations for TGF testing.	57
4.2	Turbulence estimates based on all valid vectors at each test condition.	69

PARTICLE SIZE CONTROL FOR PIV SEEDING USING DRY ICE

I. Introduction

AVIATION has made quick and efficient world travel possible, has given a new dimension to the art of war, and has become the stepping stone into the space age. Improving this industry has motivated the ever increasing study of fluid mechanics, allowing the advancement of aircraft and rockets alike. It stands to reason that, with such a vast impact on these industries, improving the methods and efficiency with which this understanding is achieved also has its merits. In modern history, theory, observation and experimentation have been the predominant means to make advancements in the field. Though there is limited evidence of his experiments in flight actually being carried out, the observations, drawings and notes of Leonardo da Vinci showed an analytical process to develop a way for humans to mimic the flight of birds [1]. Since his time, countless individuals have tackled issues dealing with the mechanics of fluids, including Newton, Bernoulli, Euler, Navier, Stokes, Reynolds, and Prandtl, just to name a few.

The fundamental theories, concepts and equations developed by these and many others are the basis from which human flight was made possible, as proven by the Wright brothers in the early 1900s. The Wrights, however, experienced setbacks with lower than expected performance of their original gliders that could have halted their progress if they were without ingenuity and perseverance [2]. In late 1901 they designed and built a wind tunnel to test different wing designs, ultimately providing the data necessary to move forward with their aircraft. As it was then, today it is still necessary to test items of interest in facilities such as wind tunnels because, even with the advent and

rise of computer modeling, there are still many problems in fluid motion that require experimental data.

1.1 Motivation

Many experimental methods exist today that can be used to gain insight into an area of interest, each with its advantages and disadvantages. One of these is particle image velocimetry (PIV) which is based on the simple relation that velocity is the distance traveled per unit of time. If particles can be placed in a fluid under the right conditions, the particles will move at the same speed as the fluid. If two sequential images of a particle are captured with a known time increment between the two, the distance traveled by the particle can be deduced by comparing the first image to the second. Coupled with the knowledge of the time difference between the two images, the speed can be determined. Raffel, et. al. make the analogy between this and children throwing pieces of wood in a stream to observe them float downstream [3]. A practical application of this simple concept has been applied by sailors for centuries when a floating object such as a log or buoy tied to a rope would be tossed overboard. Equally spaced knots would be tied in the rope and as the rope unraveled overboard, the number of knots would be counted and timed, likely with a sand glass. When the sand ran out the number of knots would be tallied and the ship's speed was determined. Hence the nautical term "knot" was coined to describe speed [4].

As simple as this concept is, the application to aerodynamics and other fields of study can be quite complex, as discussed in chapter 2, due in part to the presence of multiple particles within the field of view. Once these complexities are understood, however, a great deal of information can be obtained about the fluid flow of interest. With planar velocity data, one can determine boundary layer effects, turbulence characteristics, eddy formations, momentum thickness, and so on. The applications of PIV in aerodynamics and water flows continue to grow [3]. Consequently, there is interest in refining this technique to improve its accuracy as well as its practicality.

One of the problems presented by PIV is that introducing particles in tunnels can be inconvenient and costly. One facility, the Air Force Research Laboratory's (AFRL)

Trisonic Gas-dynamics Facility (TGF), requires additional maintenance to clear the tunnel of the particles used for PIV measurements. The TGF is a closed-circuit supersonic wind tunnel, meaning that particulates introduced into the flow for PIV persist either in the flow or accumulate on surfaces within the tunnel. In one recent case, the use of an oil-based smoke to seed the air flow caused a residue to build up on the tunnel walls and test section glass, necessitating substantial cleaning after the test. Also, residue from oil-based or solid seed material, such as titanium dioxide, can spoil measurements executed using pressure-sensitive paint. Additional maintenance means additional cost and increased downtime of the tunnel. With this type of impact, the practicality of using PIV in the TGF and other similar facilities is reduced until there exists a method to cleanly seed the flow. Many examples of oil- and water-based aerosolized seeding are available, including recent studies at the Arnold Engineering Development Center's 16T wind tunnel, showing that if these seed materials can be replaced with clean seeding methods, many facilities could benefit [5, 6]. To this end, the past several years have seen the introduction and advancement of using solid carbon dioxide (CO_2), or dry ice, to seed the flow. CO_2 can exist as a solid and then sublimate, leaving no trace or residue other than the naturally occurring inert gas that mixes into the surrounding air. Thus, if particles of dry ice can be inserted into the air flow, they can persist long enough to pass through the test section and then sublimate, negating any need for additional maintenance on the wind tunnel due to PIV testing alone.

1.2 Research Focus

The selection of particle type is critical for successful PIV measurements, not only because of the impact to the facilities using PIV, but for the measurements themselves. It is necessary to select particles with the proper characteristics that make for accurate measurements, including size, density, quantity, and light scattering characteristics. The research presented here focuses on correctly sizing CO_2 particles and determining methods to increase the number of particles to provide sufficient data for accurate velocity vector mapping. Particles must be small enough to accurately track the fluid in question while still being large enough to scatter ample light to be captured by a camera

sensor. The particle density should be as close to the fluid density as possible so that the effect due to gravity and the response time due to fluid accelerations are minimized. Lastly, there needs to be sufficient particle coverage over the field of view to maximize the resolution of the velocity vector field.

This research also attempts to scale the seeding method by injecting particles into the TGF and, for the first time, collecting PIV data using CO₂ seeding. Previous work by Greene, DeLapp, McNiel, and Peltier, under the direction of Dr. Mark Reeder, honed the methods for CO₂ particle generation and its viability for PIV application [7, 8, 9]; this research refines their methods with the following goals:

- Increase particle count to improve spatial resolution of measurements in the AFIT supersonic wind tunnel
- Assess methods for controlling particle size
- Characterize particle response to an oblique shock wave using different injectors
- Demonstrate PIV in the TGF

Previously, the injectors used for seeding were varied to assess the size distribution on the resulting particles. Factors such as the injection orifice size, injector shroud size, and injection point were all found to be important. Several injection methods and injection points were tested to find a suitable solution to the seeding problem. However, attempts to scale the injection method for use in a larger wind tunnel had limited success in achieving sufficient particle coverage [10, 11]. Thus the research presented in the following chapters discusses the attempt to improve upon this along with the goals listed above.

II. Background

IN this chapter, background information is provided on the systems used for this research. First, the basics of PIV are covered, discussing the components that are necessary to accomplish PIV. Emphasis is placed on flow seeding because of its importance in this research. Recent research in the field of clean-seeding is discussed. Next, the wind tunnel and the mathematical relations that will be relevant for calculations in this research are discussed. Finally, the basic schlieren setup is discussed as it pertains to this research.

2.1 PIV Overview

Advancements in technology over the past decades have allowed PIV to become a viable and common measurement technique. Correlating particle motion between different images is a hurdle that has been relatively easy to overcome with the introduction of digital charge coupled device (CCD) camera technology and computing power enhancements. Figure 2.1 displays the basic components of PIV, namely the seeding material, light source, imaging optics and imaging sensor. Each of these components is briefly described below but the interested reader is referred to Raffel, et. al., for an in depth review of PIV [3].

2.1.1 Light Source. Light is necessary to illuminate the particles in the flow sufficiently to be detected by the camera sensor. For planar PIV as shown in Figure 2.1, lasers are typically used because they emit monochromatic light with high energy density that is easily manipulated through a careful selection of optics to produce a light sheet that illuminates the full field of view of the camera [3]. A common type of laser, also used for this research, is the neodymium-doped yttrium-aluminum-garnet (ND:YAG) laser which uses two resonators that produce light at a wavelength of $\lambda = 1064$ nm that is then frequency doubled to get a wavelength of $\lambda = 532$ nm in the visible green spectrum. Solid state lasers such as this can produce high repetition, low duration pulses of energy making them ideal for PIV applications.

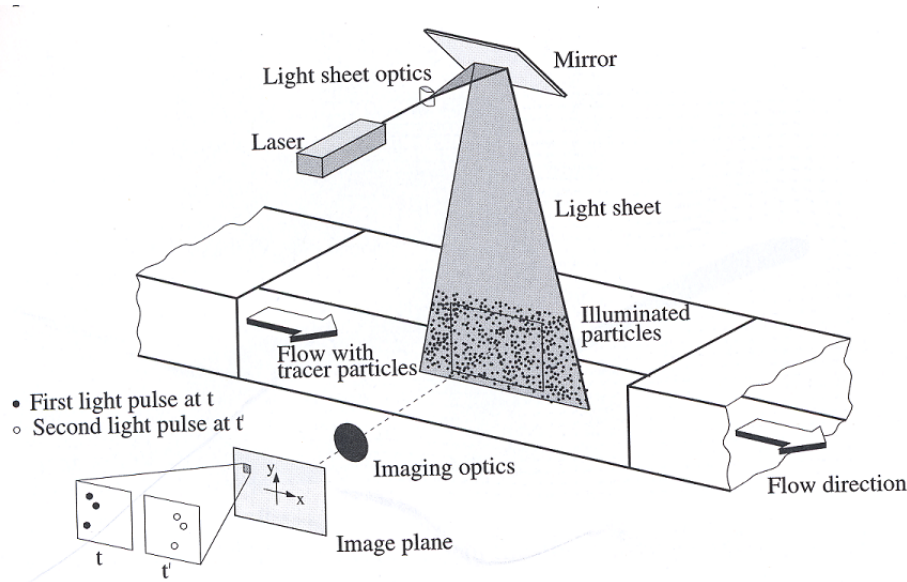


Figure 2.1: Principle components of PIV.

[3]

Selection of a light source also depends on the scattering characteristics of the particles used for seeding. If the particles used are smaller than the wavelength of light, the light is scattered according to Rayleigh's theory where the view angle is less important because the light is scattered more evenly in all directions. The energy incident on the sensor is accordingly less so detection of the particles becomes more difficult. For particles larger than the wavelength of the light, the light is scattered according to Mie theory where there is a preponderance of light scattered in the same direction as the incumbent light energy and less scattered backwards and to the sides. Figure 2.2 compares light scattering for Rayleigh and Mie theory. Table 2.1 lists most of the typical seed materials for air flow and their sizes. It is apparent that for PIV applications using Nd:YAG lasers, Mie scattering applies because the particles are typically larger in diameter than the wavelength of the light.

2.1.2 Flow Seeding. Table 2.1 shows common seeding types used for PIV measurements. The particles chosen for a specific test must be able to scatter sufficient light, but must also respond quickly to the dynamics of the flow being studied. Larger particles will scatter more light than smaller ones of the same material, but a larger particle has more momentum at the same velocity as the smaller one, meaning that



Figure 2.2: Rayleigh and Mie scattering characteristics.
[12]

Table 2.1: Common seeding materials for gas flows.

Type	Material	Mean diameter in μm
Solid	Polystyrene	0.5 – 10
	Alumina Al_2O_3	0.2 – 5
	Titania TiO_2	0.1 – 5
	Glass micro-spheres	0.2 – 3
	Glass micro-balloons	30 – 100
	Granules for synthetic coatings	10 – 50
	Diethylphthalate	1 – 10
	Smoke	< 1
Liquid	Different oils	0.5 – 10
	Di-ethyl-hexyl-sebacate (DEHS)	0.5 – 1.5
	Helium-filled soap bubbles	1000 – 3000

[3]

more force will be required to affect the particle's momentum. For a spherical particle of constant density, the mass increases with the cube of the radius, r^3 , whereas the viscous forces only act on the surface area of the sphere which increases with r^2 . Thus, the momentum increase with particle size is greater than the available aerodynamic force acting on the particle to change the momentum, thus larger particles will lag the dynamics of the air flow more than the smaller ones. Various forms of the Bassett-Boussinesq-Oseen (BBO) equation of motion for a spherical particle in a viscous fluid have been noted in the literature to characterize particle response [9]. Melling gives this equation as [13]:

$$\begin{aligned} \frac{\pi d_p^3}{6} \rho_p \frac{d\hat{U}_p}{dt} = & -3\pi\mu d_p \hat{V} + \frac{\pi d_p^3}{6} \rho_f \frac{d\hat{U}_f}{dt} - \frac{1}{2} \frac{\pi d_p^3}{6} \rho_f \frac{d\hat{V}}{dt} \\ & - \frac{3}{2} d_p^2 \sqrt{(\pi\mu\rho_f)} \int_{t_0}^t \frac{d\hat{V}}{d\xi} \frac{d\xi}{\sqrt{(t-\xi)}} \end{aligned} \quad (2.1)$$

If the density of the particle is much larger than the density of the fluid, as is the case with many seeding methods in air, the BBO equation can be simplified significantly to equation 2.2 [13]. The CO₂ density is assumed to be 1.18 g/cm³ based on previous work, so that this simplification is valid [10].

$$\frac{dv_p}{dt} = -C(v_p - U) \quad (2.2)$$

In equation 2.2 v_p is the particle velocity, U is the fluid velocity, and C is a characteristic frequency of the particle motion in terms of the drag coefficient and Reynolds number. For Stokes' resistance, the drag coefficient is given by $C_D = 24/Re_p$, yielding the following result for C :

$$C = \frac{18\mu}{\rho_p d_p^2} \quad (2.3)$$

For very small particles or rarefied flows, a Knudsen number correction can be applied to the drag coefficient to account for the ratio increase between the mean free path of molecules in the fluid to the particle's diameter. The drag coefficient would then be given by $C_D = 24 [Re_p (1 + Kn_p)]^{-1}$ [13]. In Greene's research, he compared his results using a drag coefficient with and without the Knudsen number correction and found that

the Knudsen number had very little effect [10]. For this reason, the Knudsen number correction is not used in the current research.

The Stokes' number is often defined as

$$St = \frac{\rho_p d_p^2 U C_{slip}}{18\mu L} \quad (2.4)$$

where U is the velocity, C_{slip} is a constant used to account for velocity slip in rarefied flow fields, and L is a characteristic length scale of the flow. Here, C_{slip} is approximately unity. In a turbulent flow, L is generally taken to be either the integral scale or Kolmogorov scale. In this study, however, the shock thickness is used to characterize the flow. Since this thickness is very small, the Stokes' number would increase toward infinity. So rather than utilizing Stokes' number to characterize the particle response, one goal of this project is to characterize the particles by another means.

2.1.3 Image Acquisition and Correlation. Image acquisition in PIV is accomplished primarily with digital cameras. CCD and complementary metal-oxide semiconductor (CMOS) sensors convert light energy into electrical energy that is recorded and processed to produce images. While CCD cameras typically have a higher resolution than CMOS, CMOS sensors are more sensitive to light, making them better suited for low light conditions. In either case, the shutter is typically open longer than the pulse of laser energy so low ambient light conditions are favorable for PIV. This reduces background noise and reflections in the images acquired. In the past, PIV images were collected on film, sometimes using a single exposure to capture both laser pulses. Today, digital cameras are able to capture two images in rapid succession, allowing the first image to capture one laser pulse and the second image to capture the next laser pulse. Digital processing allows for highly automated correlations of the two images using prepackaged software programs. A cross-correlation method splits the image into small subregions, called interrogation regions (IR), and then uses a fast Fourier transform (FFT) on each IR. The signal strength for a single IR is compared between the first and second image to determine a mean displacement between the two peaks. The correlation produces a

vector for that IR, and then the next IR is processed. This process is shown in Figure 2.3 below.

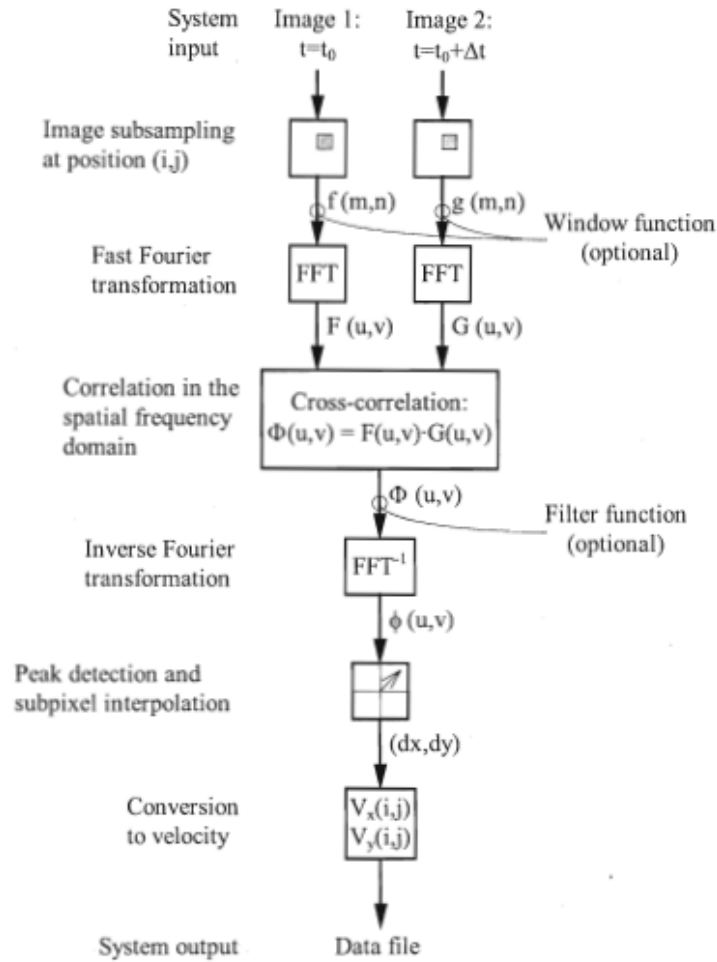


Figure 2.3: Diagram of the cross correlation process.

[14]

2.2 Discrete CO_2 Particle Formation and Characterization

The process of forming discrete CO_2 particles has been well documented in work preceding this research [7, 8, 9]. Pressurized liquid CO_2 flows through an expansion nozzle at which point some of the liquid evaporates and cools rapidly. The cool gas drops the temperature of the remaining liquid spray, freezing it into solid particles that can agglomerate to form variously-sized discrete particles. Initially, this method for forming particles was applied to the cleaning of substrates, as patented by Whitlock,

Weltmer and Clark [15]. In 2006 DeLapp, Reeder, Crafton and Goss proposed using these particles to seed air flow for PIV measurements [7]. Their work initially used a commercial off the shelf dry ice cleaning system called the Sno-Gun II to generate CO₂ particles. The particle stream was passed through a Malvern particle size analyzer using different nozzle sizes, resulting in sizes typically ranging from 5 to 15 μm .

McNiel continued and built upon the work of DeLapp and assessed whether or not discrete particles could be generated and inserted into the air flow of a wind tunnel for PIV measurements [8]. McNiel studied two different injection methods: a capped, multi-port shroud tube and a simple, uncapped shroud tube. He also used these two injection methods in two different locations: the stilling chamber and the sidewall of the converging-diverging nozzle. McNiel found that using a multi-port injection method was unsuccessful in forming discrete particles from either location and instead, gaseous CO₂ clouds were present in the test section. Using the simple shroud tube, he successfully generated discrete particles that persisted through the test section at the nozzle injection point [8].

The work of Peltier, in addition to McNiel's work, explored many combinations of injection location and method, moving away from the Sno-Gun apparatus and using a combination of small and large tubes to constrict and expand the liquid CO₂ in a controlled fashion [8]. Greene used the results of this previous work and studied the effects of varying the size of the feed tube and the shroud tube diameters, as well as the addition of a coflow of air to the CO₂ spray [9]. Another variable Greene looked at is the effect insulating the tubes had on particle size. His work using the particle size analyzer found that lengthening the shroud tube, increasing the shroud tube inner diameter (ID), decreasing the feed tube ID, and insulating the shroud tube each effectively increased the size of particles generated [10]. Conversely, particle size would decrease if any of these changes were reversed. The addition of a coflow of air decreased the particle size but the net effect was a reduction in the particle number density in the test section. Greene focused on injecting particles and collecting PIV data in the AFIT 2.5 inch by 2.5 inch pressure-vacuum supersonic wind tunnel with great success. His attempt to scale the injection system up to the larger 6 inch by 6.5 inch supersonic blowdown tunnel was met

with some success. However, particle number density was lower than that observed in the smaller tunnel. He attributed this to the increase in air mass flow rate for the larger tunnel and the increased distance between the injection point and the test section, which in turn, increased the required residence time for the particles to persist through the test section [9].

2.3 Particle Size Analysis

The behavior of light when it interacts with particles allows a passive means for determining particle size. Light impinging on a particle will be scattered in a well known manner depending on the wavelength of the light and the size of the particle. If the wavelength is known and an array of sensors are used to detect the scattered energy from a particle, then the size of the particle can be deduced. This method is exploited by particle size analyzers which shine a laser across a known distance to a lens. The lens focuses the light on the center of a ring detector. When something such as a particle disrupts the path of the light, the light will diffract and impact a different detector. To arrive at a particle size, however, the shape is assumed spherical because a sphere is the only shape that can be uniquely defined by a single number, namely its diameter. For particles that are not spherical, the true size will be different than that found by size analyzers, which instead provide an equivalent spherical size. Greene documented that the Sauter mean diameter, D_{32} , was a useful product in arriving at a mean particle diameter [10]. It is calculated by summing the cube of the diameters and then dividing this by the sum of the diameters squared to obtain a mean particle diameter, as seen in equation 2.5 [16].

$$D_{32} = \frac{\sum_{i=1}^N n_i D_i^3}{\sum_{i=1}^N n_i D_i^2} \quad (2.5)$$

D_{32} is the mean diameter of an equivalent sphere that has the same volume/surface area ratio as the particles being measured. In general, the Sauter-mean diameter is commonly used in experimental studies [17].

2.4 High Speed Wind Tunnel Testing

Wind tunnels are used to simulate actual flight in a controlled environment, thereby providing a means for acquiring data without subjecting the test to undue risks. Uniform air flow at subsonic, transonic, and supersonic speeds can be achieved at variable conditions for easy prediction of aerodynamic characteristics in a real environment.

2.4.1 Tunnel Design. All tunnels operate by creating a pressure gradient across a control volume to induce air flow from high to low pressure. High pressure can be created by using fans, compressors, or a supply of compressed air that is released into the lower ambient pressure through the tunnel. Some systems combine this with a vacuum system to further increase the pressure differential. Systems that use supplies of compressed air and/or vacuums to achieve the flow cannot run continuously because they exhaust their supply of compressed air, whereas systems that use compressors can run continuously. To achieve supersonic flow, it is necessary to design a compressor-diffuser nozzle through which the air must flow. When the pressure differential is large enough, the flow will choke at the throat of the nozzle causing a normal shock to form. The air then expands and accelerates based on the ratio of the area of the test section to the area of the throat. The volume upstream of the throat is often referred to as the stilling or stagnation chamber, and if the air properties are known inside this region, the properties of the flow through the tunnel can easily be calculated using the following relations:

$$\frac{P}{P_0} = \left(1 + \frac{\gamma - 1}{2} M^2\right)^{\frac{-\gamma}{\gamma - 1}} \quad (2.6)$$

$$\frac{\rho}{\rho_0} = \left(1 + \frac{\gamma - 1}{2} M^2\right)^{\frac{-1}{\gamma - 1}} \quad (2.7)$$

$$\frac{T}{T_0} = \left(1 + \frac{\gamma - 1}{2} M^2\right)^{-1} \quad (2.8)$$

2.4.2 *Mass Flow.* The conservation of mass can be used to determine the mass flow of air, \dot{m} , through the wind tunnel using equation 2.9.

$$\dot{m} = \rho U A \quad (2.9)$$

The density, ρ , can be found using equation 2.7, and the area, A , is known from the tunnel geometry so all that is needed is the velocity, U . Using pressure transducers in a wind tunnel, the pressure ratio P_0/P can be measured so that equation 2.6 can be solved for Mach number:

$$M = \sqrt{\frac{2}{\gamma - 1} \left[\left(\frac{P_0}{P} \right)^{\frac{\gamma - 1}{\gamma}} - 1 \right]} \quad (2.10)$$

Since the Mach number is defined as $M = U/a$ with the speed of sound defined as $a = \sqrt{\gamma RT}$, the velocity can be calculated. Thus the mass flow rate of air can be found using pressure and temperature measurements in the tunnel.

2.4.3 *Isentropic Relations.* Previous work by Greene looked at a 10° ramp in the AFIT 2.5 inch by 2.5 inch pressure-vacuum wind tunnel, so for similarity, the same will be done for this research in the larger 6 inch by 6.5 inch blowdown wind tunnel. The ramp with known deflection angle, θ , will cause an oblique shock wave at an angle β . If the speed of the flow is known, then the well known $\theta - \beta - Mach$ relation given by equation 2.11 can be used to determine the shock angle.

$$\tan \theta = 2 \cot \beta \frac{M^2 \sin^2 \beta - 1}{M^2 (\gamma + \cos 2\beta) + 2} \quad (2.11)$$

Knowledge of both the upstream Mach number and the shock angle provides the necessary information to determine the velocity normal to the shock upstream and downstream of the shock wave using isentropic relations. First, the Mach number normal to the shock is simply computed and then used to determine the Mach number downstream and normal to the shock.

$$M_{n,1} = M_1 \sin \beta \quad (2.12)$$

$$M_{n,2}^2 = \frac{1 + \left(\frac{\gamma-1}{2}\right) M_{n,1}^2}{\gamma M_{n,1}^2 - \frac{\gamma-1}{2}} \quad (2.13)$$

Finally the true Mach number downstream of the shock can be calculated using the following:

$$M_2 = \frac{M_{n,2}}{\sin(\beta - \theta)} \quad (2.14)$$

2.5 Schlieren Imaging

“Light propagates uniformly through homogeneous media” but small disturbances due to temperature variations, turbulence, convection, weather phenomena or shock waves in air affect the density of the air, thereby changing its refractive index [18]. Air has a refractive index of approximately $n = 1.0003$ but localized disturbances can change this slightly, varying with density linearly according to the simple relationship from Settles [18]:

$$n - 1 = k\rho \quad (2.15)$$

The Gladstone-Dale coefficient, k , is about $0.23 \text{ cm}^3/\text{g}$ for air at standard conditions [18]. Since the speed of light through a media other than a vacuum is proportional to the index of refraction according to equation 2.16, then a change of the refractive index due to a density gradient affects the speed light traverses through that media, causing a phase shift.

$$\lambda\nu = \frac{c}{n} \quad (2.16)$$

Here, λ is the wavelength, ν is the frequency, and c is the speed of light. An example of this is easily observed when looking at an object through the heat rising off a flame. These gradient disturbances are known as schlieren and they bend the light slightly, typically too little to be seen by the naked eye. If, however, collimated light is passed through the schlieren and then focused to a point by a lens, the schlieren will change the path of the light through the lens, causing a change in the point at which the light focuses. By placing a knife edge at the true focal point of the lens, portions of the bent light are blocked by the knife edge, causing a shadow to form against an otherwise bright

background. This is demonstrated in the simple diagram from Settles, seen in Figure 2.4.

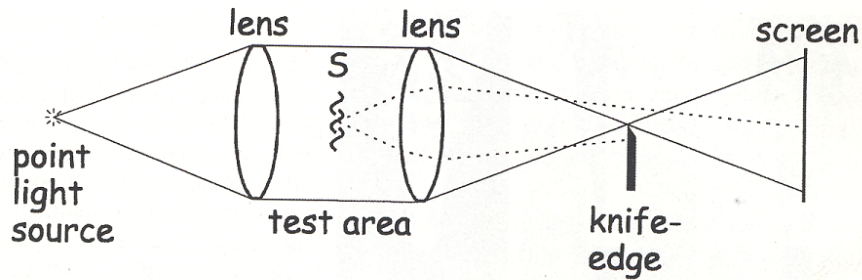


Figure 2.4: Diagram of a simple schlieren system with a point light source.

[18]

A popular arrangement is the *z-type* Herschellian system shown in Figure 2.5 because mirrors can provide a larger field of view than lenses of equal cost [18]. Light is condensed through a slit positioned at the focal point of a parabolic mirror such that the reflected light is collimated. The light then passes through the area of interest and is bounced off another mirror and is focused onto the knife edge, blocking part of the light. A camera captures the light which passes through as well as the shadows caused by any disturbances in the path of the light.

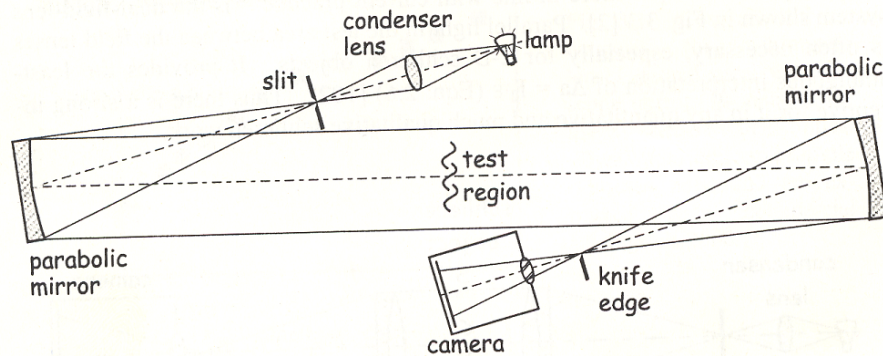


Figure 2.5: Diagram of a Herschellian schlieren system.

[18]

III. Methodology

THIS chapter discusses the test equipment and test procedures used for the various stages of testing. First, the method for generating dry ice particles is discussed, because it is vital to this research effort. Next, the experiments in particle size analysis and PIV conducted at AFIT are discussed. Finally, the testing conducted at AFRL using the TGF is discussed.

3.1 Particle Generation

Liquid CO₂ (LCO₂) stored in commercially available dewars is used throughout the research. The dewars measure 180 liters in volume and are pressurized at approximately 2413 kPa at room temperature. The LCO₂ evaporates into gaseous CO₂ inside the dewar which in turn supplies the necessary head pressure to maintain the remaining CO₂ in the liquid form. The pressurized LCO₂ flows through a siphon under its own pressure, through a length of high pressure flexible stainless steel Swagelok[®] hose as well as stainless steel or brass compression fittings, attaching to the feed tube. The feed tubes all measure 1/8 inch outer diameter (OD) and varied in ID. The feed tube was then connected to varying sizes and types of shroud tubes. Some of these tubes are shown in Figure 3.1. This junction between the feed and shroud tube is the point at which the expansion process ideally begins, allowing the LCO₂ to rapidly decrease pressure and temperature, forming solid CO₂ particles. While resident in the shroud tube, the particles agglomerate and increase in size until they exit the tube.

Two different types of shroud tube were used: a simple stainless steel cylindrical tube and a heat exchanging concentric tube inside a tube with a Kenics[®] static mixer element inside the inner tube. The static mixer, shown in Figure 3.2, is commonly used in the process industries to reduce particle size in liquid-liquid and liquid-gas dispersions [19]. There is much less information on its use in a solid-gas dispersion, however. The alternating helical mixing elements direct the flow to the outer wall and thoroughly mix the fluid, as well as increase heat transfer to the outer wall. Temperature controlled walls through the use of a heat exchanging fluid bath can increase or decrease this energy transfer rate, thereby affecting particle size.

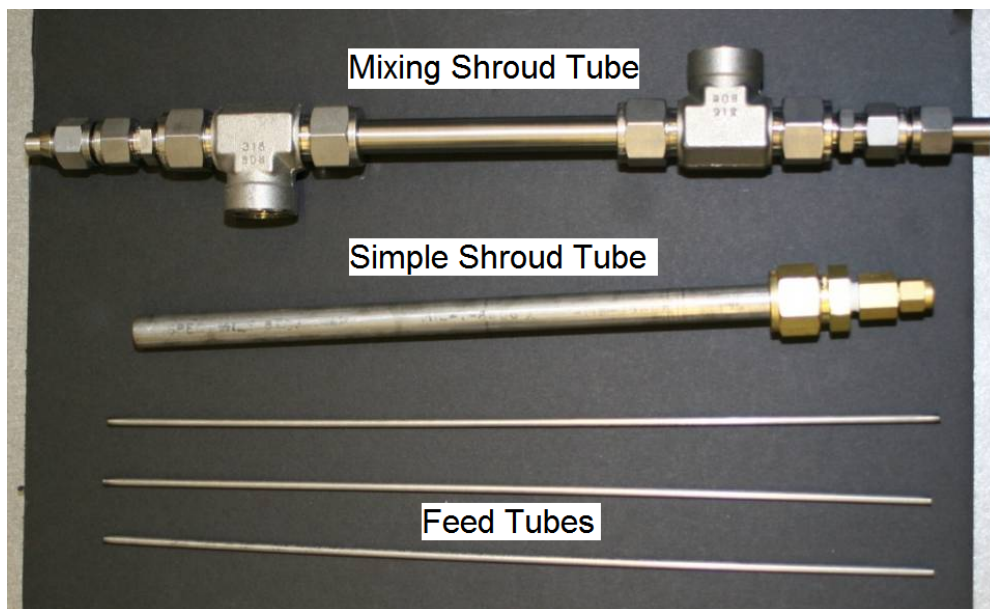


Figure 3.1: Feed and shroud tubes used during experimentation.



Figure 3.2: Kenics® static mixer.

[19]

3.2 Particle Size Analysis

Particle size data was collected using the Malvern Spraytec particle size analyzer identical to that used by Greene and Delapp [7, 9]. The Spraytec was set up in an open air environment, exposed to ambient temperatures and pressures. Different injection tube combination were used to obtain comparative size measurements.

Table 3.1 shows the different combinations of feed tubes and shroud tubes used, as well as fluid temperature of the mixing tube heat exchanger. In each case the exit plane of the shroud tube was held at a constant relative position to the laser beam. The perpendicular distance from the tube exit to the laser was kept at four inches and the intersection of the injector longitudinal axis and the laser beam axis was kept at 5.5 inches from the optics housing, as shown in Figure 3.3. Greene found that placing the particle stream closer to the receiver optics provided more reliable results [10].

The particles being analyzed were solid CO₂ at temperatures well below the ambient air temperatures, so even at low relative humidity, water vapor in the air could condense on the particles, increasing their size. To minimize the effect of humidity on the particle size analysis, a coflow of conditioned dry air was supplied through an Alicat Scientific mass flow controller. The supply pressure of the dry air limited the coflow to 47 SLPM through the mass flow controller. This air supply also provided clean air for the Spraytec optics, reducing the air available to minimize humidity effects on dry ice crystals through the laser beam.

Table 3.1: Feed and shroud tube sizes

Shroud Tube ID (in)	Feed Tube ID (in)	Temperature (°C)
0.33	0.03	N/A
	0.055	N/A
	0.068	N/A
0.31 (Mixing)	0.055	N/A
	0.068	N/A
	0.068	30
	0.068	40
	0.068	50
0.40	0.068	N/A

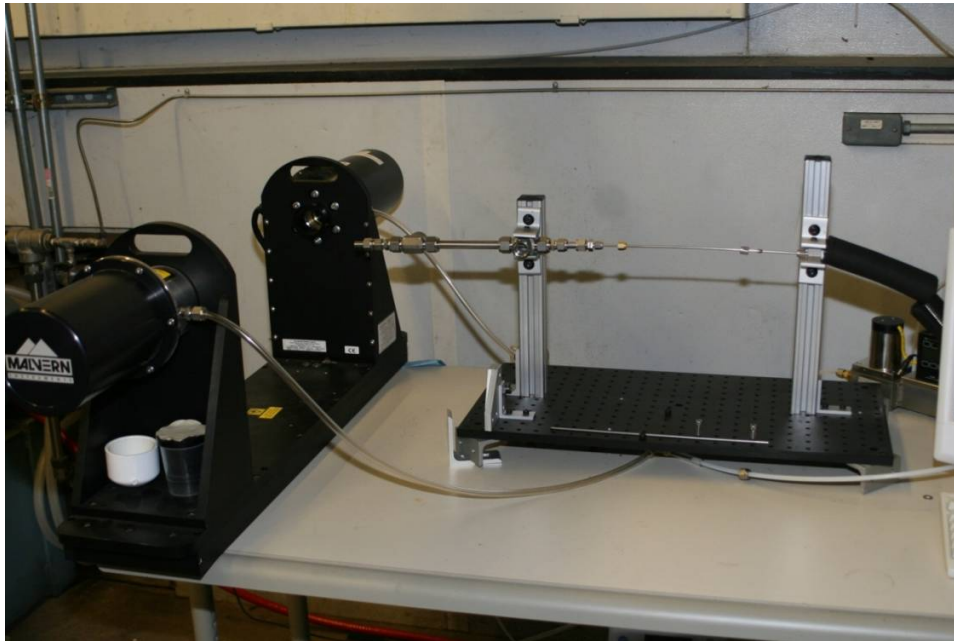


Figure 3.3: Malvern Spraytec particle size analyzer setup.

Operation of the Spraytec was relatively straightforward. After system initialization, a background noise measurement was taken with the laser and air supply on and without particles present. Background noise on each receiving ring is subtracted automatically from the signal during actual measurements to improve accuracy. When ready to perform measurements, a time history file was opened and the laser turned on. A CO₂ dewar was connected by hose to the injector tube via stainless steel and/or brass compression fittings and the dewar valve was opened to allow flow of liquid CO₂ to the tubes. Each test point was run between 30 seconds and one minute, depending on the observed steadiness of the flow. In some instances, more likely with the mixing tubes, the solid and gaseous CO₂ would sporadically clog for seconds at a time and then release, requiring more time to collect sufficient data.

For test points using the static mixing shroud tube, a Thermo Scientific NESLAB RTE Series refrigerated bath as seen in Figure 3.4 supplied fluid flow through the heat exchanging element of the shroud to maintain a constant shroud temperature. Deionized, distilled water was fed through flexible plastic tubing to the heat exchanger and then back to the bath to be reconditioned at the desired temperature.



Figure 3.4: Refrigerated bath filled with deionized, distilled water for heat exchange.

3.3 AFIT Wind Tunnel Tests

3.3.1 Wind Tunnel. Prior to its use, the AFIT variable throat 6 inch by 6.5 inch supersonic blowdown tunnel shown in Figure 3.5 was reconfigured with a new test section to provide cleaner flow than previously present. The variable throat was held constant throughout testing and set so that Mach 1.92 flow was maintained through the test section. For similarity to previous work, a 10° ramp was chosen to provide a two-dimensional oblique shock for study. Rather than redesign the tunnel floor to incorporate this ramp, a rapid prototyping Machine was used to build a ramp that would fit in the existing tunnel floor. Once configured with a 10° ramp, the tunnel was ready for use.

The tunnel was supplied with dry air by a tank pressurized to approximately 180 psi. A gate valve maintained a seal upstream of the wind tunnel when not in use. To operate the tunnel, this gate valve was opened manually. This pressurized the supply line to the tunnel which was then kept pressurized by a pneumatic butterfly valve. The butterfly valve was operated and electronically controlled by a Fisher[®] system. The user could specify a set point pressure for the stagnation chamber and through use of a pressure transducer in the chamber, the controller would operate the butterfly valve to maintain the set point pressure. When the supply pressure dropped below the specified set point pressure, the valve would close automatically. If desired, the user could



Figure 3.5: AFIT 6 inch by 6.5 inch supersonic blowdown wind tunnel.

manually open and close the valve as well. When collecting PIV data during this experiment, a set point pressure of 40 psi was used. Once initiated, the process of opening the butterfly valve took approximately 10-15 seconds to reach the set point pressure and then maintained this condition for approximately 20 seconds before the air supply was exhausted and the valve closed.

3.3.2 Schlieren. Schlieren video was used to monitor the upstream flow conditions and to assess whether or not the new test section of the tunnel provided clean flow. After several runs of the tunnel, however, it became apparent that the schlieren provided the best means of determining when the supersonic flow was steady. With limited run time of the tunnel, it was necessary to obstruct the field of view (FOV) of the schlieren so that it did not impact PIV data collection. Therefore, the schlieren setup only captured a small portion of the flow immediately upstream of the PIV FOV. The approximate FOV is shown in Figure 3.6. Light for the schlieren setup was emitted from a mercury short arc HBO[®] light that passed through a lens to focus the light down to a point through an iris to pass only this point source of light. The iris was placed at the focal point of a concave mirror to reflect and collimate the light for passage across the wind tunnel

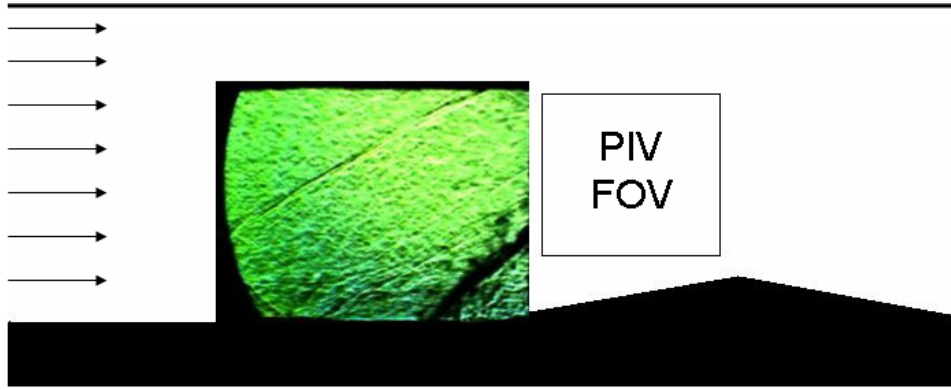


Figure 3.6: Approximate location of the field of view for the schlieren and PIV camera. Both a weak shock caused by a junction in the tunnel floor and the shock caused by the wind tunnel ramp are visible.

test section. The mirrors used were both 10 inches in diameter with a focal length of 80 inches. The second mirror reflected the light down to a point at which a vertical knife edge was placed to reduce the light intensity evenly across the image, allowing shadow visualization of the density gradients in the light path. A Photron Fastcam-X 1280 PCI camera captured the images at a frame rate of 1000 frames per second and an exposure duration of approximately $7.8 \mu\text{s}$, and then they were recorded by the Photron software system on a Compaq computer. Recording was manually initiated at the start of each run and halted when the system reached its capacity. The setup of the schlieren followed the z-type Herschellian system shown in Figure 2.5.

3.3.3 PIV System. A Dantec Dynamics PIV system was used to acquire data in the AFIT wind tunnel. The laser source was a New Wave Research Solo 200XT Nd:YAG frequency doubled laser operating at 532 nm and a maximum power of 200mJ. An optical arm consisting of a series of optics was used to manipulate the laser beam for positioning above the wind tunnel and to spread the beam into a planar laser sheet approximately 4mm wide. Images were captured by a FlowSense 4M CCD camera with a 2048 x 2048 pixel array outfitted with a Nikkor 60 mm f2.8 lens and then fed to the Dantec Dynamic Studio software package for recording. The software also provided control of the camera and laser triggering functions. This system was set up to capture particle motion in air flow across a shock generated by a 10° ramp using a vertical laser

sheet aligned with the focal plane of the camera, positioned perpendicular to the flow direction, with flow from left to right as seen in Fig. 3.7. After positioning the laser and optical arm such that the laser sheet was located in the center of the tunnel and aligned with the flow direction, a calibration grid was aligned with the laser sheet to focus the camera and scale the field of view. Figure 3.8 shows the calibration image used. The grid imaged is of known distance so a scale factor can be calculated to determine the relative size each pixel captures on the focal plane. Performing this process resulted in an image of the flow field with a field of view that measured 77.8 mm by 77.8 mm, giving a resolution of 26.3 pixels per millimeter. This translated to a scale factor of 5.096 in the Dantec software. To ensure the camera was properly focused and to test the system setup, an injector was placed on top of the wind tunnel and angled downward to direct the CO₂ particles into the test section through the PIV FOV. Figure 3.9 shows this arrangement. For wind tunnel runs and PIV data collection, image pairs were collected using a 1 μ s delay and a repetition frequency between 2-4 Hz. For the flow conditions of the wind tunnel, the system timing equated to a particle displacement of about 12 pixels in the freestream.

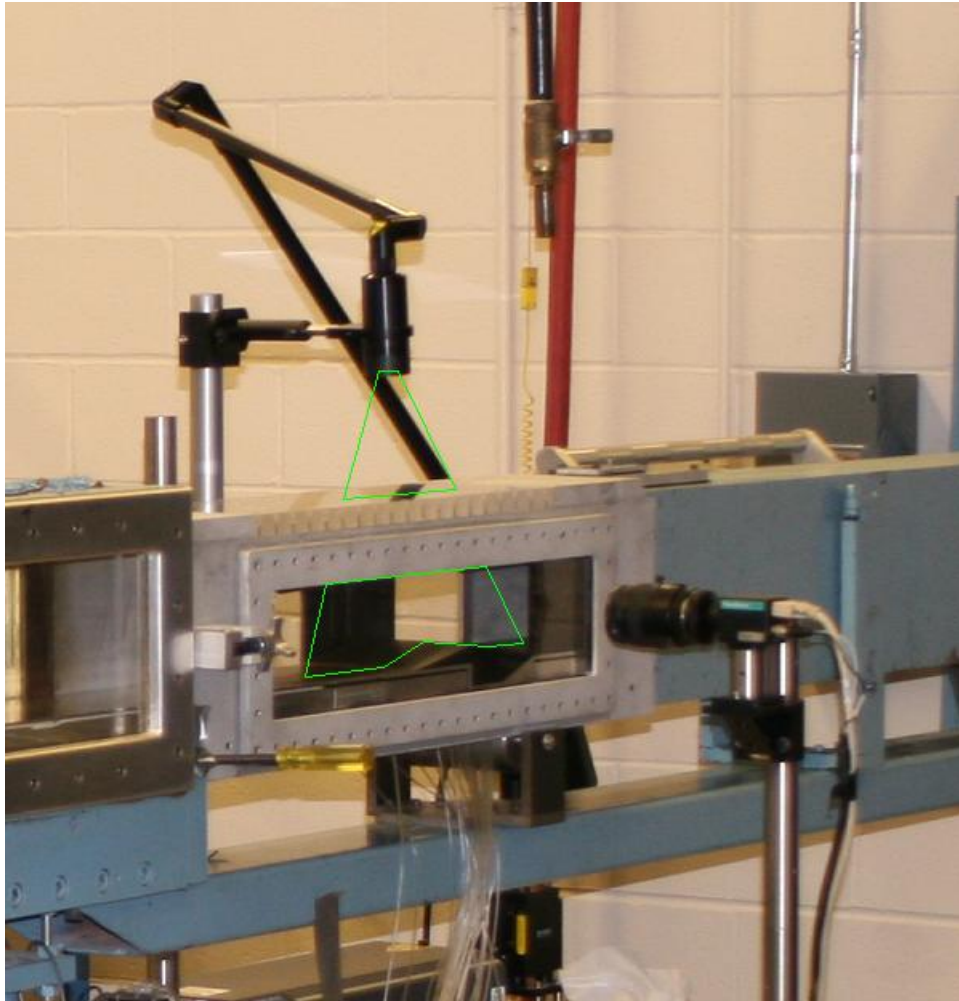


Figure 3.7: Laser and camera setup for PIV measurements in the AFIT 6 inch by 6.5 inch wind tunnel.

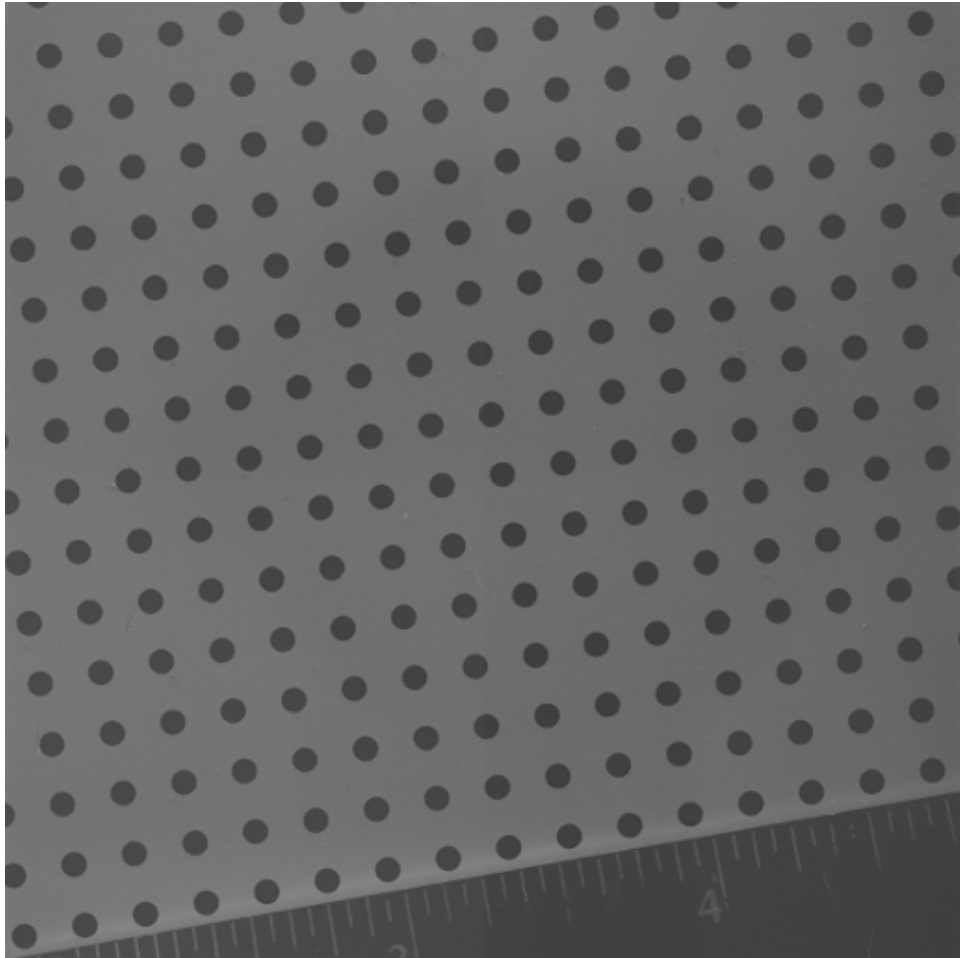


Figure 3.8: Calibration grid imaged to scale the field of view.

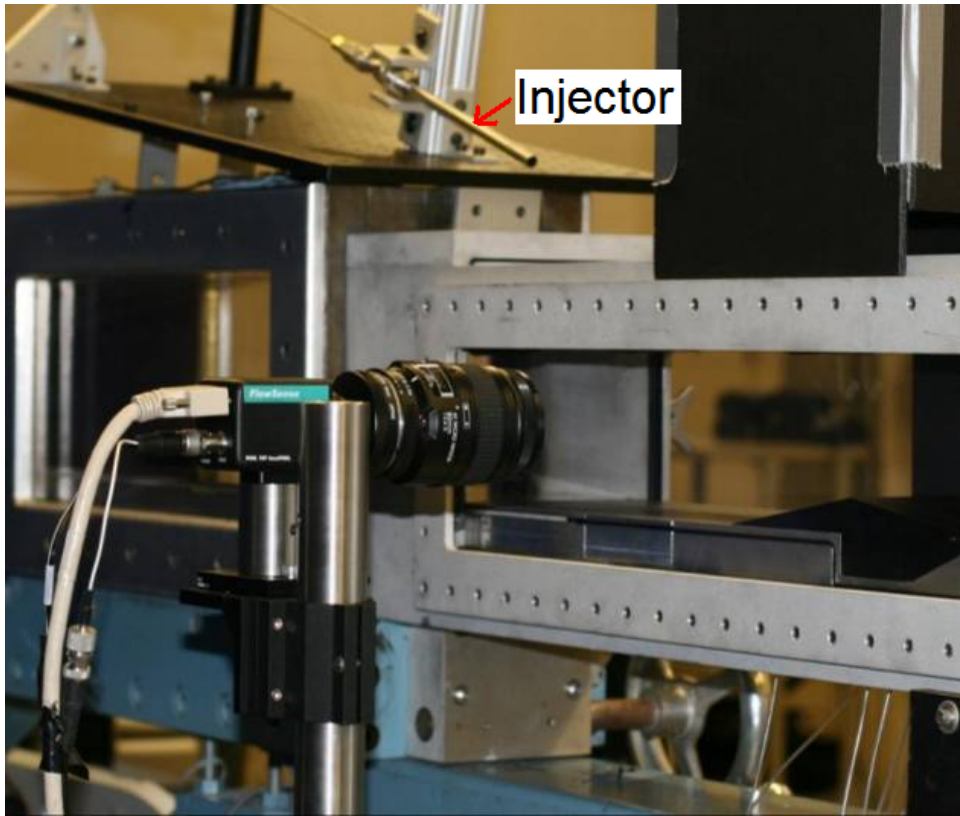


Figure 3.9: Injection from above the test section used for system checkout.

The recipe for processing the image pairs began with a cross-correlation using two different interrogation region (IR) sizes: 64 by 64 pixels (2.43 mm by 2.43 mm) and 32 by 32 pixels (1.22 mm by 1.22 mm). The full image was processed with these IR sizes using a 50% overlap for the 32² pixel IR and a 75% overlap for the 64² pixel IR. A Gaussian window function using equation 3.1 was applied to attenuate the signal strengths closer to the edge of the IR, thereby weighting the correlation towards the signal near the center of the IR [14]. In equation 3.1 the coefficient k determines the width of the window function, and for this research $k = 1.19$ was used. The weight, W , was determined using the pixel location, (m, n) , and the IR size, (M, N) . A No-DC filter was also applied to remove the background noise to effectively enhance the signal-to-noise ratio [14]. The correlation was followed by a peak validation using a value of 1.1 and a range validation to remove outlier vectors. Since the range of flow speeds were known from pressure transducer data in the tunnel as well as visual correlation of particles in the image pairs, the range of vectors passed was restricted to 200-600 m/s for the streamwise component of velocity (U) and -100 to 100 m/s for the vertical component of velocity (V). Finally, averages were calculated for each condition using only vectors that had passed both the peak and range validation methods.

$$W(m, n) = \exp \left[- \left[\frac{1}{k} \right]^2 \left(\left(\frac{2m}{M} \right)^2 + \left(\frac{2n}{N} \right)^2 \right) \right] \quad (3.1)$$

In equation 3.1, W = weight value; (m,n) = pixel location; k = window function width coefficient; and (M,N) = interrogation region size.

3.4 AFRL Wind Tunnel Tests

3.4.1 Trisonic Gas-dynamics Facility. The AFRL Trisonic Gas-dynamics Facility (TGF) is a closed loop, variable density, continuous flow wind tunnel with a 2 feet by 2 feet (0.61 m by 0.61 m) test section (Figure 3.10). It uses interchangeable nozzle blocks to operate in the subsonic, transonic and supersonic regimes. In this test only the subsonic nozzle block was used, providing the performance characteristics seen in Figure 3.11. The tunnel was operated by Shawn Raisch, Paul Olekas, and Rick Zimmer-

man from Jacobs Engineering. A LaVision PIV system was arranged and operated by Dr. Ryan Schmit with assistance from Tom Presdorf, PE (AFRL/RB) and Dr. Aaron Altman (University of Dayton). Dry ice experiments were performed on the same days as tests of a Vicount system, beginning on 29 January 2010 and ending on 5 February 2010. The tunnel was configured with CO₂ injectors in four locations; three in the stagnation chamber and one just upstream of the test section. Figure 3.12 shows two of the three injecting into the wall of the stagnation chamber and Figure 3.13 is a view looking upstream from the test section showing the fourth injector. The TGF was used on two separate days, first to assess successful generation and persistence of particles through the test section, and second to perform PIV using the CO₂. For day one, three combinations of feed and shroud tubes were used, each at a different location in the tunnel. Each injector was used individually at each test condition shown in Table 3.2. The best seeding observed during this test would then be used for PIV on the second day.

Table 3.2: Test conditions for TGF.

Mach Number	Pressure (PSF)
0.89	255
0.79	501
0.5 (approx.)	500
	1000
	1500
0.30	516
0.30	1006
0.30	1506

3.4.2 PIV System. The PIV system used for TGF testing consisted of a LaVision computer and software package, a PCO camera, and a New Wave Research Solo PIV Nd:YAG laser. For the first day the system was set up with two cameras, one on either side of the tunnel, capturing different regions of the tunnel. Because it was not known where the particles would appear in the tunnel field of view, the laser provided a sheet of light across the tunnel vertically such that the flow direction was normal to the laser sheet. This provided the maximum coverage of the tunnel test section to strictly observe particles, thus no velocimetry data was collected. For the second day of testing,

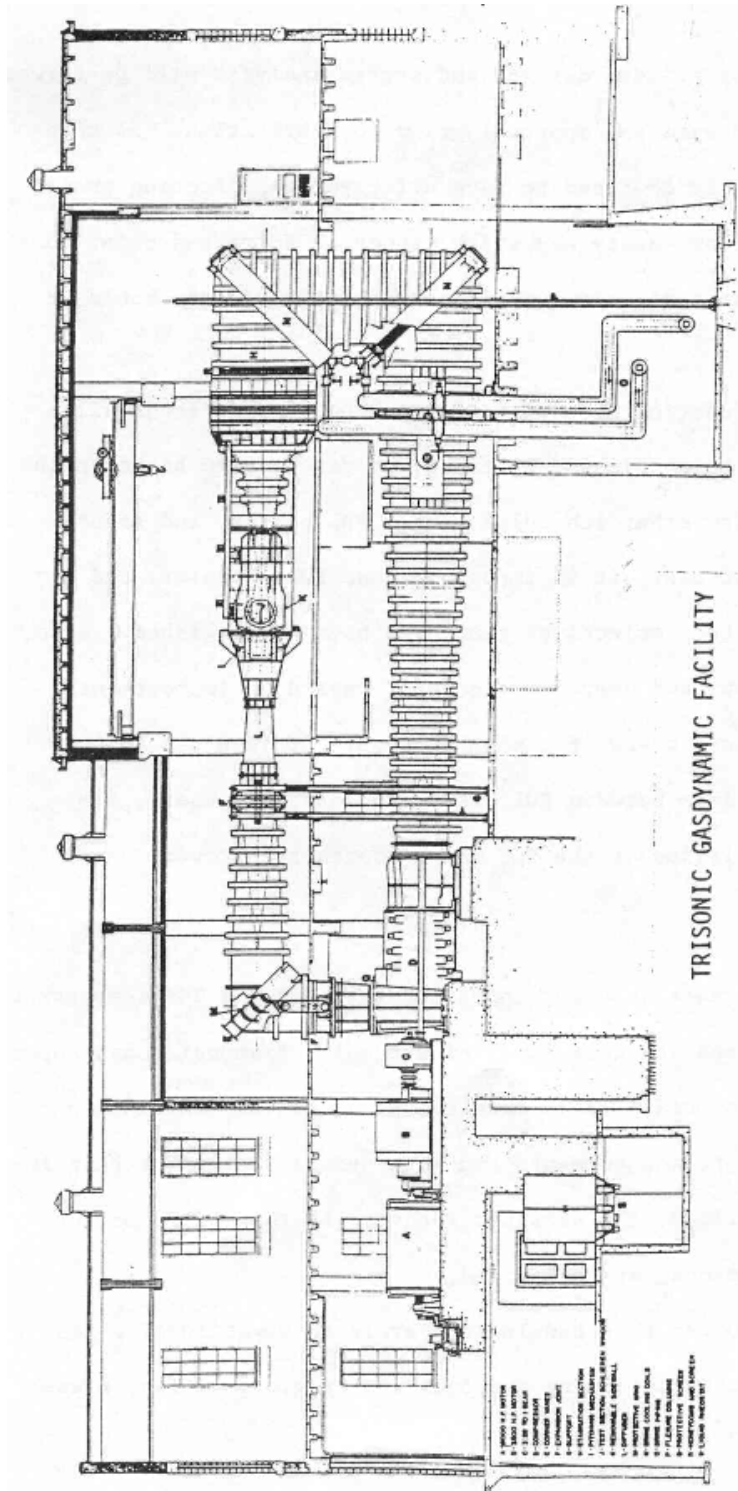


Figure 3.10: Side view of the TGF.

[20]

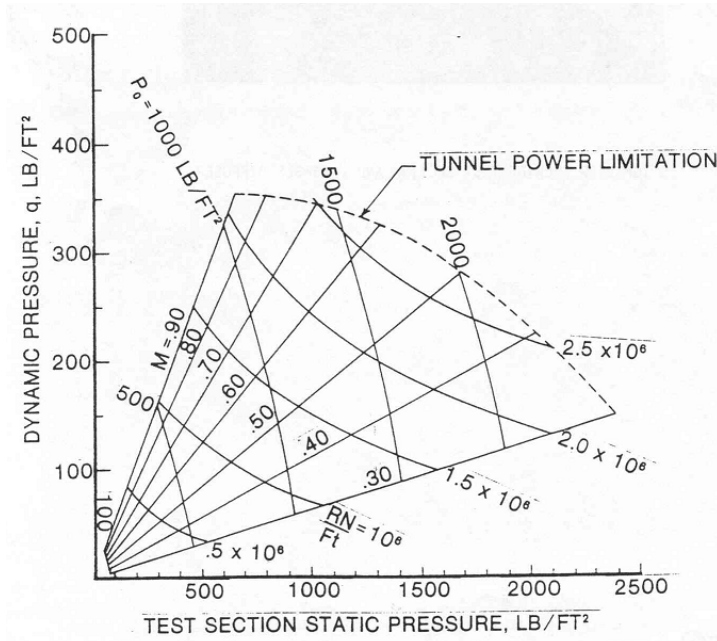


Figure 3.11: TGF subsonic test section performance chart.

[20]

the laser sheet was rotated to be in plane with the flow direction. The geometry of the TGF limited the camera FOV such that the only way to collect images perpendicular to the laser sheet was to bring the laser sheet through the tunnel at an angle. In this arrangement, the camera was approximately 90° from the laser plane, though this plane did not align with standard coordinate frames. At each test condition shown in Table 3.2, the LaVision system captured 100 image pairs. The image pairs were then processed using a similar cross-correlation technique. Differences in the software did not allow identical post processing, but in this case a range validation was applied to the streamwise velocity component. Vectors with a streamwise velocity outside the ranges specified in Table 3.3 below were not used in the mean velocity computations.

Table 3.3: Range validation for TGF data.

Min (m/s)	Expected Mach/speed	Max (m/s)
25	0.3/100	175
100	0.5/170	300
150	0.8/270	350

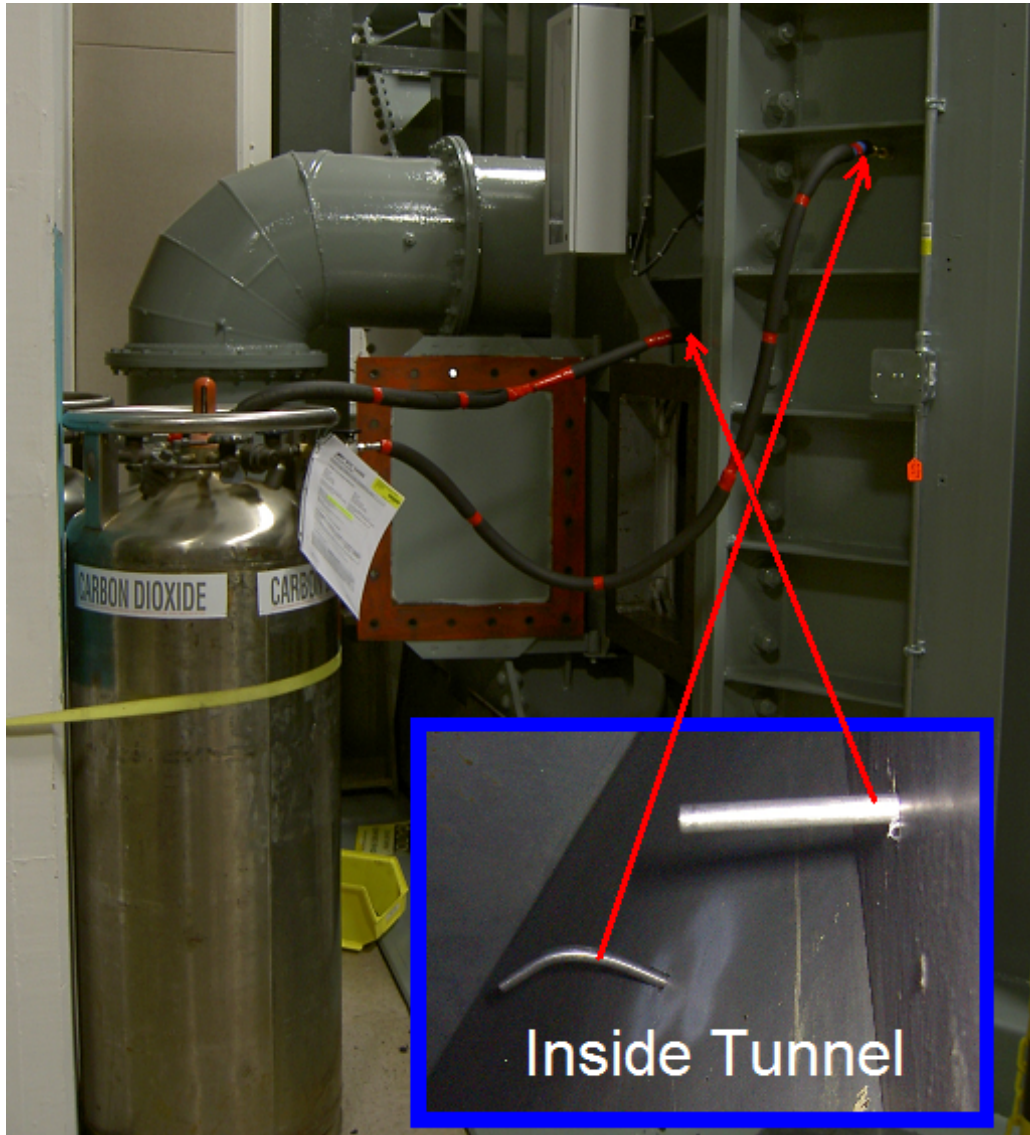


Figure 3.12: Exterior view of CO₂ injectors in the stagnation chamber wall of the TGF with an interior view inset looking up from the access door.

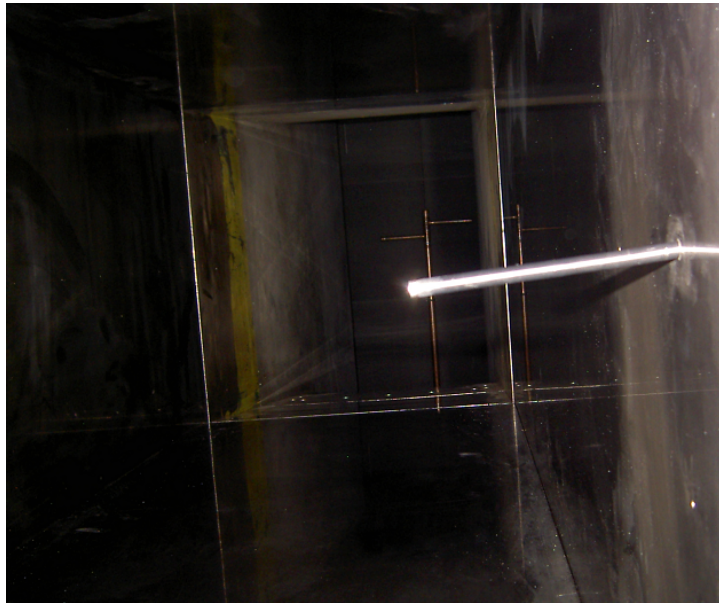


Figure 3.13: View of test section injector, looking upstream towards stagnation chamber.

IV. Results and Discussion

RESULTS for testing conducted at AFIT and AFRL are presented below. First, the particle size analysis conducted at AFIT is presented. Based on these results, particular configurations were chosen for insertion into the AFIT wind tunnel. PIV results are next presented for the AFIT tunnel testing. Finally, results for testing conducted at the AFRL/RB TGF is presented.

4.1 Particle Size Analysis

Particle size analysis was accomplished using the Malvern Spraytec. The CO₂ was run approximately 45 seconds through the laser for different configurations of feed and shroud tubes and data was recorded by the RTSizer software. Because of the differences in environments between where the Spraytec was used and where the particles will be needed (wind tunnel), the particle size information presented is for relative comparative information rather than for true particle size information. In each case the Sauter mean diameter, D_{32} , was chosen to give representative particle size information based on Greene's results that showed this was a good indicator of size [10]. To arrive at each value, random snapshots of the recorded data were exported and the mean and standard deviation of these discrete measurements were calculated. Particle dispersion is addressed and the effects due to the feed tube ID, shroud tube ID, shroud tube type, and heat exchanging fluid bath temperature are compared below.

Though mean diameter data is presented, it is not without error in addition to the standard deviation of the data points shown. The CO₂ particle size distribution was nonuniform, so even though a single number is presented to describe the particles at each test condition, the actual particles varied significantly. In most cases, the percent number of particles was greater for the smaller particles than larger ones, but larger particles made up the majority of the percent volume measurement. The percent number and percent volume measurements from the size analyzer were used to determine the Sauter mean diameter, but it is just a calculation of a particularly sized particle spray that would have the same volume to surface area ratio as the actual spray. Figures 4.1 and

4.2 are typical distributions of the particle number and volume. So, even though the mean particle size was in the range presented, a large variation of size was present.

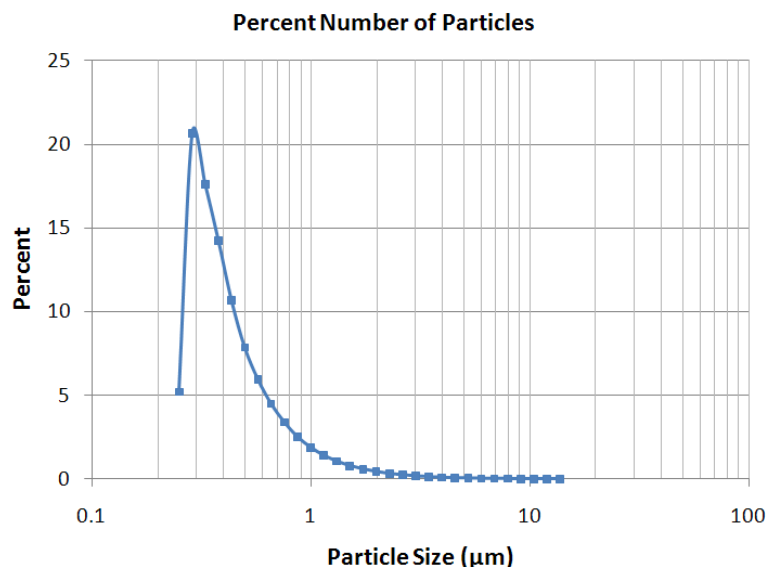


Figure 4.1: Percent of total number of particles measured at each particle diameter.

4.1.1 Particle Dispersion. Two different types of shroud tube were used for measurements: a simple shroud tube (Figure 4.3) and a static mixing shroud tube (Figure 4.4). There was a strong difference in the dispersion of CO₂ as it exited the tube. Figures 4.3 and 4.4 show the visible difference in the spread angle as the particles sprayed out. In Figure 4.3 the particles and gaseous CO₂ were sprayed predominantly in the axial direction whereas in Figure 4.4 the particles and gaseous CO₂ exited at a slower velocity and spread much more rapidly.

4.1.2 Effect due to Feed Tube Size. Three different diameters of feed tubes were used: 0.03 inch, 0.055 inch, and 0.068 inch. All feed tubes for size analysis were 12.1 inches in length. Each tube was married with the 0.33 inch ID simple shroud tube to isolate the effects of the feed tubes. Figure 4.5 shows the change in the Sauter mean diameter, D_{32} , for the three tubes with error bars at one standard deviation. It is apparent that an increase in the ID size of the feed tube decreases the mean particle size significantly, which is in agreement with the results of Greene. An effect of changing

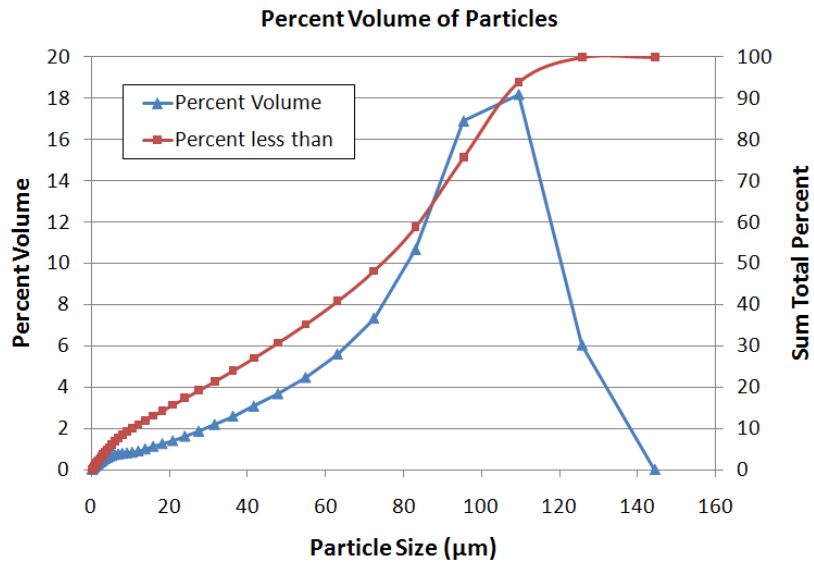


Figure 4.2: Percent of total volume particles of a given size make up.



Figure 4.3: Characteristic profile of particles exiting a simple shroud tube.



Figure 4.4: Characteristic profile of particles exiting a mixing shroud tube.

orifice size that was not measured but must be mentioned is the increase in mass flow rate of the CO₂ with increasing orifice size. A larger amount of liquid CO₂ flowed through the orifice and expanded, forming more particles, but also caused the velocity in the shroud to increase. Conversely, a small ID feed tube restricted the mass flow, thus slowing the flow through the shroud tube. As described above, a decrease in the speed through the shroud tube allowed for larger particles to grow, explaining the larger sizes seen with the 0.030 inch ID feed tube.

4.1.3 Effect due to Shroud Size. Two different diameters of shroud tube ID were used: 0.33 inch and 0.40 inch. Each of these tubes measured 10 inches in length. Figure 4.6 gives the mean D_{32} and standard deviation for these two configurations using the 0.068 inch feed tube. With a slightly larger diameter and a constant mass flow rate as governed by the orifice, the residence time of particles was higher for the larger shroud tube. This result is also consistent with those reported by Greene.

4.1.4 Effect due to Shroud Type. In addition to considering the effect of shroud diameter, two different types of shroud tube were studied: the simple straight tubes used above and the static mixing tube. The mixing tube had slightly thicker walls than the similar sized simple tube, which reduced the ID from 0.33 inch for the simple tube to 0.31 inch for the mixing tube. Also, the tube length was different; the simple tubes were 10 inches long whereas the mixing tubes were 14 inches long. Greene found that

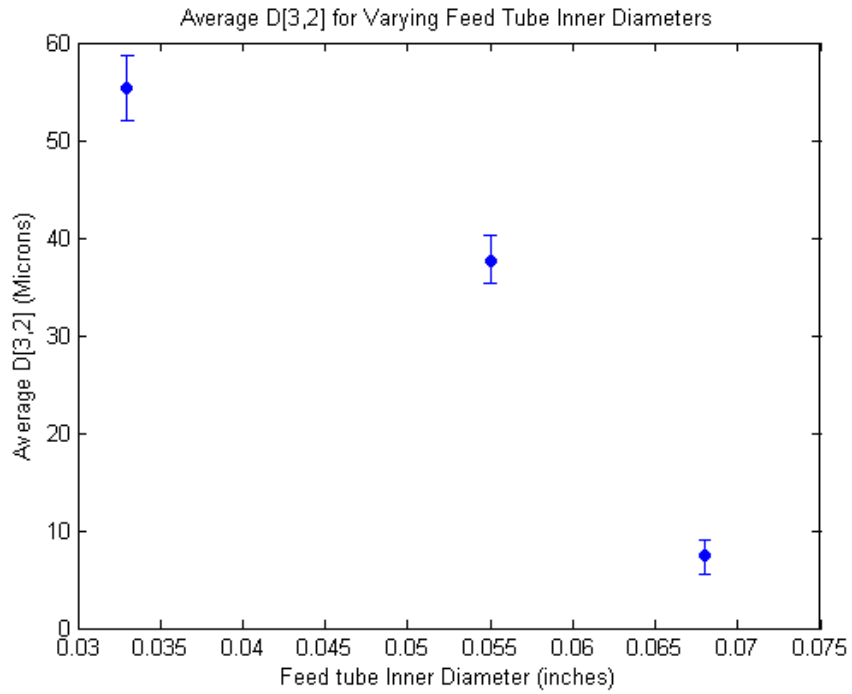


Figure 4.5: D_{32} for varying feed tube ID and a constant 0.33 inch ID shroud tube.

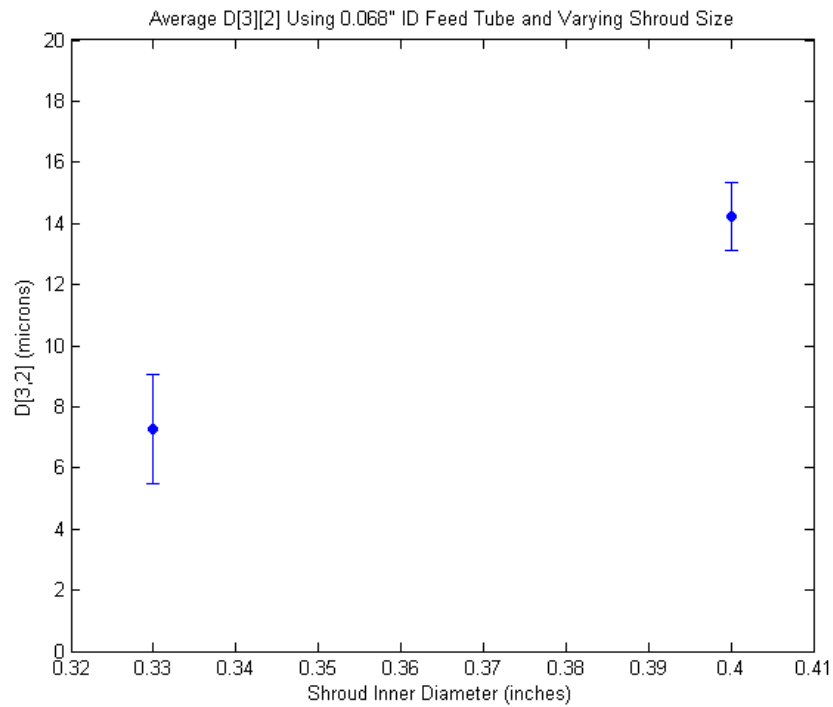


Figure 4.6: D_{32} for varying shroud tube size and constant 0.068 inch feed tube ID.

particle size plateaued at a length of approximately 10 inches and did not vary largely for a shroud tube 20 inches long so this difference was assumed to have little effect [10]. The main differences were two fold: the addition of the Kenics[®] static mixer as well as the heat exchanging fluid bath. With no fluid present, Figure 4.7 shows the mean D_{32} and standard deviation for the two types of tubes. These results suggest that the Kenics[®] mixer performs as expected in reducing the mean particle size, D_{32} , by a factor of approximately three even with no fluid bath present.

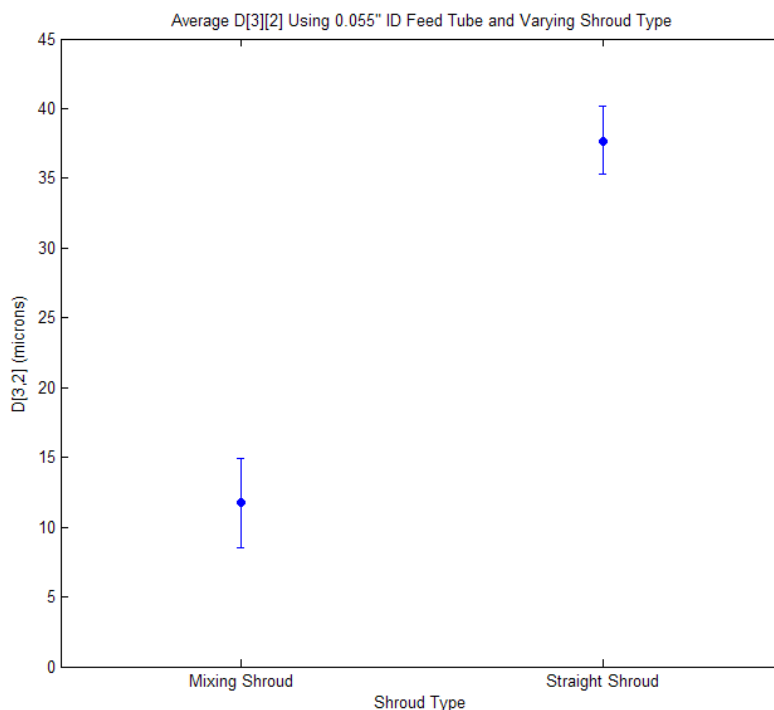


Figure 4.7: D_{32} for a simple versus mixing shroud tube type.

4.1.5 Effect due to Thermal Bath Temperature. Using deionized and distilled water, a refrigerated bath heated or cooled the water to a designated temperature and pumped the water through the heat exchanging shroud during data acquisition. Each data acquisition event lasted approximately one minute. In that time, the fluid bath temperature remained nearly constant, dropping less than 0.5°C . However, at the lower temperature measurements (20°C and 30°C), the water froze in the shroud housing such that the temperature of the heat exchanging fluid was not maintained in the shroud at

the desired setting. Figure 4.8 shows the results of the different bath temperatures using the 0.068 inch feed tube. It was evident that the small temperature range of 20°C - 50°C, as operated, produced no significant trends in particle size.

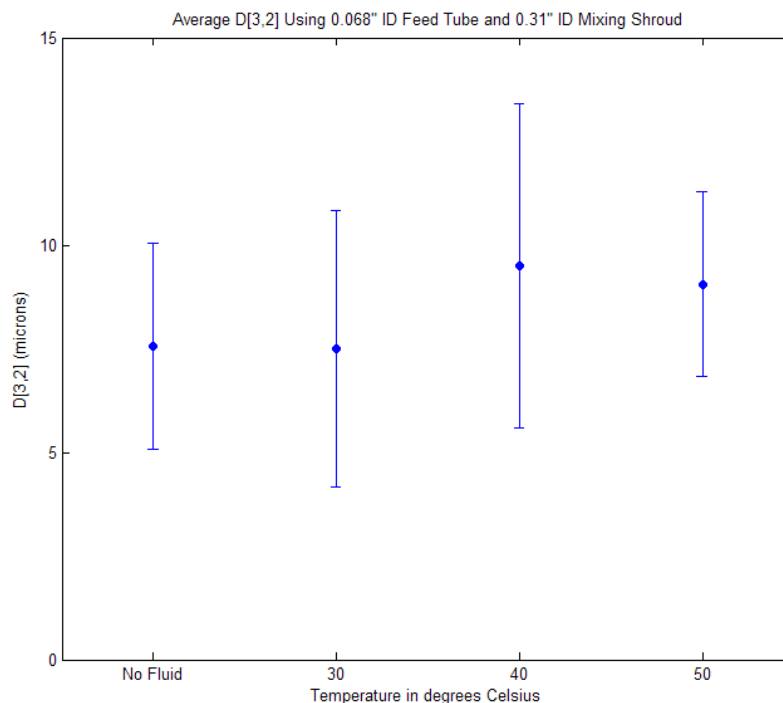


Figure 4.8: D_{32} for the mixing shroud, 0.068 inch ID feed tube and varying shroud bath temperature.

4.1.6 Sources of Error in Particle Size Analysis. As discussed at the beginning of this section, the Sauter mean diameter data presented is not the actual particle size, but rather an equivalent sized sphere that represents the particle size distribution. It is affected by the limitations of the particle size analyzer, being limited to the detection and calculation of a range of particles. The manufacturer suggested measurements less than about 2 μm are not reliable. As is evident in Figure 4.1, the Spraytec system measured the majority of particles in a range less than this, so there is uncertainty in this measure. Also, the experimental setup is an error source in that it is conducted in an environment that is exposed to ambient air, allowing humidity to affect the particle size. Water vapor can condense on particles, increasing their size during measurements. Conditioned dry air was provided in a coflow to reduce this effect, however, it may have still been present.

Finally, the flow of CO₂ was not steady. Clogging reduced the flow significantly at times, causing a decrease in particles. This issue was more prominent with the mixing tube, requiring more time to collect size measurements.

4.2 *AFIT Wind Tunnel Results*

The AFIT 6 inch by 6.5 inch supersonic blowdown tunnel was configured with a 10° ramp to observe the effects across an oblique shock. Temperature and pressure transducers installed on the tunnel were used to collect corresponding data for the tunnel flow conditions. This data was then used to calculate the speed of the flow and approximate the shock wave angle using equation 2.11 and isentropic flow theory. Using a set point of 40 psi, the approximate tunnel speed was calculated to be Mach 1.92 or 475 m/s. At this speed the 10° ramp would produce a 41° shock wave. These values were used for comparison to PIV data collected. Both temperature and pressure changed during the course of each tunnel operation so there was some variability in the speed and shock angle that was unavoidable. Figure 4.9 shows the typical change in conditions for each operation of the tunnel.

With the time delay between laser pulses set to 1 μ s and with 64 pixels corresponding to 2.43 mm, particles in the freestream typically traveled about 12 pixels. Most PIV systems are operated such that particles travel no more than about 0.25 times the length of the IR [3, 21]. Thus, the 64 by 64 pixel subregion size was expected to be reasonable, and a 32 by 32 subregion size was also explored.

4.2.1 Simple Shroud Tubes. The tunnel was configured with three dewars and three injection points, each using a 0.055 inch ID feed tube and 0.33 inch simple shroud tube. Laser power was set at 100 mJ per pulse and the camera aperture was set at f5.6. Unfortunately due to tunnel vibrations and the duration of operation at relatively stable conditions, only 10-20 image pairs were collected during each run. Several tunnel runs were combined to accumulate 174 image pairs. Using the process described in chapter three, the image pairs were correlated to produced vector statistics across the FOV. Figures 4.10 and 4.11 show the horizontal (U) velocity component using an IR size of 32

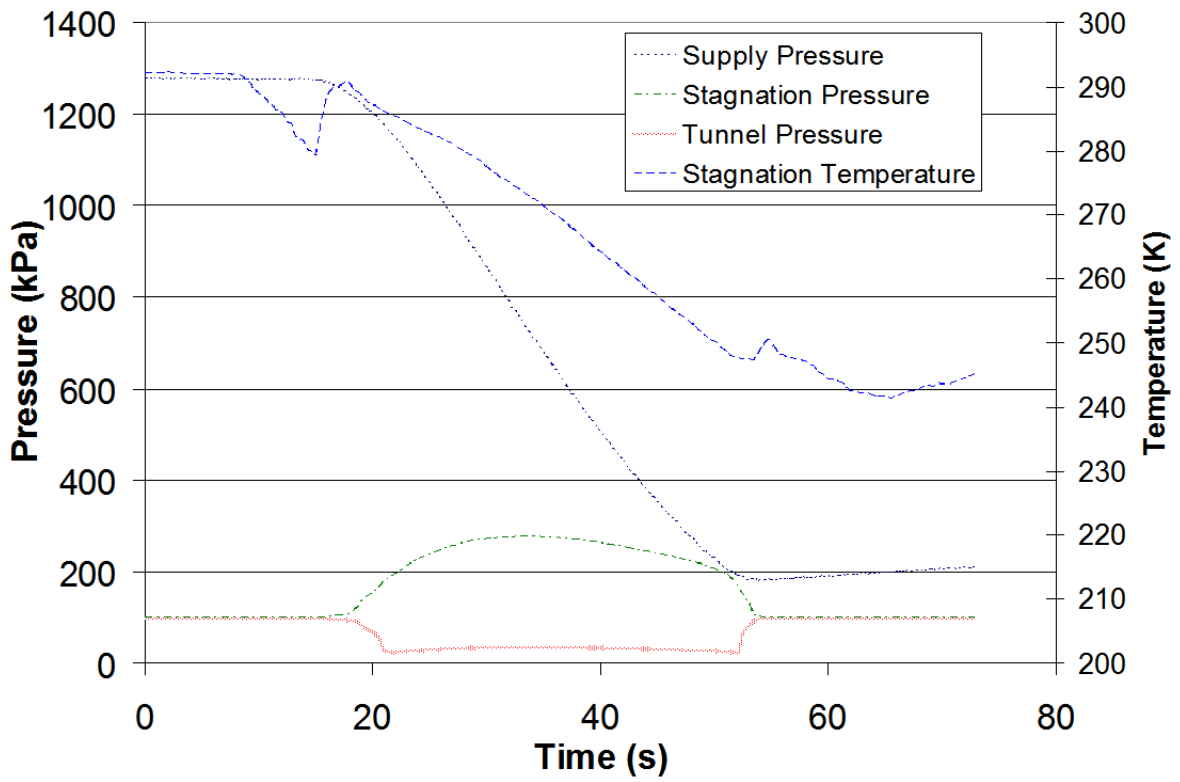


Figure 4.9: Typical transient conditions of AFIT blowdown wind tunnel operation.

by 32 pixels and 64 by 64 pixels, respectively. While the results are generally similar, the 64 by 64 IR size led to a smoother plot. The freestream velocity in both cases corresponded well with the calculated value of 475 m/s. The velocity downstream of the shock also correlated well with a calculated value of 439 m/s.

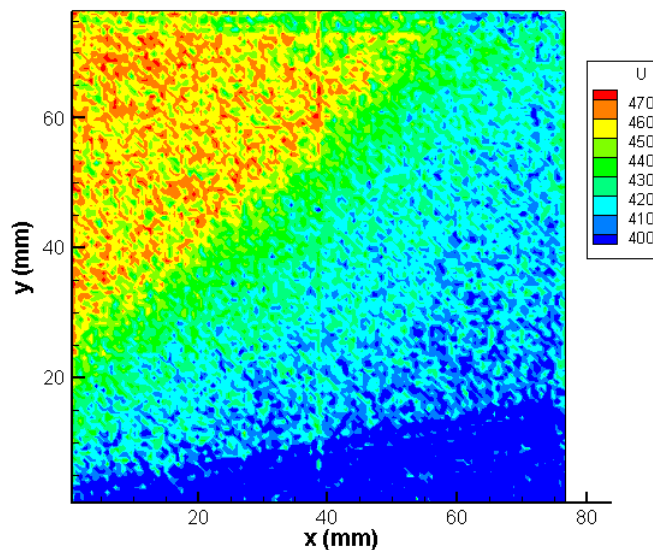


Figure 4.10: Horizontal velocity component using simple tubes and a 32 x 32 pixel IR.

The vertical velocity (V) perpendicular to the flow direction is shown for the two different IR sizes in Figures 4.12 and 4.13. In this case, the V component should be zero upstream of the shock but the PIV data apparent in both figures showed a slight positive vertical component of between 10-20 m/s. This equated to approximately 1-2 degrees of angularity in the flow upstream of the shock. Downstream of the oblique shock the calculated velocity from shock relations is 77 m/s while the PIV data suggested a value closer to 60 m/s. This may be related to the apparent flow angularity. By observing the schlieren images it was apparent that the flow upstream of the shockwave caused by the ramp was not entirely free of disturbances. It was possible that these disturbances led to the observed angularity of the flow. Figure 4.14 shows a weak oblique shock or Mach wave upstream of the shock caused by the ramp. Another factor that could account for this was that this vertical motion may have been a result of the minimum resolution of

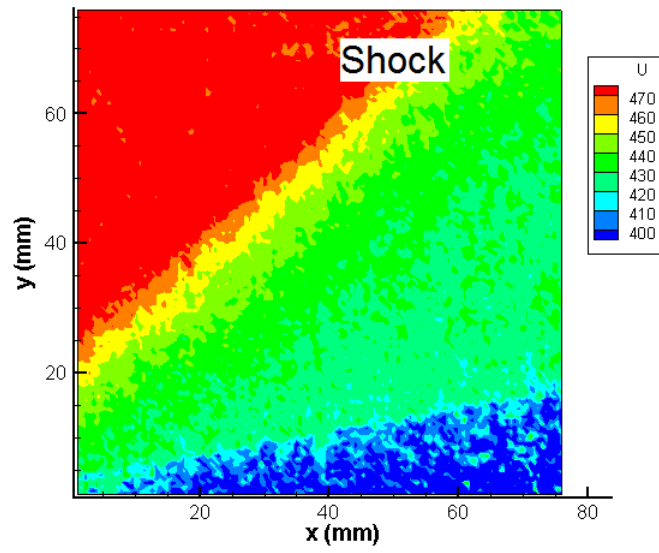


Figure 4.11: Horizontal velocity component using simple tubes and a 64 x 64 pixel IR.

the PIV processing. For the PIV FOV and the camera resolution, a motion of one pixel in an image pair equated to about 38 m/s.

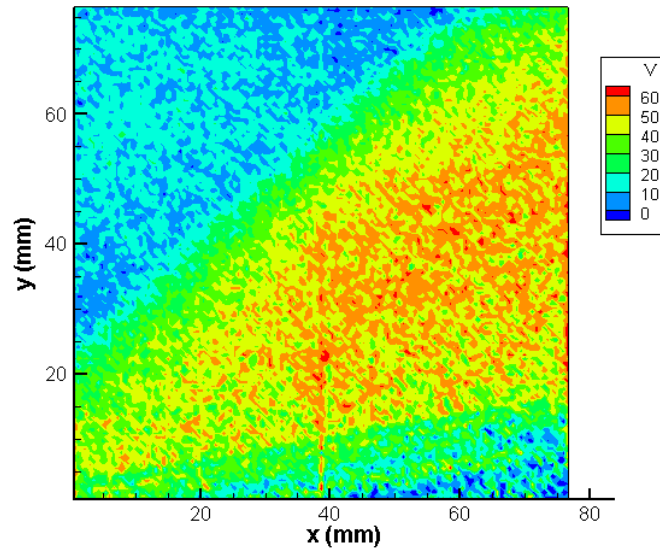


Figure 4.12: Vertical velocity component using simple tubes and a 32 x 32 pixel IR.

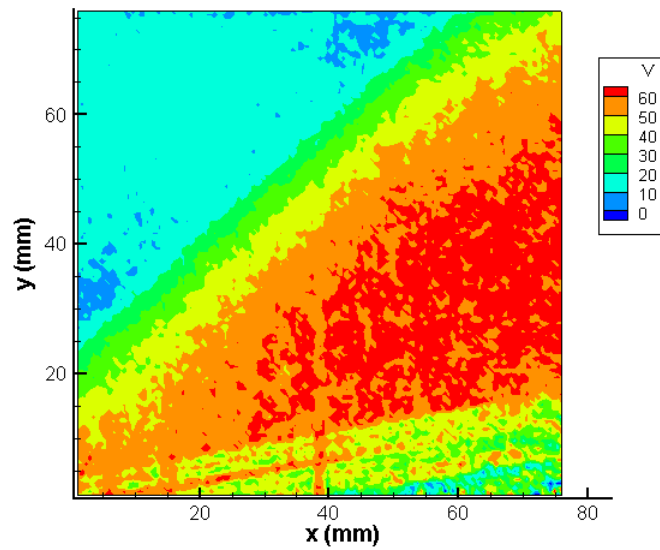


Figure 4.13: Vertical velocity component using simple tubes and a 64 x 64 pixel IR.

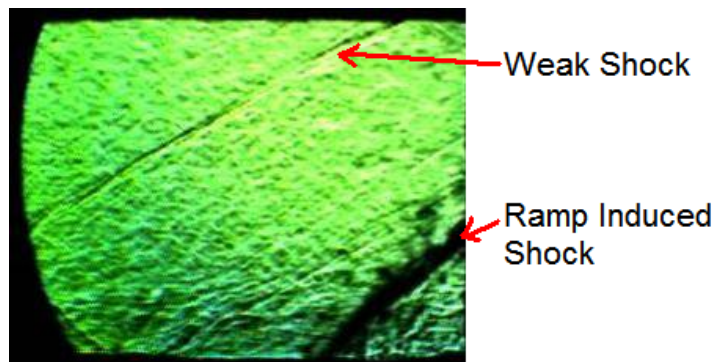


Figure 4.14: Schlieren image of flow upstream of PIV FOV showing a weak shock caused by tunnel roughness and a strong shock caused by the 10° ramp.

Having the horizontal and vertical velocity components allows the calculation of the velocity normal to the shock, V_{norm} , using equation 4.1 for each IR.

$$V_{norm} = U \sin \beta - V \cos \beta \quad (4.1)$$

Figures 4.15 and 4.16 show the results of the 32 and 64 pixel IR correlations respectively. The velocity tracked well with the calculated upstream and downstream velocities normal to the shock: 312 m/s and 230 m/s. By selecting vectors in a direction normal to the shock, the particle response could be compared with the theoretical response as determined using Melling's method described in chapter 2. In Figure 4.17 the response of the particles measured using both IR sizes is compared with the theoretical response of different size particles. The PIV data for both followed the trend of a 2.0 μm particle with a density of 1.18 g/cm³, and the smaller IR size did not show any advantage when determining this. Using the smaller IR size could have improved the resolution and altered the response curve, but in this case it did not.

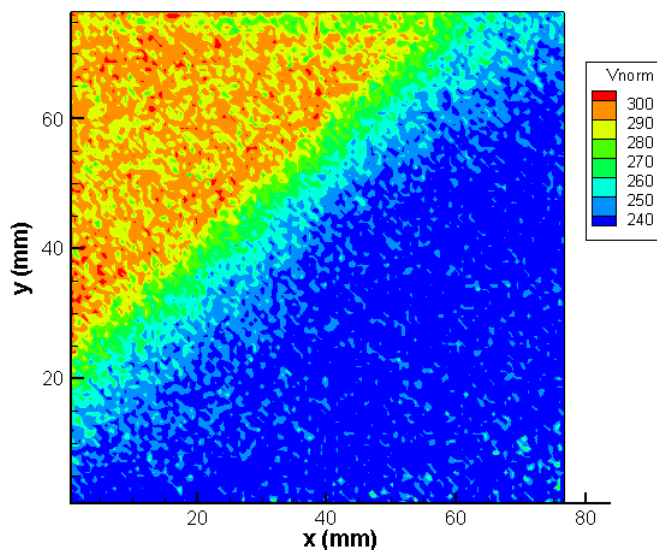


Figure 4.15: Velocity normal to the shock using simple tubes and a 32 x 32 pixel IR.

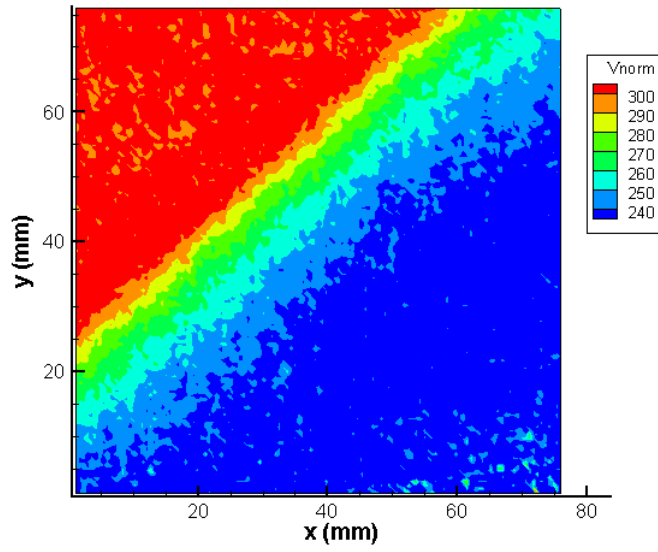


Figure 4.16: Velocity normal to the shock using simple tubes and a 64 x 64 pixel IR.

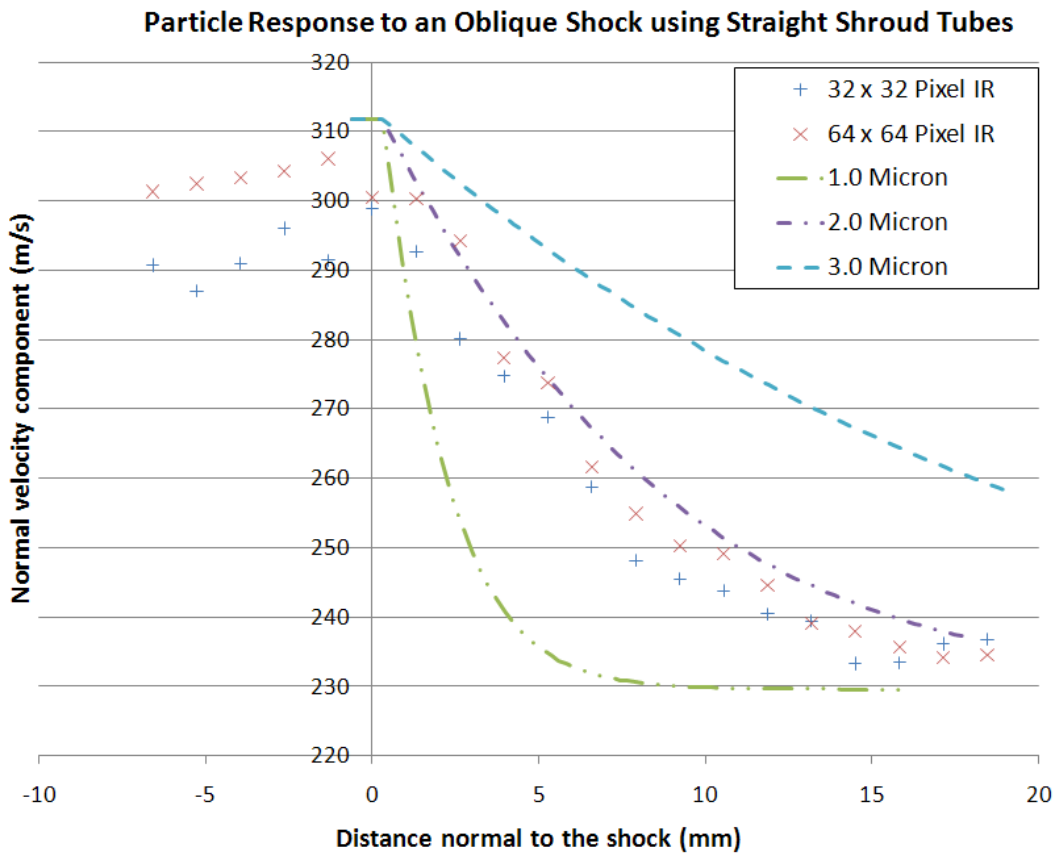


Figure 4.17: Particle response using two IR sizes compared to theoretical response for varying particle sizes.

4.2.2 Static Mixing Shroud Tubes. For the second set of tests the simple shroud tubes were replaced by three static mixing shroud tubes holding everything else constant. Initial runs of the tunnel in this configuration resulted with limited particle coverage in the image pairs collected. The hypothesis was that the particles were too small to be imaged successfully using the same camera and laser settings. Therefore, the camera f-stop was increased one stop to f4.0 and the laser power was increased to 200 mJ per pulse. These changes improved the visibility of particles in the images so all data collected on the mixing shroud tubes used these settings for the camera and laser. Overall, 150 image pairs were collected and used to produce the results below. Figures 4.18 and 4.19 show the horizontal (U) velocity component using an IR size of 32 by 32 pixels and 64 by 64 pixels, respectively. Again, the particles tracked the flow accurately far upstream and far downstream of the oblique shock wave. The same is evident in the vertical velocity component shown in Figures 4.20 and 4.21. The normal velocity is calculated in the same manner as above and is plotted in Figures 4.22 and 4.23. At the higher laser intensity and with an increased aperture, the particles generated by the static mixing tubes were able to track the freestream and downstream flow velocities accurately when compared to isentropic and shock relations. Across the shock, the particles lag the fluid velocity similar to a theoretical $2.0 \mu\text{m}$ particle, as can be seen in Figure 4.24. Surprisingly, even though laser power and aperture changes suggested smaller particles, the response characteristics indicated no significant change in the size of particles produced. For example, Figure 4.25 compares a 128 by 128 pixel region collected from a typical PIV image using the simple injectors to a similar region using the mixing injectors. The particles appear roughly the same size, however, the aperture for the mixing injectors was opened to f4.0 and the laser power was increased to capture this image. This suggested that there were either fewer particles or smaller particles with the mixing shroud tubes. Figure 4.26 shows, however, that the oblique shock wave was not entirely stationary due to turbulent structures in the boundary layer or possibly due to acoustic interactions in the tunnel. This can be seen with reference to the red horizontal reference line, which is drawn near the top of the oblique shock, indicated by the dark diagonal line. The nine sequential frames show that there is shock motion as

the dark diagonal line crosses above and below the stationary red reference line. Shock foot motion has been described by Beresh, et. al., albeit for a larger turning angle for a Mach 5 freestream [22]. Similar instability of a shock foot has been reported in the divergent section of nozzles as well [23]. Visual inspection of schlieren images suggest the shock motion is approximately 4 mm normal to the oblique shock wave. Because PIV results are averages over the collection time, the movement of the shock would be averaged out, resulting in a larger particle response distance based on PIV results.

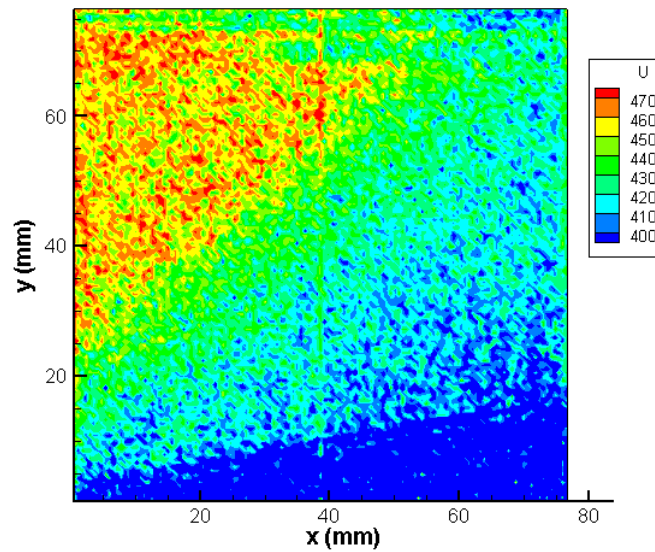


Figure 4.18: Horizontal velocity component using mixing tubes and a 32 x 32 pixel IR.

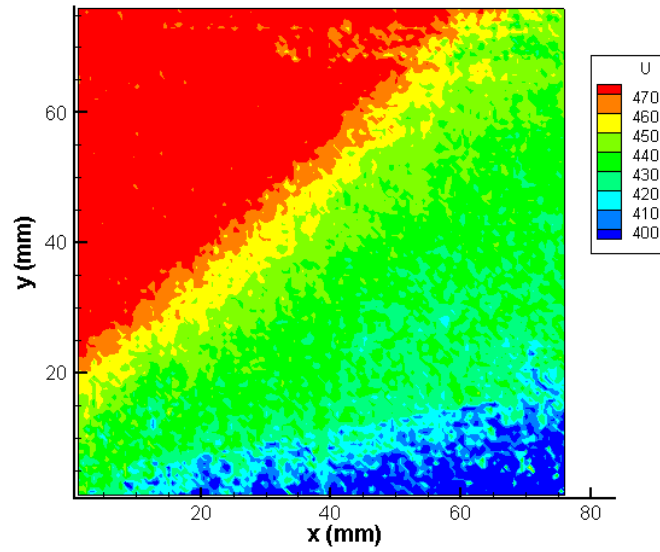


Figure 4.19: Horizontal velocity component using mixing tubes and a 64 x 64 pixel IR.

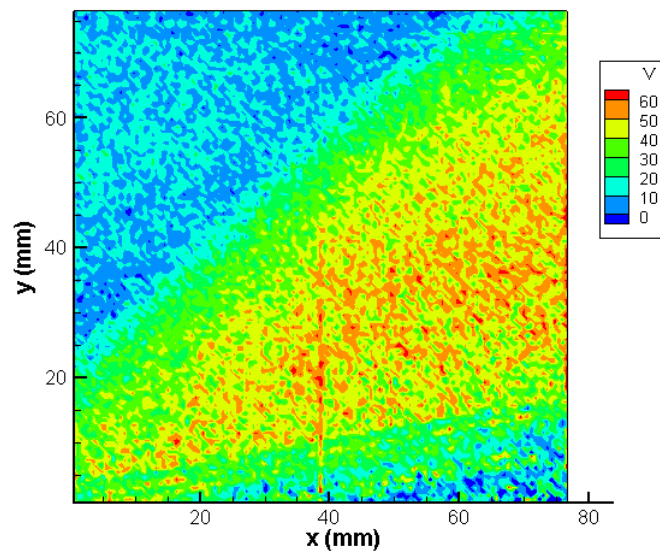


Figure 4.20: Vertical velocity component using mixing tubes and a 32 x 32 pixel IR.

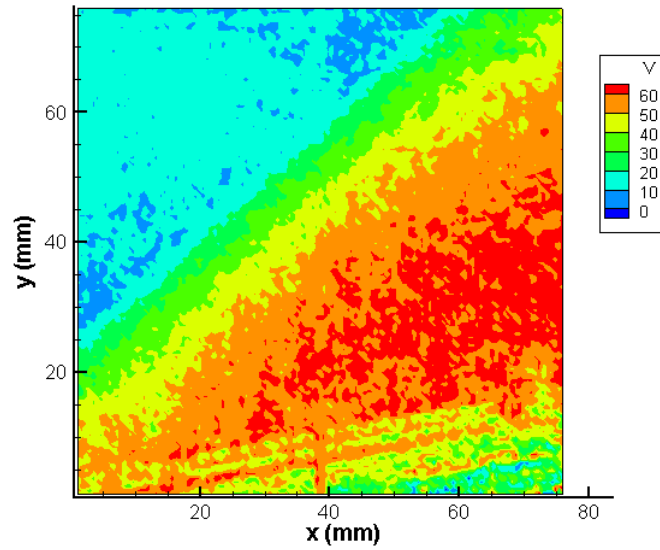


Figure 4.21: Vertical velocity component using mixing tubes and a 64 x 64 pixel IR.

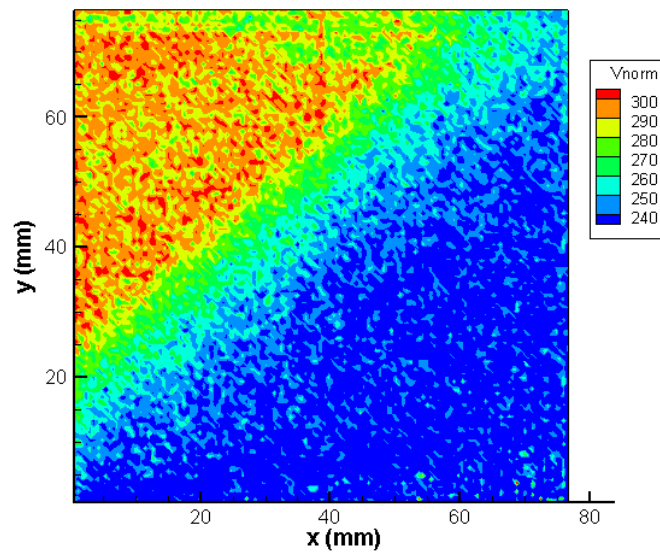


Figure 4.22: Velocity normal to the shock using mixing tubes and a 32 x 32 pixel IR.

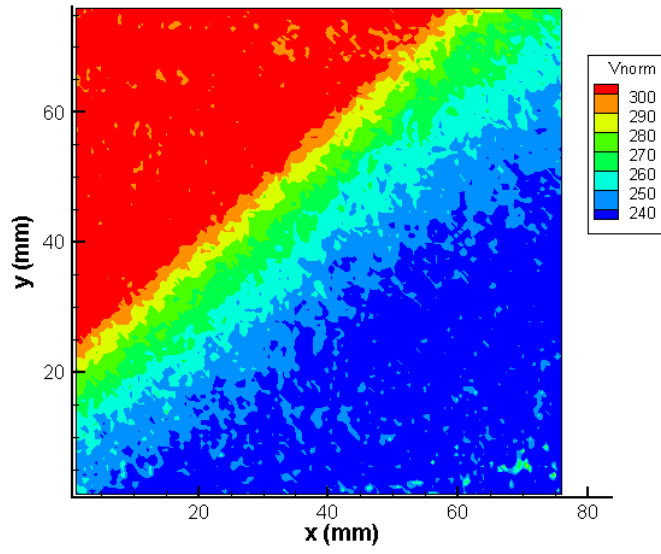


Figure 4.23: Velocity normal to the shock using mixing tubes and a 64 x 64 pixel IR.

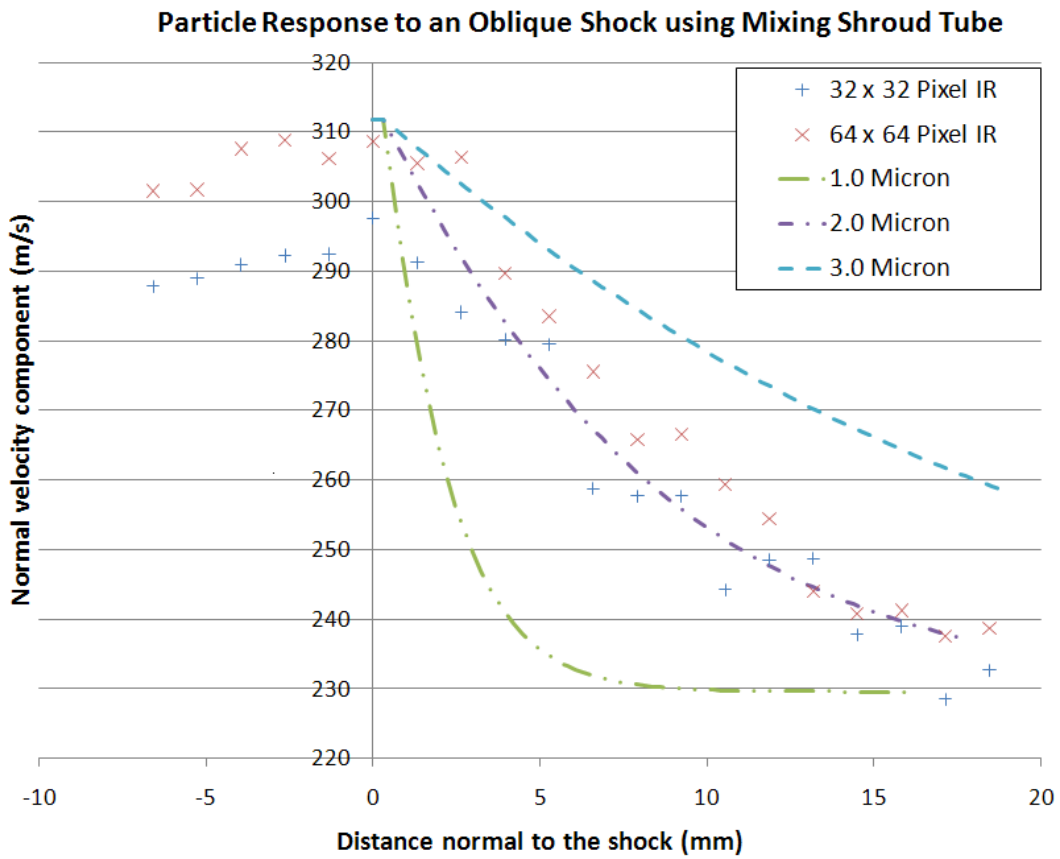


Figure 4.24: Particle response using two IR sizes compared to theoretical response for varying particle sizes

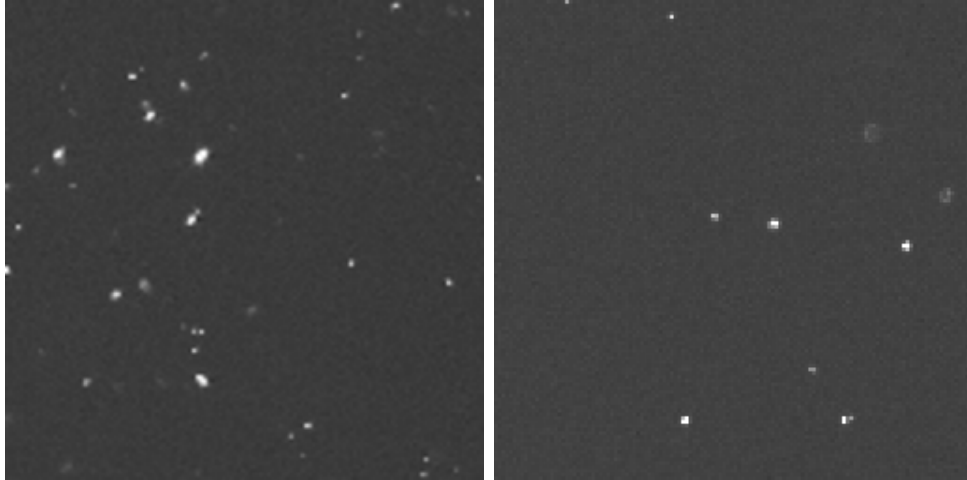


Figure 4.25: 128 by 128 pixel regions for simple injectors at f5.6 (left) and mixing injectors at f4.0 (right).

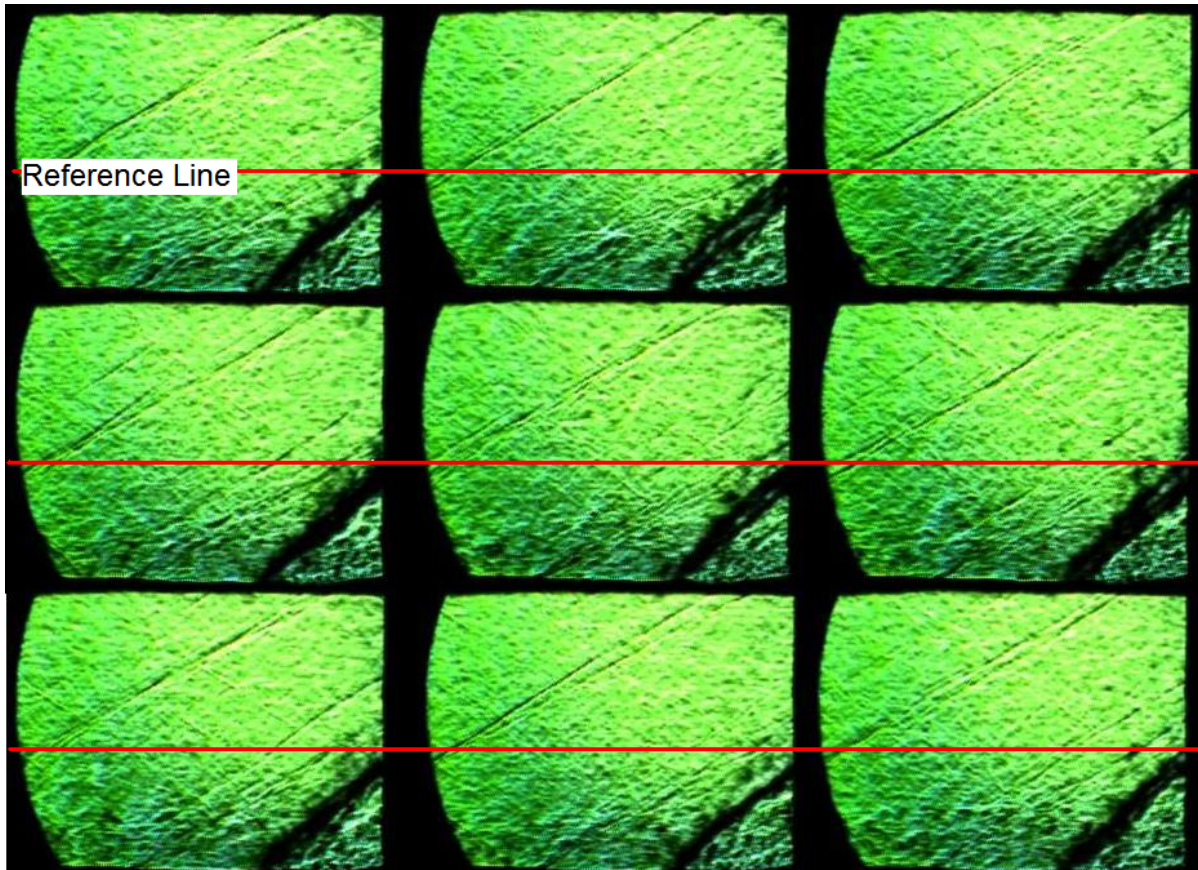


Figure 4.26: Nine sequential frames using a red reference line to indicate shock displacement over time.

Though 150 image pairs were collected and used for these calculations, many of the image pairs collected showed sparse particle coverage when using the mixing tubes. I believe this is the effect of CO₂ accumulation either in the line or in the mixing tube itself to the point where all flow was restricted. This clogging was observed when performing Malvern particle size analysis as well. For Malvern testing, most clogs did not seem to persist more than 10 seconds, but with the limited duration of PIV image collection in the tunnel, a clog in a single injector could reduce the particle count by one third for all the images collected on that run. If more than one line clogged, obviously the quantity of particles would be further reduced.

In both Figures 4.17 and 4.24, the measured velocity using the smaller IR was lower than that found using the larger IR. This suggests using the smaller IR biases the vectors produced towards zero. Use of the Gaussian filter may be the root cause. For the 1 μ s time delay between image frames, the pixel displacement is approximately 12 pixels. For a 32 pixel IR, the displacement is one third the length of the IR and the Dantec software recommends less than this when using the Gaussian filter [14].

4.2.3 Sources of Error in AFIT Wind Tunnel Testing. Though some discussion has been covered above on the potential reasons for the disagreements between PIV data and the expected velocities based on tunnel instrumentation, several other areas can affect the accuracy of these comparisons. First, the expected velocities were based on tunnel instrumentation that lacked recent, valid calibration. Both pressure and temperature transducers were used in the tunnel to provide the necessary information to compute expected conditions upstream of the shock, but the only calibration equipment available at the time of testing required calibration itself. These transducers had been used recently by Freeborn and Greene for their experiments, and the calibration performed during this experimentation agreed well with their data, but it is still a source of uncertainty [9, 11].

Next, the modifications to the tunnel test section prior to testing may have introduced a weak shock as seen in Figure 4.14. However, this apparent shock may have been isolated to one of the sides of the tunnel rather than across the entire area. The

schlieren system used was not focused, rather, captured all density gradients between the two mirrors and collapsed them onto a two dimensional image. If the shock was located directly upstream of the focal plane of the PIV system, the disagreement between the velocities would be increased.

Finally, the PIV system may introduce errors that aren't known. The velocity results are based on a user-defined calibration correlating a length scale to a pixel scale. The velocity calculations require sub-pixel analysis to resolve velocity differences less than about 38 m/s in this setup, which is the equivalent speed of a one-pixel displacement for the 1 μ s time delay. If the calibration is slightly off, velocity results could be biased.

4.3 AFRL Wind Tunnel Results

The TGF was used with a LaVision PIV system and multiple injection ports and types to demonstrate the usability of this seeding method. The TGF uses interchangeable nozzle blocks to produce supersonic flow, but for the testing performed, only the subsonic nozzle was used, allowing speeds up to approximately $M = 0.8$ at variable pressures. Figure 3.11 shows the subsonic conditions achievable. The test conditions used for testing are shown in Table 3.2.

4.3.1 Cross Plane. Figures 3.12 and 3.13 show the initial setup using two injection points in the stilling chamber through the wall and a third injection point just upstream of the test section. Table 4.1 lists the position and configuration of each injector. To improve the chances of seeing particles, each injection point used a different combination of tubes, introducing two that had not been used for data collection in the AFIT tunnel: a curved 0.4 inch ID shroud tube and a 0.17 inch ID shroud tube. The third injector was identical to that used in the AFIT wind tunnel: 0.055 inch ID feed tube and 0.33 inch ID shroud tube. This initial test was used to determine whether or not seeding was present through the test section, and if so, where. The increased distance from the injector port to the test section (approximately 20 feet) and the lower tunnel speed meant that the particles had to persist much longer in the TGF than in the smaller AFIT wind tunnels. Therefore, the PIV system projected the laser sheet such

that the flow direction was normal to the laser plane. Two cameras were used to image the left and right sides of the tunnel using Scheimpflug mounts to maintain focus from an off-axis direction. This arrangement is shown in Figure 4.27. The images collected were not processed for PIV, rather they were used to determine whether particles persisted and where they were present.

Table 4.1: Injector configurations for TGF testing.

Location	Feed Tube ID (inches)	Shroud Tube ID (inches)
Stagnation Chamber	0.068	0.40
Stagnation Chamber	0.055	0.33
Test Section	0.068	0.17

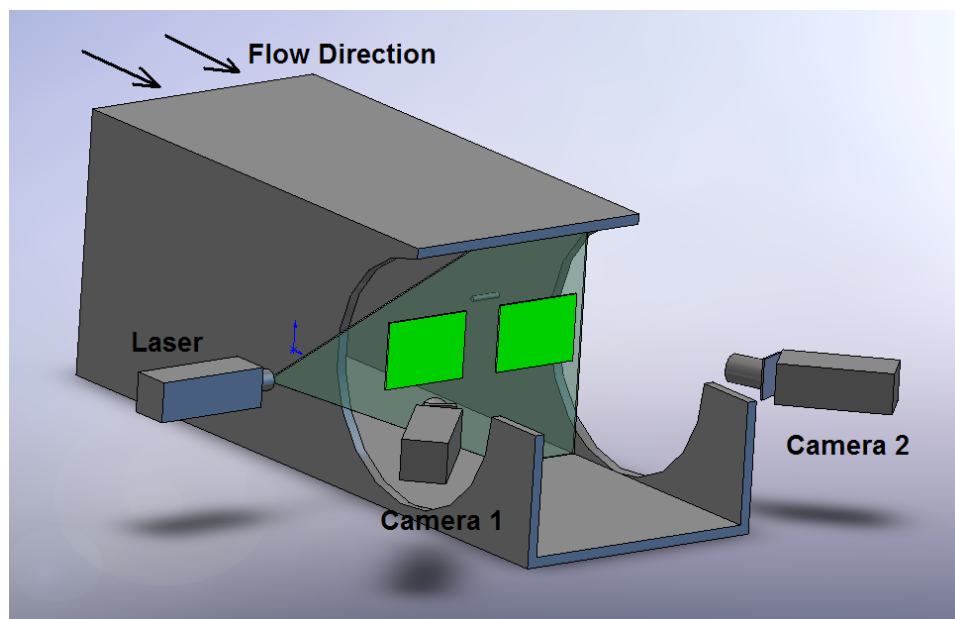


Figure 4.27: Cross-plane PIV setup at the TGF with approximate fields of view for each camera.

At the conditions in Table 3.2, each injector was tested individually to observe particles. The goal was to see particles injected from the stilling chamber because for actual testing, there would be little flow disturbances from the shroud tube seen in the test section whereas the injector just upstream of the test section would cause a momentum deficit in its wake, possibly disturbing the flow over the model being studied. If no particles were seen, however, this injector near the test section windows would be easily observed by eye to check for problems. Particles were observed from two of the

three injectors, though the larger, curved shroud tube provided very promising results. This injector used a shorter, 3 inch feed tube with a 0.068 inch ID. Figure 4.28 is a typical image of the right side of the test section looking upstream at $M = 0.8$ and $P = 250$ psf using this injector. The third, smaller stagnation chamber injector did not produce particles that persisted through the test section. Similar results were observed at all speed and pressure test points.

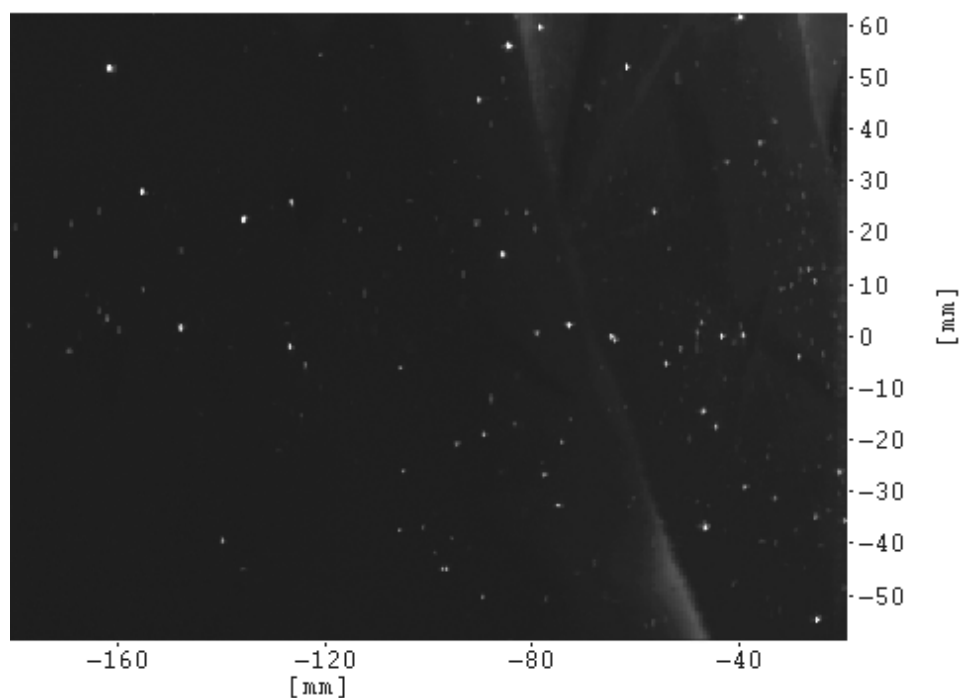


Figure 4.28: Image of seeding from curved 0.4 inch ID shroud at $M=0.8$, $P=250$ psf.

The second tube injecting into the stilling chamber was a simple tube with a 0.33 inch ID and 0.055 inch ID feed tube, identical to that used in the AFIT tunnel. Few, if any particles were observed in the test section with this injection configuration. A typical image of the particles from this injector is seen in Figure 4.29. This image was taken with the tunnel at $M = 0.8$ and $P = 250$ psf, which was the highest speed and lowest pressure settings used. A higher speed decreases the time between injection and passage through the test section for individual particles, and a lower pressure increases the expansion ratio from the liquid CO_2 , thus this condition is the most favorable for particle persistence through the test section. Since few particles were visible from this

injector at this tunnel condition, data was not collected with this injector configuration for the remaining test conditions.

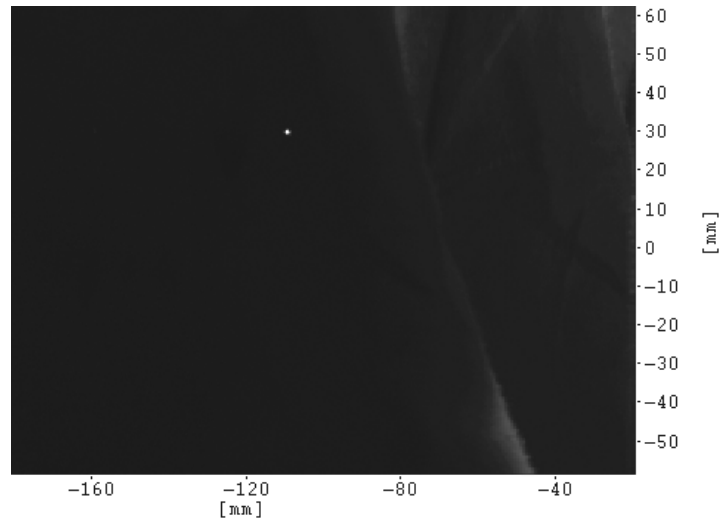


Figure 4.29: Image of seeding from simple 0.33 inch ID shroud at $M=0.8$, $P=250$ psf showing lack of particles.

The third injector was installed 13 inches upstream of the laser sheet and projected 4 inches into the tunnel from the test section wall. It used a 0.17 inch ID shroud tube and a 0.055 inch feed tube. Because of its close proximity to the laser sheet and the viewing windows, the particles produced were easily observed by both the PIV system and by eye. However, the close proximity also meant that the particles did not spread evenly across the FOV of either camera, so discrete particles were hard to discern because of the large concentration over a very small region. Figure 4.30 is a typical image of the particles produced by the test section injector and Figure 4.31 overlays this image on the approximate field of view of the camera. The bloom is indicative of a jet in a crossflow profile where the larger particles are ejected further into the stream and smaller particles respond more quickly to the flow change. Since the main goal was to observe particles injected into the stilling chamber and the curved injector proved effective in achieving this, the test section injector and the other stilling chamber injector were not used for the remaining test conditions.

4.3.2 Streamwise Plane. With successful particle generation using the large ID feed tube and the large ID, curved shroud tube, the TGF was reconfigured with two

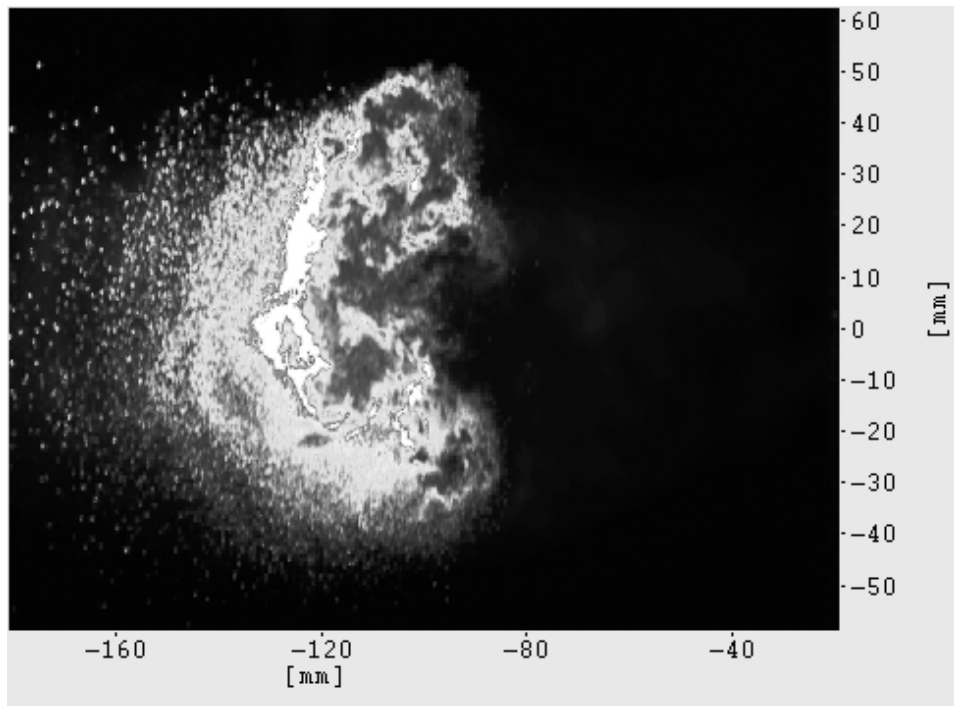


Figure 4.30: Image of seeding from simple 0.17 inch ID shroud at $M=0.8$, $P=250$ psf showing typical jet in a crossflow profile.

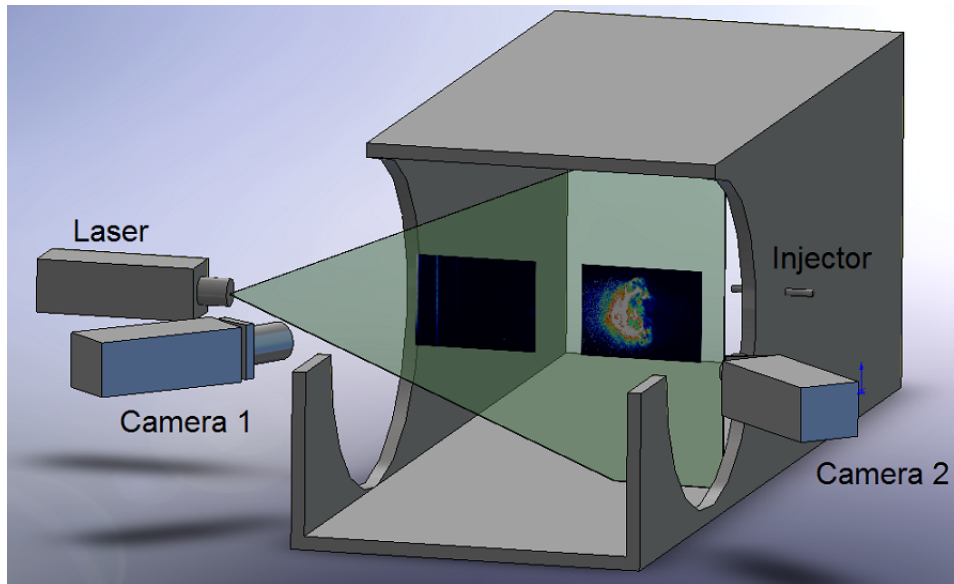


Figure 4.31: Approximate PIV image location within the test section.

more injectors identical to the first, all injecting into the stilling chamber. The PIV system was reconfigured such that the laser sheet was parallel with the flow direction, but at an angle from the tunnel walls. This was necessary to allow a perpendicular angle between the camera and laser sheet. This setup is shown in Figure 4.32. The tunnel was run at the same conditions as shown in Table 3.2 with all three injectors flowing at each test point. One hundred image pairs were collected at a frequency of 10 Hz for each condition. Figure 4.33 is a sample image collected in this configuration. Several reflections are present in the left side of the image, thus this data was removed from the figures showing the results for all the conditions. The red box in the image indicates the area that PIV figures are drawn from. Also visible in this image is the variation in particle size seen in the FOV. Many large particles were present in the images. Figure 4.34 projects the PIV results presented on the approximate location in the wind tunnel test section. To align with standard convention, the data has been rotated so that the flow is from left to right in each vector map.

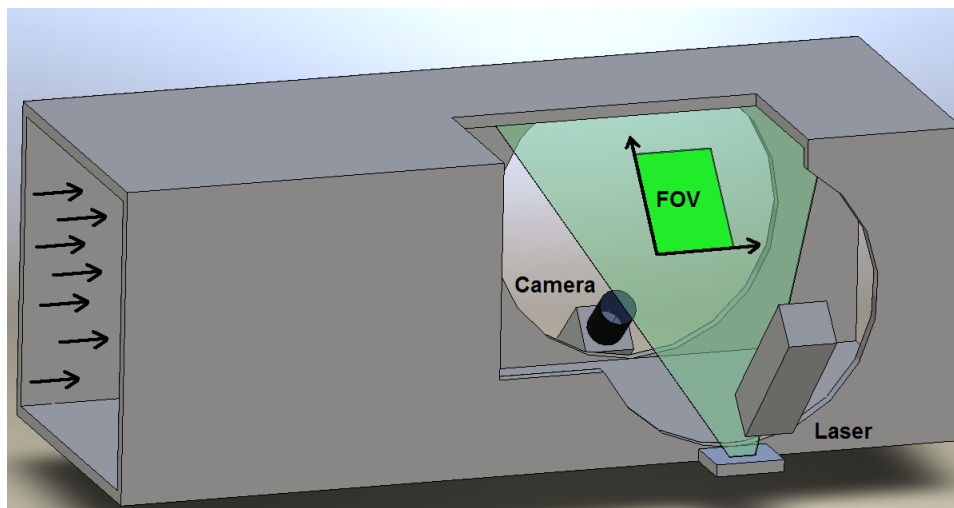


Figure 4.32: Setup for PIV data collection in the TGF.

Figures 4.35 and 4.36 are comparisons of the three different test condition speeds at approximately the same stagnation pressure. In these and the remaining figures, the images have been rotated so that the flow direction is left to right as indicated by the vector maps. Additionally, the full frame of the camera FOV has been cropped to remove erroneous data that was caused by strong reflections in the images. The TGF

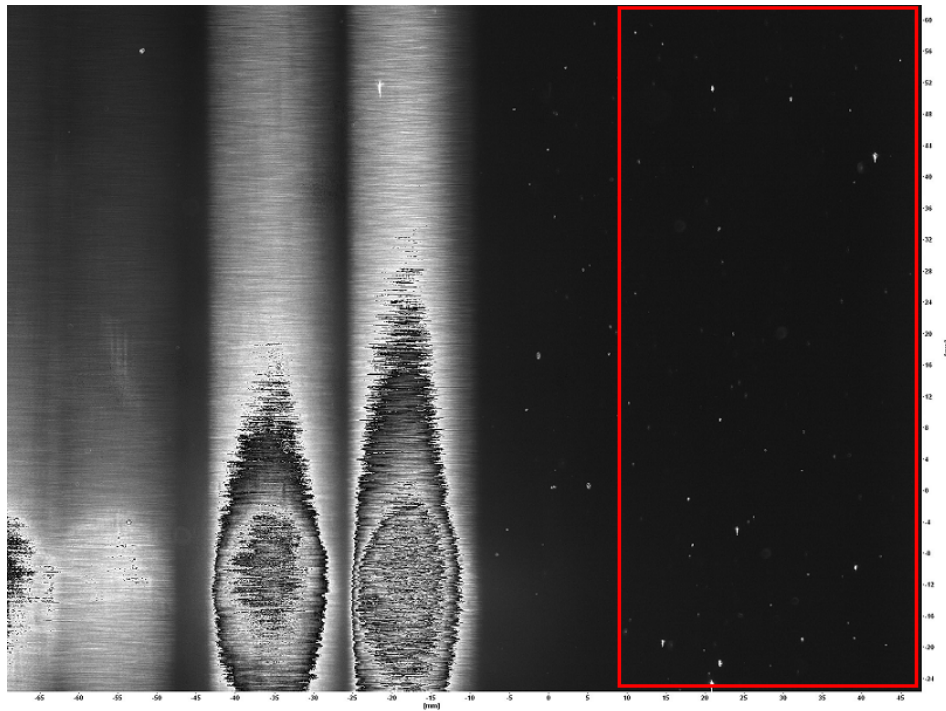


Figure 4.33: Sample PIV image collected in the TGF. The red box indicates area processed for PIV.

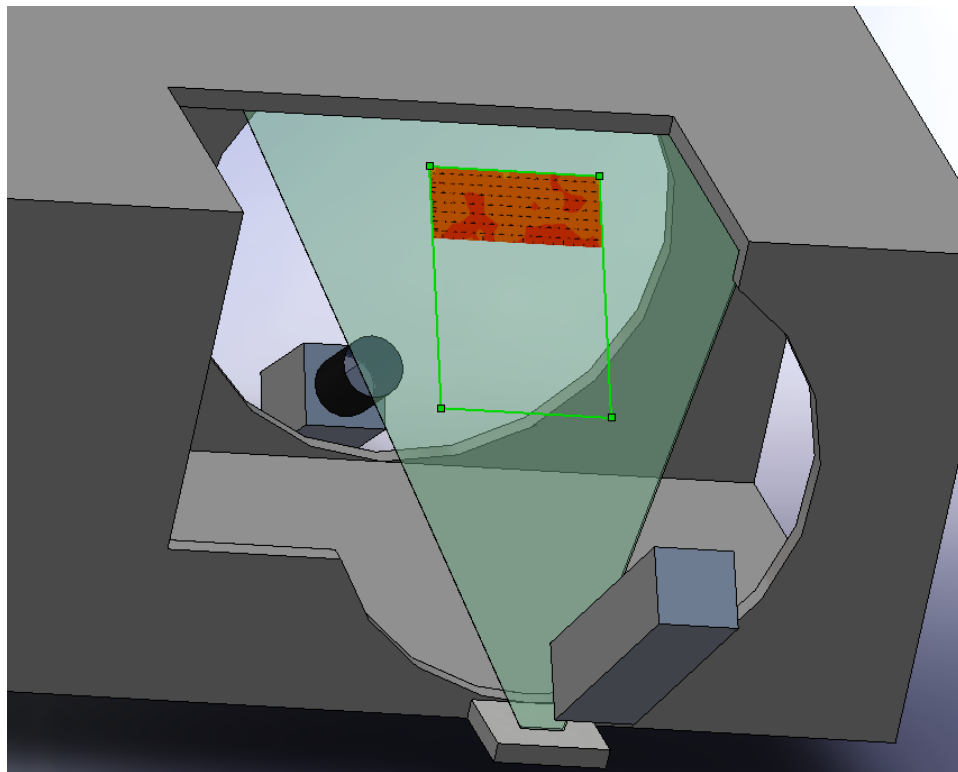


Figure 4.34: Sample PIV vector map overlaid on the approximate field of view for the PIV arrangement at the TGF.

operated at a stagnation temperature between 293 K and 300 K so the actual velocity using equation 2.8 can be calculated. Based on tunnel data collected, the approximate velocities at Mach 0.3, 0.5 and 0.8 were 100 m/s, 170 m/s and 260 m/s, respectively.

Figure 4.37 is the streamwise velocity component at Mach 0.89 and 255 psf. Figure 4.38 is at Mach 0.79 and 501 psf. At the lower pressure there were larger variations in speed than at the higher pressure condition where the field is much more uniform. This was likely due to a variation in tunnel conditions during data collection that was not known at the time. It was noted following data collection that the TGF conditions were not stable and the Mach number varied, which could account for the speed variation in the data. Each vector was the average of only about 10 - 20 % of the image pairs so some vectors could be the result from the beginning of the data collection whereas its neighboring vectors may have been the result of data from the end of the data collection. For the same reason, the turbulence, as indicated by the RMS fluctuations normalized by the streamwise velocity, was higher than expected, as seen in Figures 4.39, 4.40, 4.41 and 4.42.

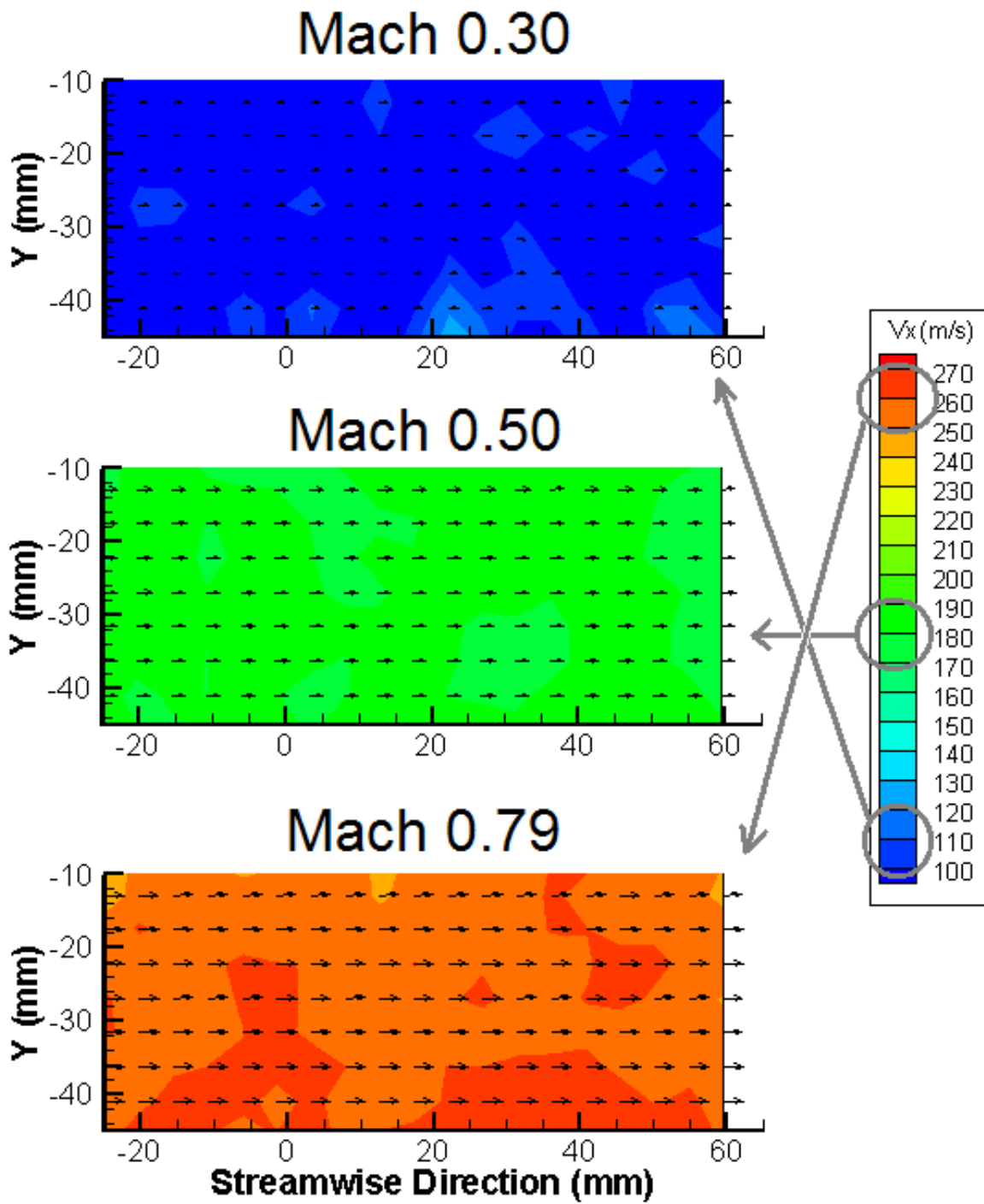


Figure 4.35: Streamwise velocity maps at $P_0 = 500$ psf and varying speeds.

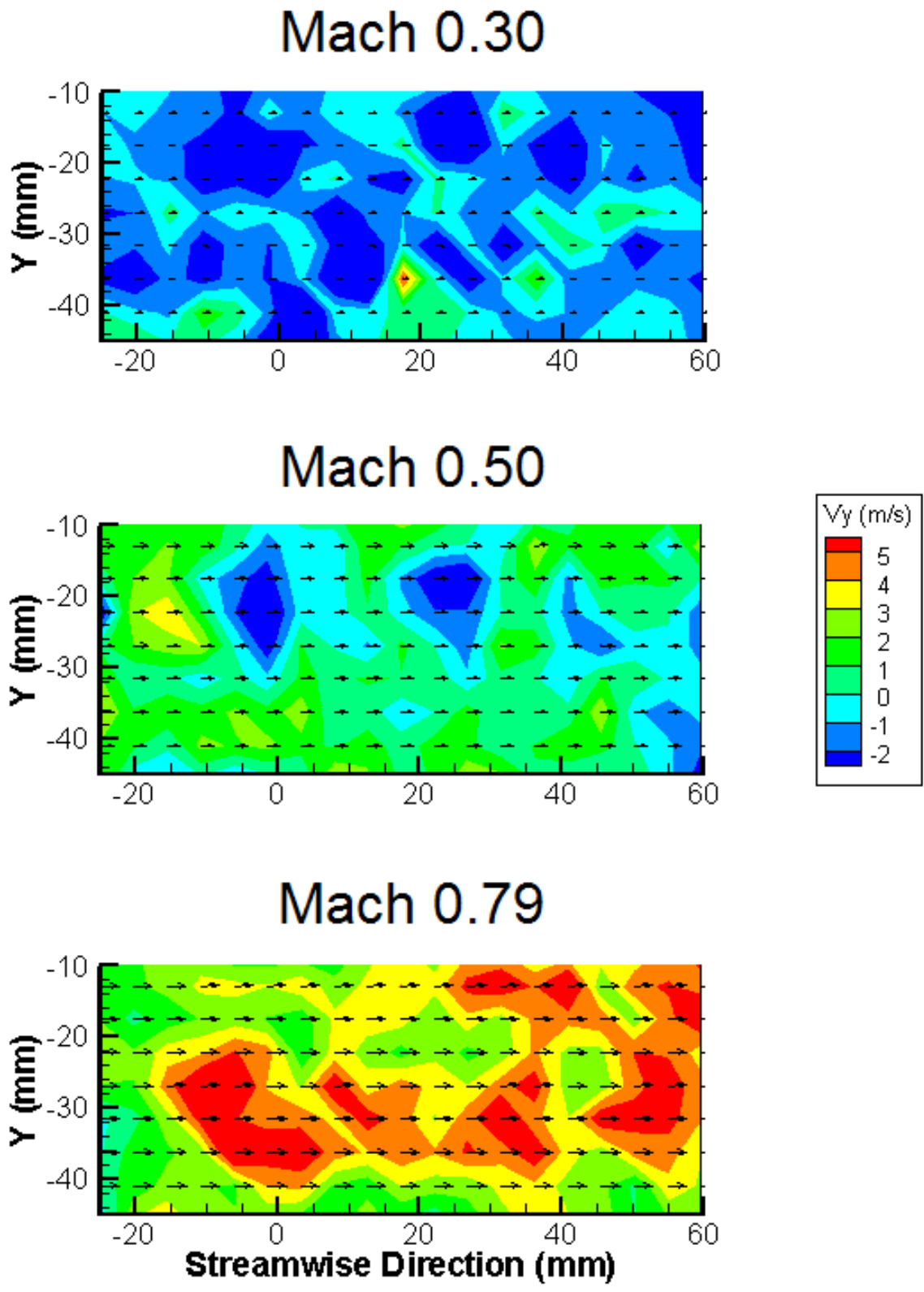


Figure 4.36: Vertical velocity maps at $P_0 = 500$ psf and varying speeds.

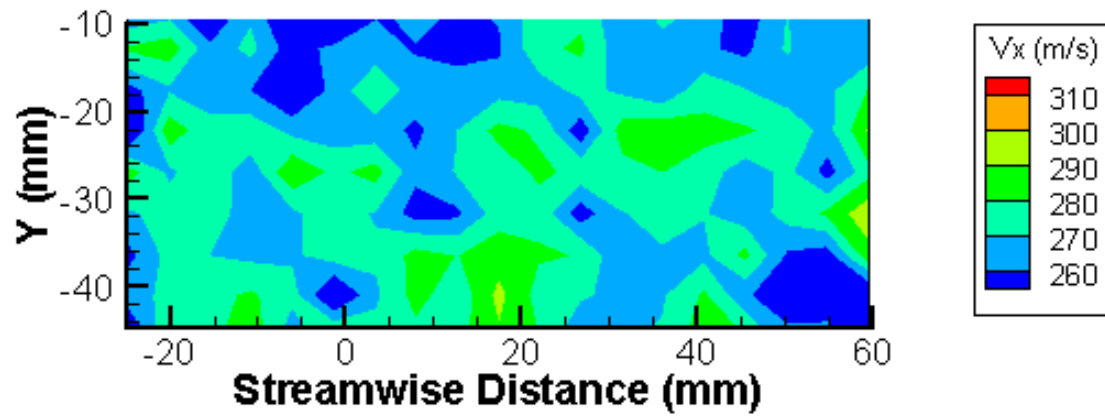


Figure 4.37: Streamwise velocity profile at $M = 0.89$, $P_0 = 255$ psf, and $T_0 = 294$ K.

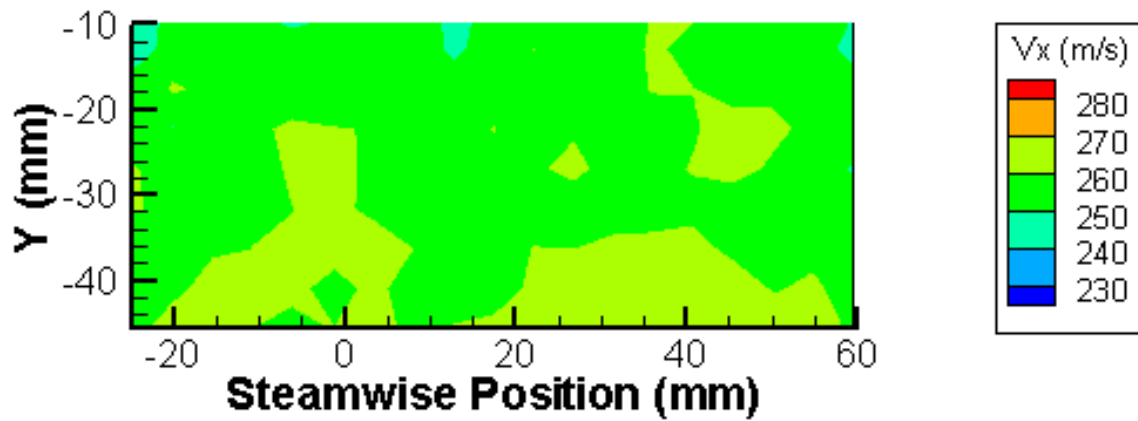


Figure 4.38: Streamwise velocity profile at $M = 0.79$, $P_0 = 501$ psf, and $T_0 = 296$ K.

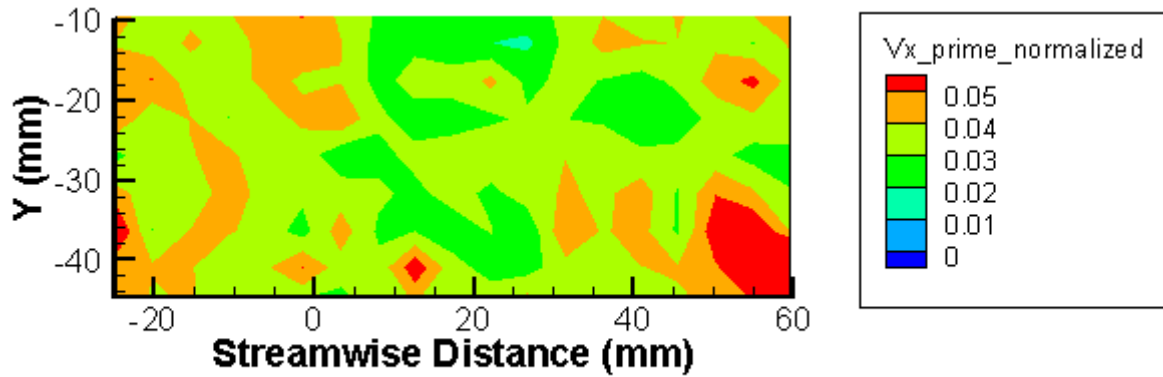


Figure 4.39: Streamwise turbulence profile at $M = 0.89$, $P_0 = 255$ psf, and $T_0 = 294$ K normalized by the calculated freestream velocity, 286 m/s.

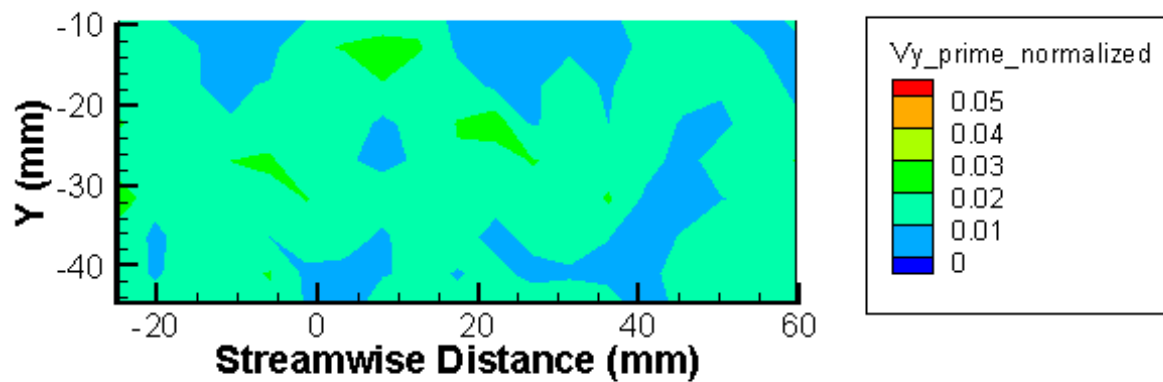


Figure 4.40: Vertical velocity turbulence profile at $M = 0.89$, $P_0 = 255$ psf, and $T_0 = 294$ K normalized by the calculated freestream velocity, 286 m/s.

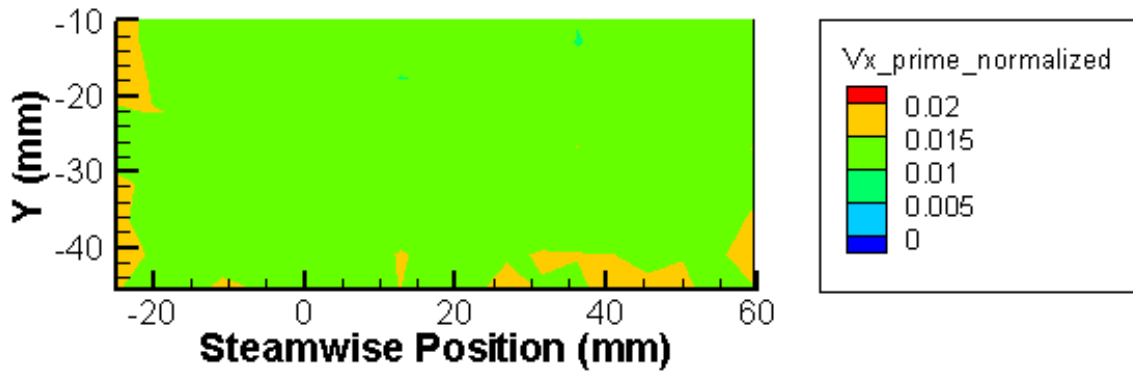


Figure 4.41: Streamwise velocity turbulence profile at $M = 0.79$, $P_0 = 501$ psf, and $T_0 = 296$ K normalized by the calculated freestream velocity, 257 m/s.

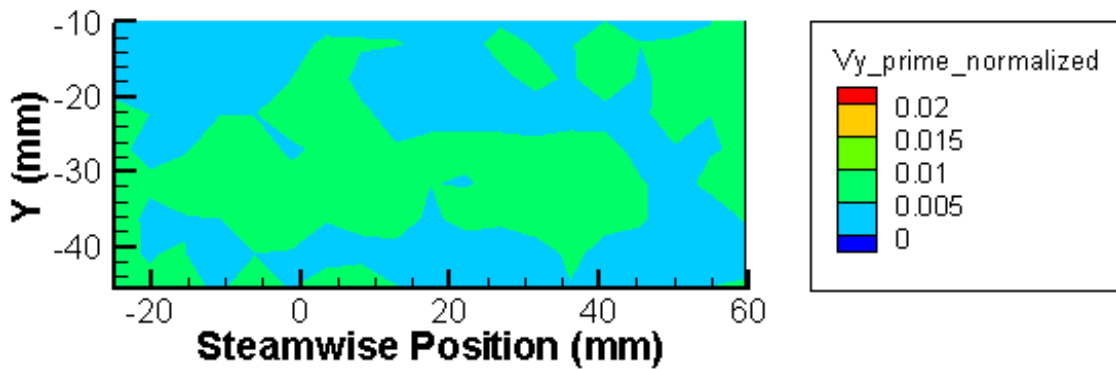


Figure 4.42: Vertical velocity turbulence profile at $M = 0.79$, $P_0 = 501$ psf, and $T_0 = 296$ K normalized by the calculated freestream velocity, 257 m/s.

The turbulence figures, however, are the result of only 100 image pairs. Therefore, the turbulence results are presented as a rough estimate rather than a statistically valid result. If each valid vector for a test condition is assumed to be an independent measure of the freestream velocity, however, then they can be combined into a single ensemble of several thousand data points versus 100. Table 4.2 presents these results, providing the number of vectors used at each test condition, the average horizontal and vertical velocity components, and the normalized fluctuations. The Mach 0.3, P =516 psf and the Mach 0.8, P=255 psf cases have the largest fluctuations, but these are explained above for the high speed case and in later paragraphs for the lower speed case.

Table 4.2: Turbulence estimates based on all valid vectors at each test condition.

Mach	P (psf)	# Vectors	U_{avg}	$ V _{avg}$	U'/U	V'/U
0.30	517	2931	94.0	4.5	0.0186	0.0011
0.30	1007	14877	107.4	3.3	0.0080	0.0003
0.30	1506	14955	109.9	3.2	0.0080	0.0003
0.5	500	12630	181.7	7.4	0.0086	0.0004
0.5	1000	15044	175.3	3.7	0.0080	0.0002
0.5	1500	15005	173.4	3.0	0.0080	0.0002
0.89	255	2282	272.7	11.1	0.0203	0.0009
0.79	501	14107	258.6	8.6	0.0082	0.0003

Figures 4.43, 4.44 and 4.45 are the streamwise velocity maps for a nominal Mach 0.5 velocity and pressures of 500, 1000 and 1500 psf. The actual tunnel data for these three events was not available, so true velocity comparisons could not be made. The calculated velocity at Mach 0.5 is approximately 170 m/s but at the lower pressures, PIV data indicates an approximately 8% higher velocity than this. However, if the actual speed was higher during the lower pressure runs because the TGF was set to a higher velocity, then the PIV data may be accurate. Vertical velocity remains low and freestream turbulence is less than 2% for each case, as shown in Figures 4.46, 4.48, 4.50, 4.47, 4.49 and 4.51.

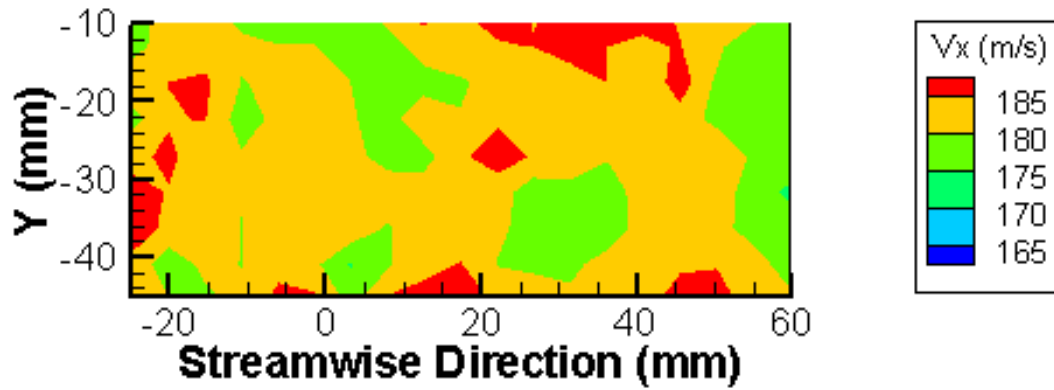


Figure 4.43: Streamwise velocity profile at $M = 0.5$, $P_0 = 500$ psf, and $T_0 = 294$ K.

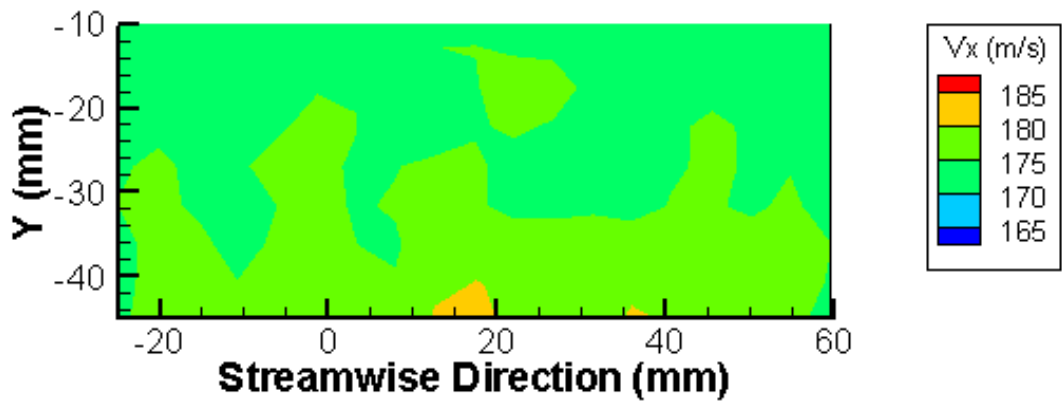


Figure 4.44: Streamwise velocity profile at $M = 0.5$, $P_0 = 1000$ psf, and $T_0 = 294$ K.

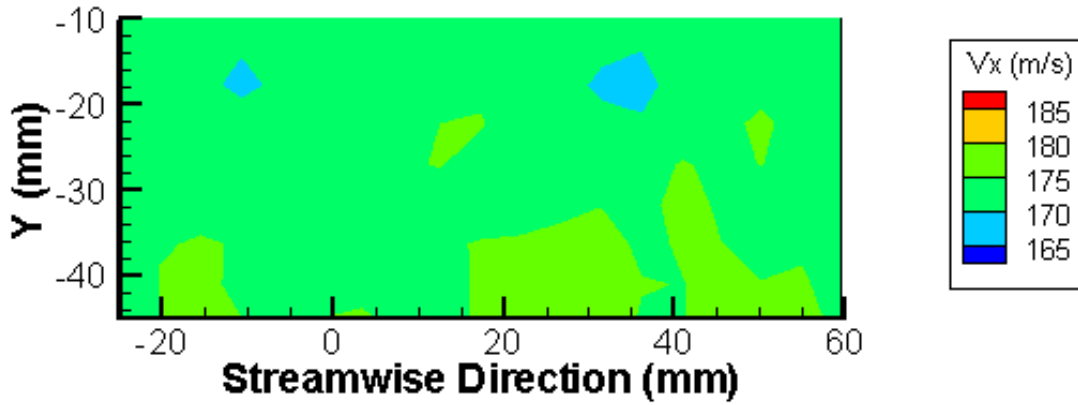


Figure 4.45: Streamwise velocity profile at $M = 0.5$, $P_0 = 1500$ psf, and $T_0 = 294$ K.

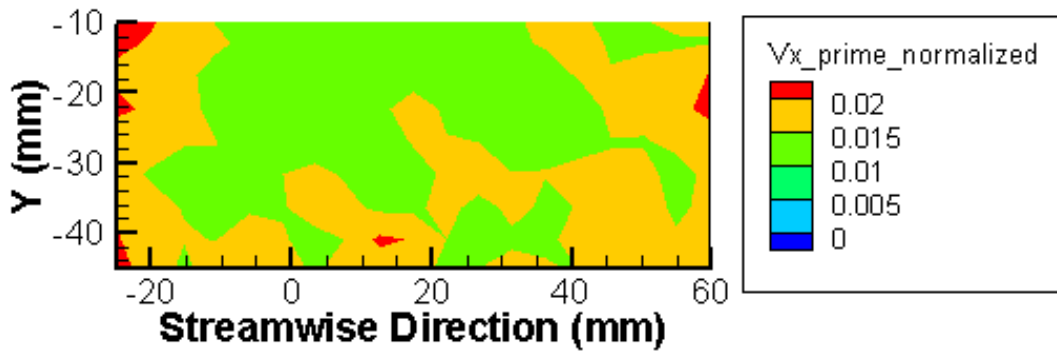


Figure 4.46: Streamwise turbulence profile at $M = 0.5$, $P_0 = 500$ psf, and $T_0 = 294$ K normalized by the calculated freestream velocity, 170 m/s.

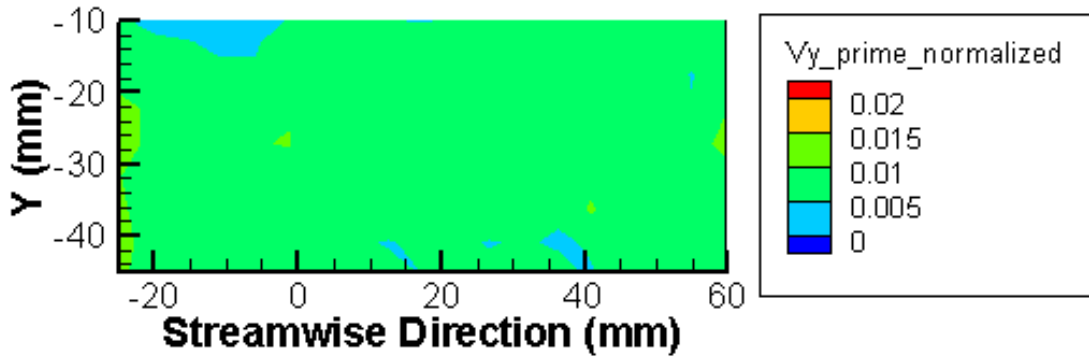


Figure 4.47: Vertical velocity turbulence profile at $M = 0.5$, $P_0 = 500$ psf, and $T_0 = 294$ K normalized by the calculated freestream velocity, 170 m/s.

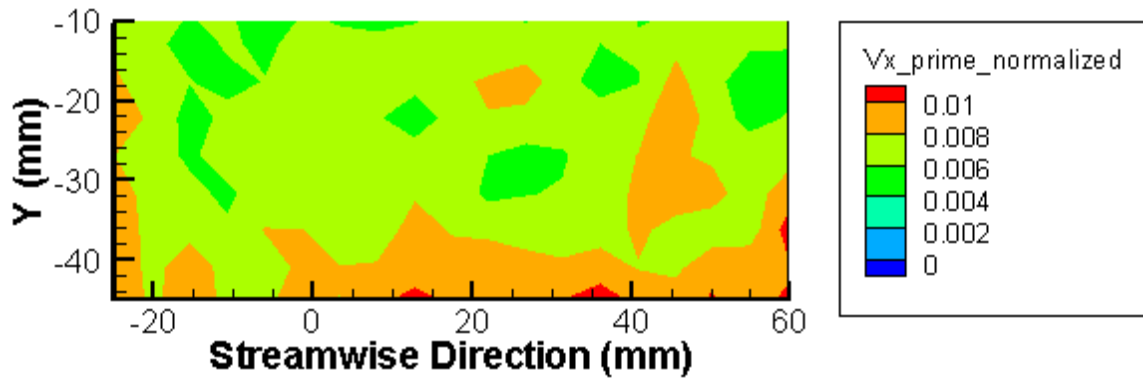


Figure 4.48: Streamwise turbulence profile at $M = 0.5$, $P_0 = 1000$ psf, and $T_0 = 294$ K normalized by the calculated freestream velocity, 170 m/s.

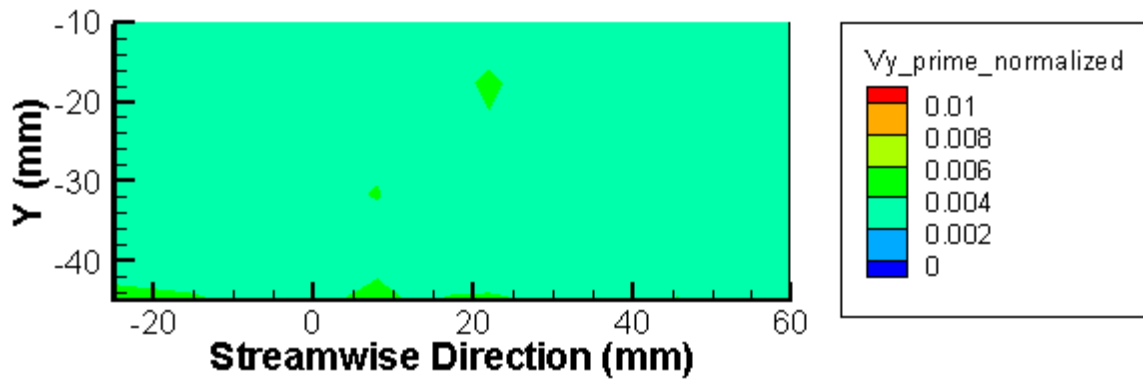


Figure 4.49: Vertical velocity turbulence profile at $M = 0.5$, $P_0 = 1000$ psf, and $T_0 = 294$ K normalized by the calculated freestream velocity, 170 m/s.

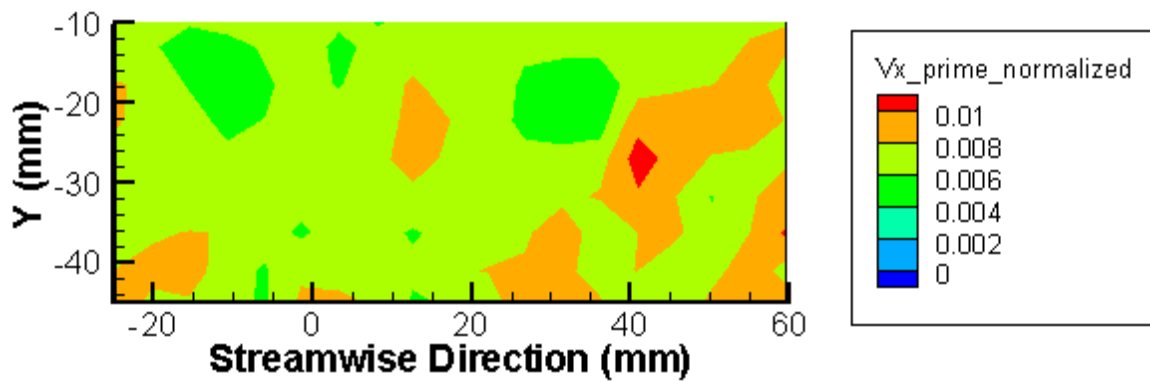


Figure 4.50: Streamwise turbulence profile at $M = 0.5$, $P_0 = 1500$ psf, and $T_0 = 294$ K normalized by the calculated freestream velocity, 170 m/s.

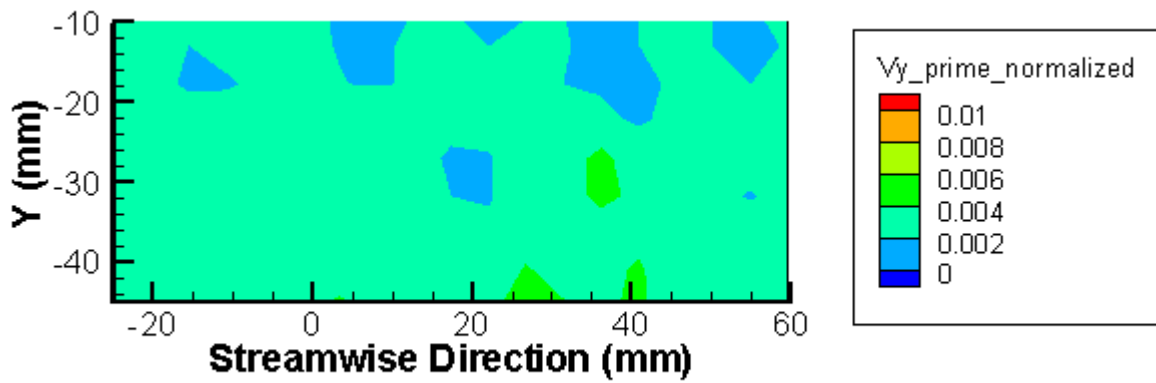


Figure 4.51: Vertical velocity turbulence profile at $M = 0.5$, $P_0 = 1500$ psf, and $T_0 = 294$ K normalized by the calculated freestream velocity, 170 m/s.

Figures 4.52, 4.53 and 4.54 are the streamwise velocity maps for a nominal Mach 0.30 velocity and pressures of 500, 1000 and 1500 psf. Based on tunnel instrumentation, the expected velocities for these three cases were approximately 100 m/s, 104 m/s and 104 m/s. The graphs are centered on these expected values and color contours are placed for the range ± 15 m/s. Following data collection at the 500 psf condition we found that at least one CO₂ injector had clogged, so the mass flow had been reduced, decreasing the number of particles and decreasing the smoothness of that data. The PIV data for the three conditions showed average streamwise velocities that closely matched expected velocities. Streamwise turbulence remained below 1.5% across much of the field whereas the vertical velocity component turbulence was less than 1% in the the two higher pressure cases. The low pressure case had pockets of turbulence near 2%, but again this is the test case that experienced a reduction of particles, so a decrease in the smoothness is expected. Turbulence profiles are given in Figures 4.55, 4.57, 4.59, 4.56, 4.58 and 4.60.

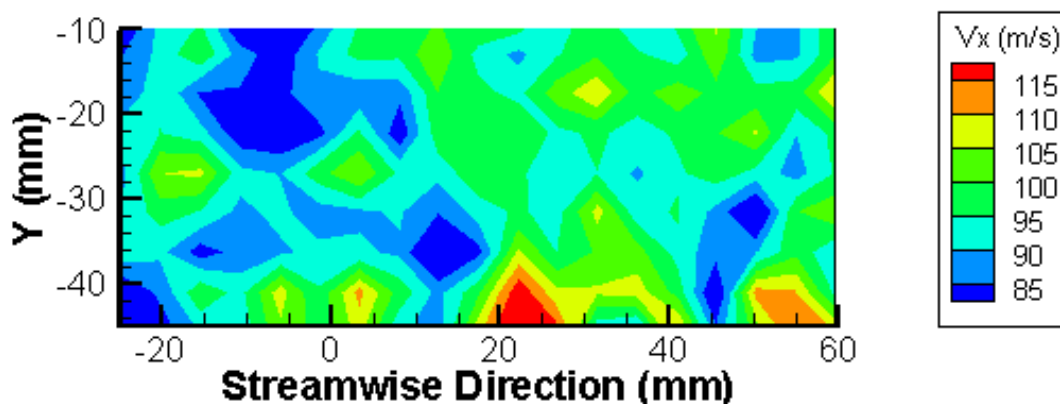


Figure 4.52: Streamwise velocity profile at $M = 0.30$, $P_0 = 517$ psf, and $T_0 = 298$ K.

4.3.3 Sources of Error in AFRL Wind Tunnel Testing. Two sources of error have been discussed above, causing less uniform results in the PIV data: first, the fluctuation in tunnel conditions during data collection, and second, the clogging of the CO₂ lines. In addition to these, large particles present in the flow and strong reflections both caused uncertainty in the data. The large particles caused pixel saturation with streak-

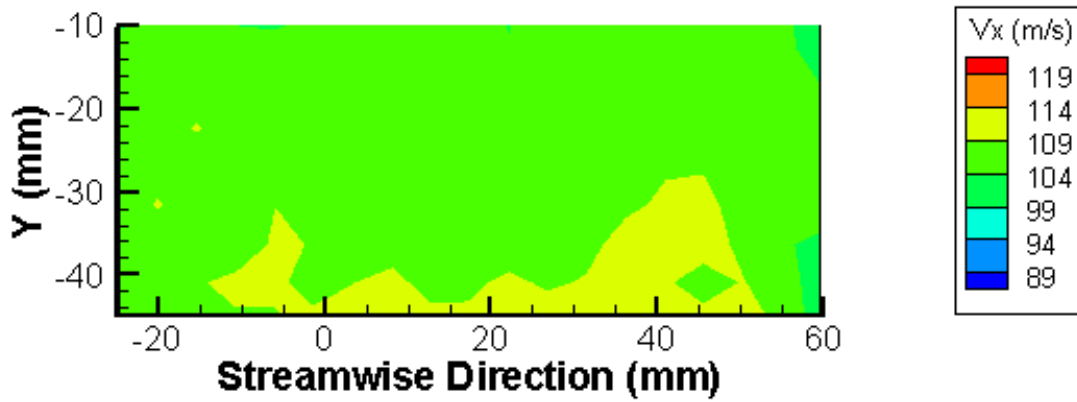


Figure 4.53: Streamwise velocity profile at $M = 0.30$, $P_0 = 1007$ psf, and $T_0 = 298$ K.

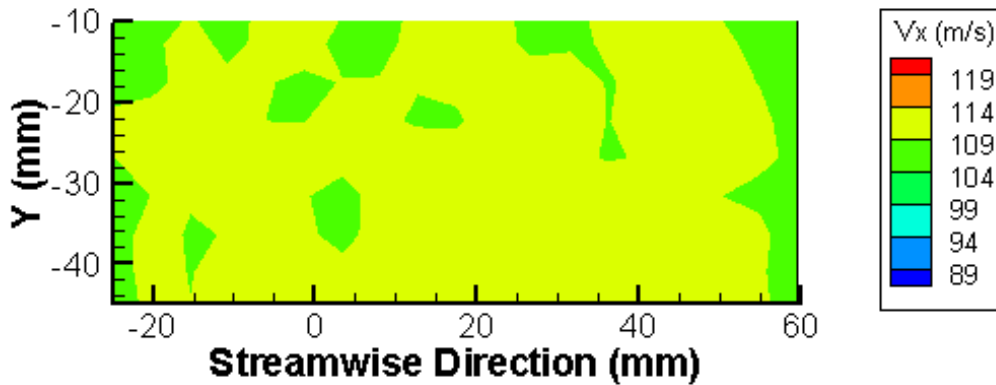


Figure 4.54: Streamwise velocity profile at $M = 0.30$, $P_0 = 1506$ psf, and $T_0 = 300$ K.

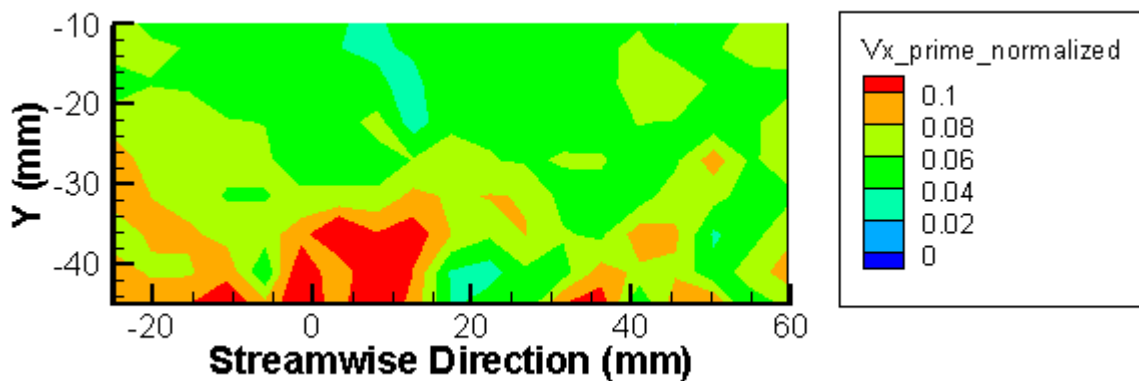


Figure 4.55: Streamwise turbulence profile at $M = 0.30$, $P_0 = 517$ psf, and $T_0 = 298$ K normalized by the calculated freestream velocity, 103 m/s.

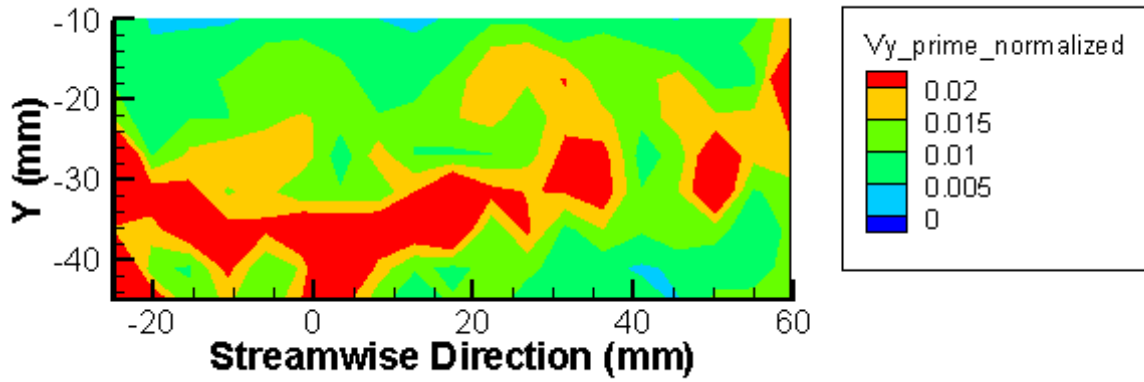


Figure 4.56: Vertical velocity turbulence profile at $M = 0.30$, $P_0 = 517$ psf, and $T_0 = 298$ K normalized by the calculated freestream velocity, 103 m/s.

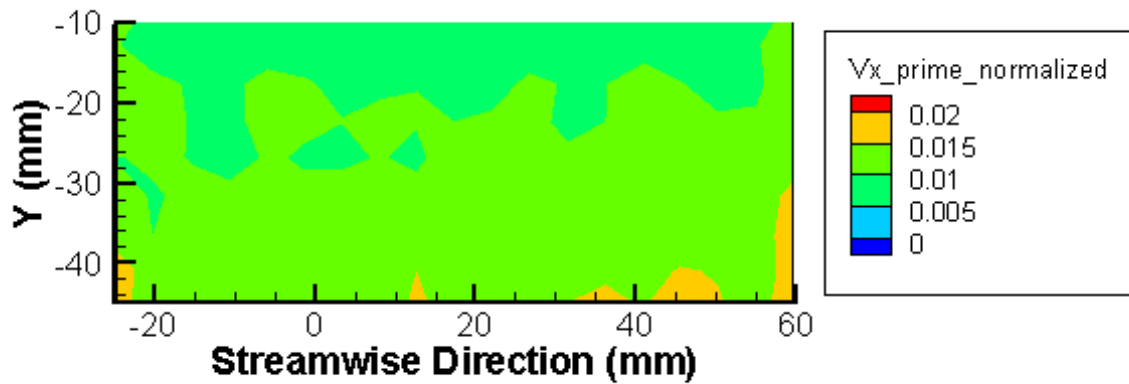


Figure 4.57: Streamwise turbulence profile at $M = 0.30$, $P_0 = 1007$ psf, and $T_0 = 298$ K normalized by the calculated freestream velocity, 104 m/s.

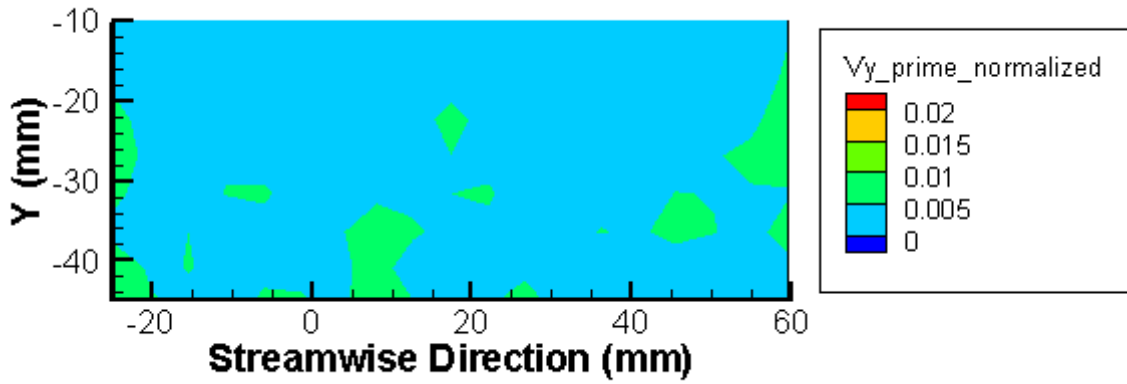


Figure 4.58: Vertical velocity turbulence profile at $M = 0.30$, $P_0 = 1007$ psf, and $T_0 = 298$ K normalized by the calculated freestream velocity, 104 m/s.

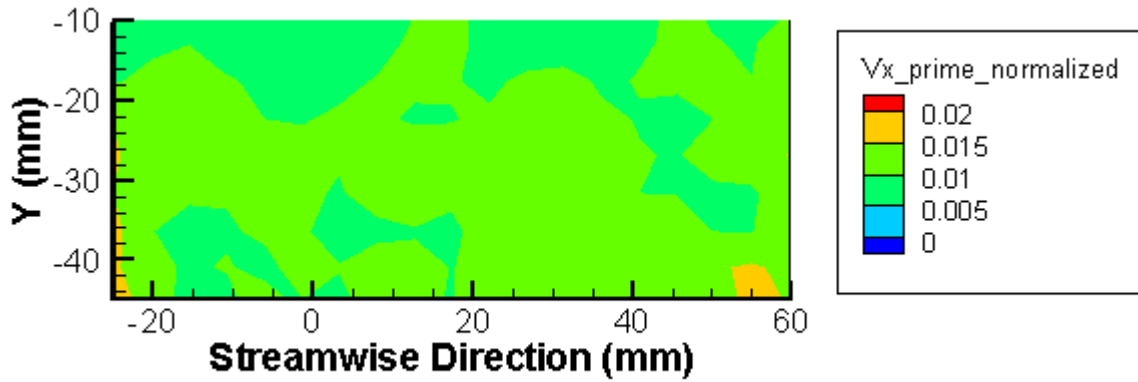


Figure 4.59: Streamwise turbulence profile at $M = 0.30$, $P_0 = 1506$ psf, and $T_0 = 300$ K normalized by the calculated freestream velocity, 104 m/s.

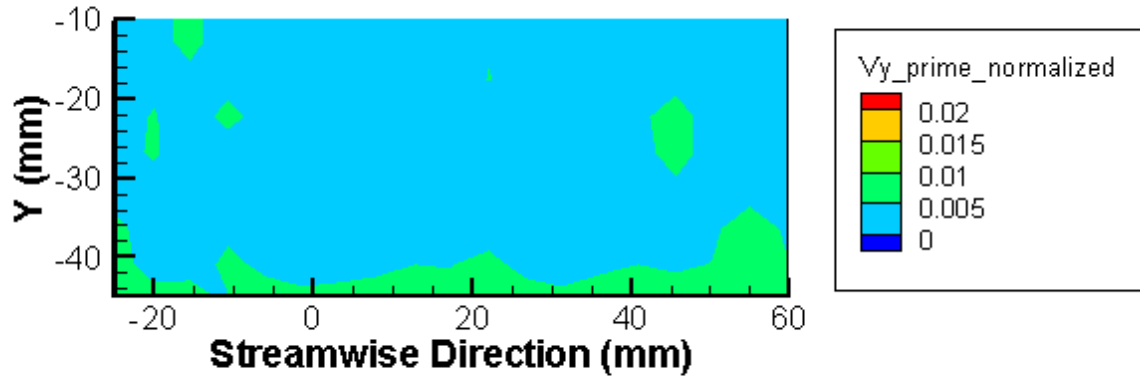


Figure 4.60: Vertical velocity turbulence profile at $M = 0.30$, $P_0 = 1506$ psf, and $T_0 = 300$ K normalized by the calculated freestream velocity, 104 m/s.

ing, decreasing the number of valid vectors available to render the figures above. Also, the reflections present in the image had the same effect, reducing the area used for PIV to about a third of the image field of view. Finally, as mentioned above, these results are based on a single set of 100 image pairs for each condition. Though particle coverage was sufficient to compute these results, typically only about 10-20 % of available vectors were used to determine the mean vector magnitudes presented in these results. Thus, more particles and more image pairs could improve the results.

V. Conclusions

5.1 Overview of Research Effort

PIV is a highly effective measurement technique, but its usefulness depends on careful selection of particles for flow seeding. Particle characteristics such as size and density are important in determining the response of the particle to the flow dynamics. Additionally, particle size affects the signal recorded by cameras used to collect PIV data. In many circumstances, particularly in closed-circuit tunnels, the particles can affect the safety and performance of the facility where they are to be used. Facilities such as the AFRL/RB TGF have difficulty using PIV because of the impact of the seed material on tunnel components. Seeding materials can accumulate within the tunnel, either attaching to wall surfaces or system components necessitating additional maintenance for tunnel operation. Thus, a method of cleanly seeding the tunnel for PIV measurements is sought.

To this end, research has been performed on the introduction of solid CO₂ particles for the application of PIV seeding. These dry ice particles are generated by allowing liquid CO₂ to expand through an orifice into a shroud tube which leads to solidified particles which are injected into the wind tunnel. The present study comprised determining the effects of changing the orifice tube and shroud tube size on particle size by using a Malvern Spraytec particle size analyzer to obtain mean particle sizes. In addition to the varying sizes of tubes, a different shroud tube using a Kenics[®] static mixer and heat exchanger tube was studied. Two combinations of injection methods were assessed in the AFIT 6 inch by 6.5 inch supersonic blowdown wind tunnel at Mach 1.92. A 10° ramp in the test section led to an oblique shock wave, and particle response was characterized. In this study three separate injection ports with identical orifice and shroud tube arrangements were used in this tunnel. This significantly increased particle population in the test section, which generally improves the spatial resolution and accuracy of the PIV data. Also three injection methods were qualitatively observed in the AFRL TGF at varying subsonic conditions to demonstrate the scaling effects and injection geometry of a larger tunnel (24 inch by 24 inch test section). Finally, PIV data was collected using the preferred injection method in the TGF at varying subsonic conditions, demonstrating

the applicability of the clean seeding method for PIV measurements at Mach numbers of 0.3, 0.5 and 0.8.

5.2 Conclusions

Particle size data collected using the Malvern Spraytec suggests that the static mixing shroud tube produced particles with a Sauter mean diameter, D_{32} , of approximately 3 times smaller than that for a simple straight shroud tube of nearly equal size. This tube was also more likely to clog, causing a reduction of particles. In separate experiments, the two different injector shroud types were then used in the AFIT 6 inch by 6.5 inch wind tunnel and particle response was assessed across an oblique shock wave. Three injectors of each type were employed, injecting into the stagnation chamber of the tunnel. The expectation was that smaller particles would be produced and they would respond to the oblique shock in a shorter distance than larger particles. The raw images suggested that smaller particles were being produced when the shroud with the mixer was used as it was necessary to increase the laser power and open the lens aperture to obtain images of similar quality to those captured using the simple shroud tube. This shroud tube increased the likelihood of clogging, however, causing a reduction in particles when clogging occurred.

The particles generated using the simple 0.33 inch shroud tube and 0.055 inch feed tube closely matched the freestream horizontal velocity expected from tunnel instrumentation within 3% using the larger, 64 x 64 interrogation region, which corresponded to 2.43 mm by 2.43 mm. The horizontal velocity far downstream of the shock was within approximately 3% of the calculated values as well. The vertical velocity component of the PIV results was 15 m/s upstream and 65 m/s downstream of the shock. The expected vertical velocity component upstream of the shock was assumed to be zero, and based on tunnel instrumentation and isentropic relations, the component downstream of the shock was calculate to be 77 m/s. The discrepancy in the vertical component suggests about 1° - 2° of flow angularity.

Using the static mixing shroud tubes and same feed tubes for similar test conditions, the differences between the computed and experimental velocities upstream and

downstream of the shock were also low. There was virtually no effect on the shroud tube on these mean velocity values. In both cases, using the smaller interrogation region (IR) caused a bias towards lower velocities which is in accord with the literature and the software manufacturer specifications. A reason for exploring a smaller IR was to determine whether the measured response of the particles to the shock could be improved in this experiment. There was no improvement when going to the smaller IR in either data set, suggesting that the IR size was not a factor in the response calculations.

Across the shock, the particles recovered to expected velocities based on tunnel instrumentation within approximately 15 mm normal to the shock. This would suggest particle sizes of approximately $2\ \mu\text{m}$ for both data sets, following the methodology laid out by Melling [13]. Schlieren images showed a strong interaction between the oblique shock and the tunnel floor boundary layer effects; shock motion of approximately 4 mm was observed in the freestream. Particle response was calculated based on the PIV data which is an array of mean velocity data. Therefore transient shock conditions would be averaged during the data processing, causing a smeared shock region in the velocity data results. Thus, the assumption that the shock acted as a step function is not necessarily valid for this setup. This shock motion suggests the response comparison to a theoretical $2\ \mu\text{m}$ particle is likely conservative and actual particle response could more closely match that of smaller particles using Melling's method.

For the first time, the CO_2 seeding method was scaled up and applied to the TGF successfully. By positioning the laser sheet perpendicular to the flow direction, observations could be made on whether particles injected into the stagnation region were persisting long enough to pass through the test section in this tunnel. The 0.068 inch ID feed tube and 0.40 inch ID curved shroud to direct particles downstream from the stagnation chamber produced the best particle coverage so this combination was replicated two times to provide three identical injectors at three points on either side of the stagnation chamber. A simple shroud tube injecting in the stagnation region normal to the streamwise direction was ineffective. The curved shroud tube was critical to the success because the particles were directed toward the test section, reducing the initial velocity difference between the particles and the freestream. After repositioning

the laser sheet and camera, PIV measurements were taken at three subsonic speeds at varying pressures. In all cases, the seeding was sufficient to provide mean velocities in the flow field which matched predicted values within a few percent. Freestream turbulence was typically between 1-2% except where problems with particle coverage due to clogging occurred and when tunnel settings drifted during data collection. The combination of injectors used in the TGF produced some large particles that saturated camera pixels introducing error into the IR correlations. Collecting and analyzing 100 image pairs using a range filter limited the impact of the large particles when computing mean velocities, though improved methods of dealing with the large particles are needed so that the method may be employed robustly. Importantly, no residue persisted in the tunnel following the data collection using the CO₂ to seed the flow.

5.3 Impact of Research

For the first time CO₂ was used to seed the TGF wind tunnel for PIV. Facilities such as the TGF can benefit from this method because of the low cost and availability of liquid CO₂, the ability to influence particle size by injector design, and because the seeding does not cause maintainability or safety problems. The characterization of the particle response may lead to improvements by providing a means of calculating the particle lag in the fluid. This is necessary to draw meaningful velocity data from PIV in dynamic fluid motion and to resolve small-scale motion in areas of interest where the relaxation distance of the particle is much closer in magnitude to the scale being resolved. Finally, the effect on particle size due to varying the injection method may be used to size the particles for the geometry of the tunnel it is used in. The distance between the injection point and the test section as well as the speed of the air flow of the tunnel are important for determining the residence time the particles must be able to achieve to be useful before sublimating completely.

5.4 Future Work

This and previous research have demonstrated the capabilities and limitations of various injection methods and injection locations, and have successfully scaled the in-

jection method for larger wind tunnel use. Future work may be devoted to acquiring particle response data for a stationary shock that is not influenced by boundary layer interaction. By designing a vertical wedge rather than a ramp, the shock-boundary layer interaction can be minimized and a shock attached to the wedge can be observed in the horizontal plane. Also, a method for limiting particle dispersion to enhance the concentration of particles in a desired area would enhance the accuracy of mean velocities and enable smaller interrogation regions, as well as make time-resolved PIV possible. In this and previous research, the particles have mainly been injected perpendicular to the flow direction within the stagnation region. This method has been suitable for observing an oblique shock wave as well as boundary layer flow in previous work because it provides an even distribution of particles across the entire test section cross-sectional area. However, in larger tunnels, an even distribution can be unnecessary. Given that PIV often focuses on a small subregion of a large tunnel, the ability to inject particles that cover just this region could enhance the ability to conduct PIV without having to utilize an excessive amount of CO₂ to seed the flow. In larger facilities such as the TGF, a structure could be installed completely within the stagnation region such that the injector tubes could be aligned with the flow direction as well as translated vertically and horizontally such that the particle concentration could be localized rather than dispersed. These areas of research may be unique to the tunnel using this technique, so future work could include the full scale introduction and use of dry ice seeding in a facility such as the TGF for a specific test.

Appendix A. Theoretical Response Curves Using Melling's Approach

The following spreadsheet is used to calculate the theoretical response of particles as proposed by Melling. The variables are calculated using the following expressions, given an upstream stagnation temperature, $T_{0,1}$, and Mach number, M_1 , as well as the shock angle, β . In all cases, the subscript, "1" refers to upstream of the shock, and "2" refers to downstream of the shock.

$$U_1 = M_1 \sqrt{\gamma R \left(\frac{T_{0,1}}{1 + \frac{\gamma-1}{\gamma} M_1^2} \right)}$$

Where $\gamma = 1.4$, and $R = 287 JKg^{-1}K^{-1}$.

To ensure the β used results with the correct ramp angle, θ , can be calculated:

$$\tan \theta = 2 \cot \beta \frac{M_1^2 \sin^2 \beta - 1}{M_1^2 (\gamma + \cos 2\beta) + 2}$$

The Mach number normal to the shock is:

$$M_{n,1} = M_1 \sin \beta$$

The normal velocity upstream of the shock is:

$$V_{n,1} = U_1 \sin \beta$$

The total temperature downstream of the shock is:

$$T_2 = T_1 \left[2 + (\gamma - 1) M_{n,1}^2 \right] \frac{2\gamma M_{n,1}^2 - (\gamma - 1)}{(\gamma + 1)^2 M_{n,1}^2}$$

The Mach number normal to and downstream of the shock is:

$$M_{n,2}^2 = \frac{1 + \left(\frac{\gamma-1}{2}\right) M_{n,1}^2}{\gamma M_{n,1}^2 - \frac{\gamma-1}{2}}$$

The velocity normal to and downstream of the shock is:

$$V_{n,2} = M_{n,2} \sqrt{\gamma RT_2}$$

The Mach number downstream of the shock is:

$$M_2 = \frac{M_{n,2}}{\sin(\beta - \theta)}$$

The velocity downstream of the shock is:

$$U_2 = M_2 \sqrt{\gamma RT} \cos \theta$$

Finally, Melling's relations can be applied to determine the theoretical particle response:

$$\frac{dv_p}{dt} = -C(v_p - U)$$

$$C = \frac{18\mu}{\rho_p d_p^2}$$

Calculations for Particle Response

$\rho = 1180 \text{ kg/m}^3$

T1 =	265
M1 =	1.92
U1 =	475.3289018
Beta =	41
Theta =	0.175890805
Mn1 =	1.259633336
Vn1 =	311.8438178
T2 =	308.8390331
Mn2 =	0.651711701
Vn2 =	229.5760486
M2 =	1.2682333
U2 =	439.8628391

deg
rad = 10.07780077 deg

d_p	C
0.0000002	2.82263E-07
0.0000004	1.12905E-06
0.0000006	2.54037E-06
0.0000008	4.51621E-06
0.000001	7.05657E-06
0.0000012	1.01615E-05
0.0000014	1.38309E-05
0.0000016	1.80648E-05
0.0000018	2.28633E-05
0.000002	2.82263E-05
0.0000022	3.41538E-05
0.0000024	4.06459E-05
0.0000026	4.77024E-05
0.0000028	5.53235E-05
0.000003	6.35091E-05

Theoretical Particle Responses Using AFIT Wind Tunnel Conditions

Time(s)	Vn 1.0um	Dist. Traveled (mm)	Vn 2.0um	Dist. Traveled	Vn 3.0um	Distance (mm)
	311.8438178	-0.602665882	311.8438178	-0.618010362	311.8438178	-0.621127227
	311.8438178	-0.30640885	311.8438178	-0.31041204	311.8438178	-0.311201206
	311.8438178	0	311.8438178	0	311.8438178	0
0	311.8438178	0.30640885	311.8438178	0.31041204	311.8438178	0.311201206
0.000001	300.9738832	0.602665882	308.9802625	0.618010362	310.558594	0.621127227
0.000002	291.540179	0.89011244	306.2163812	0.922892905	309.234485	0.929797985
0.000003	283.3529381	1.169912643	303.5487043	1.225154198	308.0480677	1.237233091
0.000004	276.2474668	1.443076792	300.9738832	1.524885483	306.8221428	1.543451847
0.000005	270.0808323	1.710481702	298.4886858	1.822174822	305.6153699	1.848473257
0.000006	264.7289873	1.972888333	296.0899925	2.117107214	304.4274497	2.152316025
0.000007	260.0842746	2.230957101	293.7747923	2.4097647	303.2580877	2.454998566
0.000008	256.0532619	2.485261163	291.540179	2.700226463	302.106994	2.756539005
0.000009	252.5548618	2.736297944	289.3833476	2.988568933	300.9738832	3.056955183
0.00001	249.5187007	2.984499146	287.3015906	3.274865875	299.8584743	3.356264666
0.000011	246.8837037	3.230239431	285.2922948	3.559188492	298.7604909	3.654484742
0.000012	244.5968655	3.473843956	283.3529381	3.841605504	297.6796607	3.95163243
0.000013	242.6121842	3.715594916	281.481086	4.122183241	296.6157157	4.247724484
0.000014	240.8897364	3.955737221	279.6743889	4.400985725	295.5683921	4.542777395
0.000015	239.3948733	4.19448342	277.9305788	4.678074748	294.5374302	4.836807397
0.000016	238.0975246	4.432017979	276.2474668	4.953509951	293.5225745	5.129830471
0.000017	236.971593	4.66850099	274.6229401	5.227348901	292.5235734	5.421862348
0.000018	235.9944292	4.904071393	273.0549596	5.499647159	291.540179	5.712918511
0.000019	235.1463768	5.13884977	271.5415569	5.770458354	290.5721477	6.003014204
0.00002	234.4103765	5.372940769	270.0808323	6.039834246	289.6192395	6.292164433
0.000021	233.771623	5.606435214	268.6709522	6.307824796	288.6812179	6.580383967
0.000022	233.2172671	5.839411927	267.3101469	6.574478223	287.7578506	6.867687347
0.000023	232.7361576	6.071939314	265.9967082	6.839841071	286.8489085	7.154088884
0.000024	232.3186164	6.304076744	264.7289873	7.103958261	285.9541663	7.439602669
0.000025	231.9562445	6.535875742	263.5053928	7.366873152	285.0734022	7.724242569
0.000026	231.6417522	6.767381025	262.324389	7.628627593	284.2063978	8.008022237
0.000027	231.3688135	6.998631401	261.1844932	7.889261977	283.3529381	8.290955111
0.000028	231.1319377	7.22966055	260.0842746	8.14881529	282.5128115	8.573054422
0.000029	230.9263601	7.460497702	259.0223522	8.407325163	281.6858098	8.854333191
0.00003	230.7479452	7.691168227	257.9973929	8.664827914	280.8717279	9.134804237
0.000031	230.593104	7.92169414	257.00811	8.9213586	280.0703639	9.414480178
0.000032	230.4587218	8.152094548	256.0532619	9.176951056	279.2815191	9.693373437
0.000033	230.3420953	8.382386035	255.1316499	9.43163794	278.5049981	9.97149624
0.000034	230.2408785	8.612582992	254.2421172	9.685450772	277.7406082	10.24886062
0.000035	230.1530354	8.842697909	253.383547	9.938419976	277.088816	10.52547844
0.000036	230.0767989	9.072741626	252.5548618	10.19057492	276.4474668	10.80136134
0.000037	230.0106354	9.302723551	251.7550212	10.44194394	275.8183451	11.07652082
0.000038	229.953214	9.532651848	250.9830212	10.6925544	275.200614	11.35096818
0.000039	229.9033796	9.762533603	250.2378928	10.94243269	274.6409957	11.62471453
0.00004	229.8601298	9.992374965	249.5187007	11.19160431	274.0940957	11.89777084
0.000041	229.8225945	10.22218127	248.824542	11.44009386	273.5986149	12.17014788
0.000042	229.7900187	10.45195715	248.154544	11.68792507	273.139992	12.44185626
0.000043	229.7617471	10.68170663	247.5078699	11.93512085	272.7000789	12.71290643
0.000044	229.737211	10.9114332	246.8837037	12.18170334	272.2766868	12.98330868
0.000045	229.7159168	11.14113987	246.2812633	12.42769386	271.86808323	13.25307312
0.000046	229.6974362	11.37082929	245.6997925	12.67311304	271.4700789	13.52220972
0.000047	229.6813974	11.60050373	245.1385614	12.91798075	271.0940957	13.79072829
0.000048	229.6674778	11.83016517	244.5968655	13.1623162	270.7236868	14.05863848
0.000049	229.6553974	12.05981532	244.0740248	13.4061379	270.36808323	14.32594979
0.00005	229.6449131	12.28945568	243.5693829	13.64946375	270.02808323	14.59267159
0.000051	229.6358141	12.51908755	243.0823066	13.89231099	269.69808323	14.85881308
5.2E-05	229.6279174	12.74871204	242.6121842	14.1346963	269.37808323	15.12438333
5.3E-05	229.621064	12.97833013	242.1584258	14.37663574	269.06808323	15.38939127
5.4E-05	229.6151162	13.20794267	241.7204617	14.61814484	268.76808323	15.65384567
5.5E-05	229.6099542	13.43755038	241.2977421	14.85923858	268.47808323	15.91775518
5.6E-05	229.6054743	13.66715391	240.8897364	15.09993142	268.19808323	16.18112832
5.7E-05	229.6015863	13.89675381	240.4959325	15.3402373	267.92808323	16.44397347
5.8E-05	229.5982121	14.12635056	240.115836	15.5801697	267.66808323	16.70629887
5.9E-05	229.5952836	14.35594457	239.7489698	15.81974163	267.41808323	16.96811265
6E-05	229.5927421	14.58553621	239.3948733	16.05896561	267.17808323	17.2294228
6.1E-05	229.5905364	14.81512579	239.0531022	16.29785378	266.94808323	17.49023718
6.2E-05	229.5886222	15.04471358	238.7232274	16.53641781	266.72808323	17.75056355
6.3E-05	229.5869608	15.27429982	238.4048348	16.77466899	266.51808323	18.01040951
6.4E-05	229.585519	15.50388471	238.0975246	17.01261821	266.31808323	18.26978259
6.5E-05	229.5842677	15.73346844	237.8009113	17.25027597	266.12808323	18.52869017
6.6E-05	229.5831817	15.96305115	237.5146224	17.48765243	265.94808323	18.78713951
6.7E-05	229.5822392	16.19263298	237.2382986	17.72475738	265.77808323	19.04513779
6.8E-05	229.5814212	8.386864657	236.971593	9.66772322	257.7745135	10.28080433

Bibliography

1. Linscott, R. N. and Da Vinci, L., *The Notebooks of Leonardo Da Vinci*, Random House, New York, NY, 1957.
2. Anderson, J. D., *Fundamentals of Aerodynamics*, McGraw-Hill, New York, NY, 4th ed., 2007.
3. Raffel, M., Willert, C., Wereley, S., and Kompenhans, J., *Particle Image Velocimetry, A Practical Guide*, Springer, New York, NY, 2nd ed., 2007.
4. “Knot,” Merriam-Webster Online Dictionary, 23 February 2010, <http://www.merriam-webster.com/dictionary/knot>.
5. Gongora-Orozco, N., Zare-Behtash, H., and Kontis, K., “Particle image velocimetry studies on shock wave diffraction with freestream flow,” 48th AIAA Aerospace Sciences Meeting, Orlando, FL, 4-7 January 2010.
6. Wehrmeyer, J., Menako, C., Sirbaugh, J., and Sinclair, D., “Planar Doppler velocimetry applied in the AEDC 16T large-scale transonic wind tunnel,” 48th AIAA Aerospace Sciences Meeting, Orlando, FL, 4-7 January 2010.
7. DeLapp, C. J., Reeder, M. F., Crafton, J., and Goss, L. P., “Clean Seeding Material for Particle Image Velocimetry Measurements,” 25th AIAA Aerodynamic Measurement Technology and Ground Testing Conference, San Francisco, CA, 5-8 June 2006.
8. McNeil, C. M., Peltier, D. W., Reeder, M. F., and Crafton, J., “Clean Seeding for Particle Image Velocimetry,” 22nd International Congress on Instrumentation in Aerospace Simulation Facilities, Pacific Grove, CA, 10-14 June 2007.
9. Greene, B. G., Reeder, M. F., and Crafton, J., “Characterizing dry ice particle response for clean seeding PIV applications,” 26th AIAA Aerodynamic Measurement Technology and Ground Testing Conference, Seattle, WA, 23-26 June 2008.
10. Greene, B. G., *Characterization and Control of Carbon Dioxide Seed Particles in Particle Image Velocimetry*, Master’s thesis, Air Force Institute of Technology, 2008.

11. Freeborn, A. B., King, P. I., and Gruber, M. R., "Swept-Leading-Edge Pylon Effects on a Scramjet Pylon-Cavity Flameholder Flowfield," *Journal of Propulsion and Power*, Vol. 25, No. 3, 2009, pp. 571–582.
12. Andrews, L. C., *Field Guide to Atmospheric Optics*, SPIE Press, 2004.
13. Melling, A., "Tracer particles and seeding for particle image velocimetry," *Measurements Science and Technology*, Vol. 8, No. 12, 1997, pp. 1406–1416.
14. Dantec Dynamics, Skovlunde, Denmark, *FlowManager software and introduction to PIV instrumentation*, 5th ed., 2000.
15. Whitlock, W., Weltmer, W., and Clark, J., "Apparatus and method for removing minute particles from a substrate," *US Patent 4,806,171*, 21 February 1989.
16. Masutti, D., Bernhardt, S., Asma, C. O., and Vetrano, M. R., "Experimental Characterization of Liquid Jet Atomization in Mach 6 Crossflow," 39th AIAA Fluid Dynamics Conference, San Antonio, TX, 22-25 June 2009.
17. Ibrahim, E. A., "Comment on 'Atomization Characteristics of Impinging Liquid Jets'," *Journal of Propulsion and Power*, Vol. 25, No. 6, 2009, pp. 1361–1362.
18. Settles, G. S., *Schlieren and Shadowgraph Techniques*, Springer, New York, NY, 2001.
19. Chemineer, Inc., Dayton, OH, *Kenics Static Mixing Technology Bulletin 800*, 2008.
20. Air Force Research Laboratory, *TGF User Manual*.
21. Stanley, D., Doty, J. H., and Altman, A., "Optimization of a PIV based study using maximum work potential and design of experiments techniques," 48th AIAA Aerospace Sciences Meeting, Orlando, FL, 4-7 January 2010.
22. Beresh, S. J., Clemens, N. T., and Dolling, D. S., "Relationship Between upstream turbulent boundary-layer velocity fluctuations and separation shock unsteadiness," *AIAA Journal*, Vol. 40, No. 12, 2002, pp. 2412–2422.
23. Papamoschou, D., Zill, A., and Johnson, A., "Supersonic Flow Separation in Planar Nozzles," *Journal of Shock Waves*, Vol. 19, No. 3, 2009, pp. 171–183.

REPORT DOCUMENTATION PAGE			<i>Form Approved</i> OMB No. 0704-0188		
The public reporting burden for this collection of information is estimated to average 1 hour per response, including the time for reviewing instructions, searching existing data sources, gathering and maintaining the data needed, and completing and reviewing the collection of information. Send comments regarding this burden estimate or any other aspect of this collection of information, including suggestions for reducing this burden to Department of Defense, Washington Headquarters Services, Directorate for Information Operations and Reports (0704-0188), 1215 Jefferson Davis Highway, Suite 1204, Arlington, VA 22202-4302. Respondents should be aware that notwithstanding any other provision of law, no person shall be subject to any penalty for failing to comply with a collection of information if it does not display a currently valid OMB control number. PLEASE DO NOT RETURN YOUR FORM TO THE ABOVE ADDRESS.					
1. REPORT DATE (DD-MM-YYYY) 25-03-2010		2. REPORT TYPE Master's Thesis		3. DATES COVERED (From — To) August 2008 – March 2010	
4. TITLE AND SUBTITLE Particle Size Control for PIV Seeding Using Dry Ice			5a. CONTRACT NUMBER		
			5b. GRANT NUMBER		
			5c. PROGRAM ELEMENT NUMBER		
6. AUTHOR(S) Brian T. Love, Capt, USAF			5d. PROJECT NUMBER		
			5e. TASK NUMBER		
			5f. WORK UNIT NUMBER		
7. PERFORMING ORGANIZATION NAME(S) AND ADDRESS(ES) Air Force Institute of Technology Graduate School of Engineering and Management (AFIT/ENY) 2950 Hobson Way WPAFB OH 45433-7765			8. PERFORMING ORGANIZATION REPORT NUMBER AFIT GAE ENY10-M15		
9. SPONSORING / MONITORING AGENCY NAME(S) AND ADDRESS(ES) Mr. Tom Presdorf Air Force Research Laboratory, Air Vehicles Directorate Bldg 45 2130 Eighth Street WPAFB, OH 45433-7542 937-255-6317			10. SPONSOR/MONITOR'S ACRONYM(S) AFRL/RBAI		
			11. SPONSOR/MONITOR'S REPORT NUMBER(S)		
12. DISTRIBUTION / AVAILABILITY STATEMENT APPROVED FOR PUBLIC RELEASE; DISTRIBUTION UNLIMITED					
13. SUPPLEMENTARY NOTES					
14. ABSTRACT Particle image velocimetry (PIV) has been carried out using solid carbon dioxide (CO ₂) particles as the seed material to continue the development of clean seeding for use in large-scale, closed-circuit tunnels. Testing occurred in two wind tunnels at subsonic and supersonic speeds using dry ice particles generated by allowing liquified CO ₂ to expand from a small diameter injector tube through a larger diameter shroud tube. The particles were injected into the plenum and discrete solid particles, suitable for PIV measurements, were present in the test section. Data on particle size were first collected using a Malvern particle size analyzer for three sizes of injector tubes, two sizes of shroud tubes, and two different types of shroud tubes: a simple tube and a static mixing tube. The injectors using the static mixing shroud tube and the simple shroud tube were each used in the adjustable throat supersonic blowdown wind tunnel at the Air Force Institute of Technology with a 6 inch by 6.5 inch cross-section. Particle size results for these two configurations suggested that the static mixing shroud tube decreased the Sauter mean particle diameter by a factor of three. In the tunnel, Mach 1.92 flow over a 10 degree ramp was produced and PIV images captured particles above the ramp, both upstream and downstream of the oblique shock while schlieren imaging provided insight into the flow conditions. Both the velocities far upstream and far downstream of the shock closely matched expectations, based on the wind tunnel instrumentation. Particle lag for the flow across the shock was quantified for the two cases, and despite the substantial, quantified differences in particle size measured at the shroud tube exit, the results for both shroud tubes were generally consistent with a theoretical response of a 2 micron particle. Finally, for the first time particles were injected into the stilling chamber of the Air Force Research Laboratory's closed-circuit Trisonic Gas-dynamics Facility, which has a 24 inch by 24 inch cross-section, at three subsonic speeds and four stagnation pressures. PIV was successfully carried out in each case. Measured streamwise velocities matched expected velocities within a few percent based on tunnel instrumentation, and freestream turbulence was found to be less than 2% in most cases. These results suggest that PIV using CO ₂ particles may be robustly implemented in this closed-circuit wind tunnel without risk of contaminating the tunnel.					
15. SUBJECT TERMS PIV, dry ice, TGF, oblique shock wave, particle image velocimetry, carbon dioxide					
16. SECURITY CLASSIFICATION OF: UNCLASSIFIED		17. LIMITATION OF ABSTRACT UU	18. NUMBER OF PAGES 103	19a. NAME OF RESPONSIBLE PERSON Dr. Mark Reeder	
a. REPORT U	b. ABSTRACT U			c. THIS PAGE U	19b. TELEPHONE NUMBER (Include Area Code) (937)255-3636, ext 4530